Effectively Identifying and Segmenting Individual Vortices in 3D Turbulent Flow

A DISSERTATION
SUBMITTED TO THE FACULTY OF THE GRADUATE SCHOOL
OF THE UNIVERSITY OF MINNESOTA
BY

Sheng-Wen Wang

IN PARTIAL FULFILLMENT OF THE REQUIREMENTS
FOR THE DEGREE OF
DOCTOR OF PHILOSOPHY

Victoria Interrante, Adviser

May 2011

Acknowledgements

During my Ph.D. studies at the University of Minnesota, I have received outstanding support and advice from a number of people that I would like to acknowledge at this time. First, I would express my sincere appreciation to Dr. Victoria Interrante, my advisor, for her expert guidance throughout this process. A special thank-you goes to Dr. Ellen Longmire for her exceptional advice and assistance on my research studies. In addition, I would like to acknowledge the work done by Dr. Jack Goldfeather, who led the research described in chapter 4. Dr. Longmire's previous students, Dr. Neelakantan Saikrishnan and Dr. Daniel Troolin provided timely assistance during this research. The experimental data created by Dr. Longmire and Dr. Troolin was significant in leading to our contributions described in chapter 6. My committee members, Dr. Gary Meyer and Dr. Dan Keefe, provided excellent comments and advice on my research. Finally, the support received from the faculty and staff in the Department of Computer Science and Engineering was invaluable.

A special thank you also goes out to my parents for their support and encouragement throughout my Ph.D. journey and to my friends in Minnesota who encouraged me in so many ways during this educational quest.

All the support described above has been vitally important in helping me toward the completion of my Ph.D. degree. The memories of my time in Minnesota will be treasured for the rest of my life.

Abstract

Three-dimensional, time-varying flow has been a significant research subject for decades. A long-term goal of the ongoing research in the turbulence community has been to develop an improved understanding of the dynamically-evolving vortex structure and organization in turbulent boundary layers. Such improved understanding requires the development and validation of accurate and robust numerical models of flow under complex conditions, and has the potential to enable the development of effective strategies to predict and control vortex generation and organization, which has influential practical impact in many industries.

The focus of this work is on understanding and visualizing the dynamics of three-dimensional flows. The primary objective is to study the relationship of various attributes in the flows, to relate multiple variables to the structure of turbulence and to correlate the evolution of vortex structures among all vortices' lifecycles. While many methods have been proposed for defining and visualizing vortices in 3D flow data, little attention has been devoted to the problem of robustly ensuring that the identified regions accurately correspond to individual vortex structures, as opposed to containing entangled clusters of closely spaced and potentially intertwined vortices. The success of efforts to effectively analyze unsteady flows at the level of individual structures critically depends on this ability.

This dissertation presents innovative methods for achieving the primary research objective of overcoming the limitations of current methods for vortex definition and

feature extraction in 3D turbulent flows. Multi-variate visualization of 3D turbulent flow data provides efficient schemes for effectively conveying multiple scalar and vector quantities and their relationships within identified target regions. The LIC glyph approach allows the detailed characteristics of important scalar variables such as vorticity magnitude, swirl strength and velocity magnitude, as well as vector properties such as direction and orientation, to be understood both individually and in relationship to each other throughout a complex flow. This contribution is critical in the feature identification process.

Two novel approaches are proposed for pursuing our efforts to achieve a robust segmentation of a 3D turbulent flow dataset into individual vortex regions. The first approach is based on the intuition that while any single scalar measure may not provide enough information, by itself, to robustly define an appropriate segmentation of a composite region into individual vortices, it is possible that better results can be achieved by considering multiple, non-redundant, local scalar and vector measures in combination. A careful mathematical analysis of the interrelationships between swirl and vorticity is derived to show how these measures can be used together to resolve ambiguities in structure identification that cannot be as successfully determined using either measure alone. In a second, different approach to the problem, we introduce a novel method for automatically detecting potential compound structures in an initial segmentation of a flow and coherently partitioning the constituent components. This method is based on the combined use of vortex core lines and hierarchical region

identification. The datasets used in this research were obtained from a direct numerical simulation of a turbulent channel flow by Zandonade and Moser [1].

Finally, we have applied our segmentation and tracking schemes to a time-varying experimentally acquired flow dataset to effectively visualize the dynamic and irregular evolution of a three-dimensional vortex ring. The vortex structures in this data consist of a tilted primary vortex ring and two opposite vertical streams, which branch irregularly with the perturbed fluids. A full analysis and visualization approach successfully identifies each individual vortex and consistently highlights significant structures, corresponding to well-correlated flow features, over time.

In summary, this dissertation introduces approaches to effectively depict the physical attributes, distribution, orientation and strength of vortex structures within both numerically simulated and experimentally acquired turbulent flow data. Investigations of the relationships between multiple variables in the data have assisted the development of two novel algorithms for the identification and segmentation of individual vortices within compound regions. Finally, through the application of our feature tracking methods to time-varying vortex rings, we have successfully demonstrated the ability of our methods to achieve reasonable segmentation results across a wide range of input data types, and to enable tracking coherent structures over time.

Contents

Acknowledgements ..... **i**

Abstract ..... **ii**

Contents ..... **v**

List of Tables ..... **viii**

List of Figures ..... **ix**

Chapter 1 Introduction **1**

1.1 Motivation **2**

1.2 Objectives **3**

1.3 Overview **4**

1.4 Contributions **6**

Chapter 2 Background **8**

2.1 Flow Visualization **10**

2.1.1 Vector Field Definition 11

2.1.2 2D Flow Visualization 13

2.1.3 3D Flow Visualization 20

2.2 Fluid Dynamics **26**

2.2.1 Turbulent Flow 26

2.2.2 Particle Image Velocimetry 30

2.2.3 Direct Numerical Simulation 31

2.3 Vortex Organization and Extraction **31**

2.3.1 Vortex Organization in Turbulent Boundary Layers 32

2.3.2 Feature Extraction Methods 35

Chapter 3 Visualization Methods 40

3.1 Direct Numerical Simulation Dataset 41

3.2 Time-Evolving Vortex Ring Dataset 42

3.3 Vortex Identification 43

3.3.1 Vortex Region Identification 43

3.3.2 Individual Vortex Identification 45

3.4 Vortex Feature Visualization 47

3.4.1 Direct Flow Visualization 47

3.4.2 LIC Glyph Method 50

3.5 Discussion 75

Chapter 4 Segmentation Using Multiple Scalar and Vector Quantities 77

4.1 Approach Ideas 78

4.2 Quantities of Vorticity and Swirl 80

4.3 The Relationships between Vorticity and Swirl 82

4.4 Segmenting Compound Structures Using Vorticity and Swirl 84

4.5 Experimental Results 88

4.6 Discussion 93

Chapter 5 Segmentation Using Vortex Cores 94

5.1 Vortex Region with Multiple Joint Vortices 95

5.2 Vortex Core Line Detection Method 97

5.2.1 Predictor-Corrector Method 98

5.2.2 Variation of Predictor-Corrector Method 101

5.3 Segmentation of Individual Vortices 103

5.4 Experimental Results 111

5.5 Sensitivity Analysis 117

5.6 Statistics Analysis 122

5.7 Discussion 125

Chapter 6 Segmenting and Tracking Time-Varying Vortex Ring Data 127

6.1 Vortex Identification and Tracking 128

6.1.1 Vortex Ring Identification 128

6.1.2 Noise Fading 129

6.1.3 Region Correspondence 129

6.1.4 Attribute Correspondence 130

6.1.5 Global Correspondence 131

6.2 Algorithm 132

6.2.1 Segment Tracking and Determination 132

6.2.2 Application to Time-Evolving Vortex Ring Data 137

6.3 Experimental Results 144

6.4 Discussion 147

Chapter 7 Conclusion and Future Work 149

Bibliography 152

Appendix 159

List of Tables

Table 5.1: This table shows, for each connected region in our dataset, the number of constituent vortices detected using one pass of our segmentation algorithm. 123

List of Figures

Figure 3.1: The entire turbulent channel flow in a plane. The rectangle in the upper left side shows a sub-volume of our dataset. Red and blue colors represent higher and lower speed areas respectively. 42

Figure 3.2: An entire view of vortices in a turbulent channel flow identified by iso-surface extraction on swirl strength.....44

Figure 3.3: A close-up view of vortices in a turbulent channel flow identified by iso-surface extraction on swirl strength.....45

Figure 3.4: The upper left image shows a vortex with simple structure. The upper right image shows a connected region form by two individual vortices touching each other. The lower left image shows a region with several complicated elongated structures. The lower right image shows a complicated clump containing multiple interacting structures.....46

Figure 3.5: Left figure shows two categories of arrows, indicated by distinct red and blue colors. The red arrows show the vorticity direction and the blue arrows show the normals to the rotation plane defined by the swirl. Right figure provides a close-up view of a central portion of the image on the left. 49

Figure 3.6: In these images, the colors of the arrow heads are defined using a weighted common mixing color (between red and blue) according to magnitude of the angle between the paired vector values. Vectors that are more aligned have more

similarly colored tips. The shafts of the arrows remain rendered in the original colors (red and blue). 49

Figure 3.7: Here the colors of the arrow heads are defined using a weighted common mixing color (between red and blue) according to magnitude of the angle between the paired vector values, with the interpolation occurring between boundary values that are twice the standard deviation away from the mean angle size. 50

Figure 3.8: This diagram shows the implementation details of the LIC glyph method, which portrays detailed information in the regions of interest in the flow using glyphs and other meaningful visual primitives. 58

Figure 3.9: The upper left image and lower left image show the rainbow colormap and color saturation respectively. The upper right image and lower right image show color wheels of the RGB color model and HSV color model respectively. 58

Figure 3.10: Using the LIC glyph method to indicate vorticity direction within a vortex region. Glyphs with color transitions encompassed by thin gray outlines convey vorticity direction effectively. 60

Figure 3.11: Using the LIC glyph method to visualize vorticity directions withing a vortex ring. This figure shows regular LIC glyphs representing vorticity direction using the rainbow color model. 61

Figure 3.12: Using the LIC glyph method to show the orientation of the vorticity vectors within a complex. Different vorticity orientations are represented using different colors. 63

Figure 3.13: Using the LIC glyph method to convey information about the orientation of the vorticity vectors within a vortex ring using our regular color model (left) and HSV color model (right). 63

Figure 3.14: A combination of two different color coding methods for visualizing vorticity direction and orientation within a target region in a 3D turbulent flow. ..65

Figure 3.15: A combination of two different color coding methods for visualizing vorticity direction and orientation for a time-evolving vortex ring dataset. In the left image, regular LIC glyphs are used to portray vorticity direction and orientation using our regular color model. The image on the right shows the same information using the HSV color model. 65

Figure 3.16: Using LIC glyph method to portray vorticity magnitude. Left: Vorticity magnitude within a target region in a 3D turbulent flow is depicted by the variation of color saturation. Right: Vorticity magnitude in the vortex ring data is depicted using transparency. 67

Figure 3.17: Using the LIC glyph method to show velocity information within an interesting target region. A simple color coding method is applied by varying the red color toward white to depict velocity direction, with velocity orientation still delivered by the shape of the glyphs. 68

Figure 3.18: Two groups of LIC glyphs convey information about vorticity and velocity simultaneously. The vorticity direction is encoded by color coding using the rainbow color scale, and the velocity direction is encoded by color coding using a single red color varying toward white in the leading part. 70

Figure 3.19: The left image shows that regular LIC glyphs are used to portray vorticity direction. The right image shows that regular LIC glyphs encode both vorticity direction and orientation. 71

Figure 3.20: LIC glyphs being used to encode a combination of vorticity and velocity information. The glyph direction is defined by the vorticity direction, and the glyph size is defined by the velocity magnitude. 72

Figure 3.21: Using LIC glyphs and arrows to visualize multiple vector fields. Here, the LIC glyphs are used to portray the vorticity direction while arrows show the swirl vectors.....73

Figure 4.1: Vortices defined by a threshold level of swirl strength. The region marked in red represents a compound structure defined by a connected set of neighboring voxels all with supra-threshold values.....79

Figure 4.2: Swirl rotation axes represented by the plane normal n and swirl vector r...82

Figure 4.3: Individual vortices segmented according to a threshold level of swirl strength (only), for two different thresholds. 86

Figure 4.4: Individual vortices defined by similar threshold levels of swirl strength, and by threshold differences between the swirl and vorticity directions at neighboring points.....87

Figure 4.5: Vortex segmentation using vorticity c (Top) and normal vector n (Bottom). 90

Figure 4.6: Vortex segmentation using swirl vector r (Top) and vorticity c (Bottom). .91

Figure 4.7: Vortex segmentation using vorticity c (Top) and both vorticity c and swirl vector r (Bottom). 92

Figure 5.1: Upper left, upper right, lower left, and lower right images show different regions by four different thresholds which increase in equal steps.....96

Figure 5.2: The left image shows a connected region with two roughly symmetrical elongated tubes that join each other near one end. The right image shows a region with three elongated tubes and one small blob that all join together. 97

Figure 5.3: The left image shows an extremely complex connected region, the red entity, that exists in the volume. The right image shows the same entity in isolation. 97

Figure 5.4: Upper left: vorticity ω_i is computed at a vortex core position v_i. Upper right: the next vortex core position v'_{i+1} is predicted from the last position v_i and the vorticity ω_i. Lower left: vorticity ω'_{i+1} is computed at the predicted vortex core position v'_{i+1}. Lower right: the predicted vortex core position v'_{i+1} is corrected to

v_{i+1} according to the local minimum of pressure on the plane perpendicular to the vorticity direction ω'_{i+1} at position v'_{i+1}.....100

Figure 5.5: These four images illustrate the basic concept of the segmentation algorithm presented in this chapter. Image A shows an interesting region of the flow, consisting of two elongated touching tubes. Image B shows some candidate sub-regions inside the interesting region. Image C shows that some of these sub-regions are joined by vortex core lines, and two groups of related sub-regions have been identified. Image D shows that the group information enables the segmentation of the compound region into two distinct vortices.....104

Figure 5.6: This flow chart describes the algorithm used for the segmentation of individual vortices. 110

Figure 5.7: The left image shows the intermediate result of the vortex segmentation algorithm. The right image shows the final result of the vortex segmentation algorithm. Two individual vortices are identified and distinguished by using red and blue colors. 112

Figure 5.8: A success case of our algorithm. The top and middle images show the different segments that are identified at each intermediate level, and the bottom image shows the successful segmentation after multiple iterations. 114

Figure 5.9: Another automatic segmentation produced by our algorithm. The top image shows one connected clump. The middle and bottom images show the

segmentation result with eight individual vortices from different viewing angles. 115

Figure 5.10: The top image shows a successful segmentation of a very complex and large vortex clump. The bottom image shows the individual vortices of this region in the context of the surrounding flow.....116

Figure 5.11: This image shows that the individual vortices can be identified from this very complex and large vortex clump. 117

Figure 5.12: An experimental investigation of the sensitivity of the segmentation to the number of threshold levels used, for two different compound regions. 119

Figure 5.13: The left image shows seven major individual vortices captured by iterations at eleven threshold levels for the complex region, Structure0110. The right image shows six major individual vortices captured by interations at thirteen threshold levels for the same complex region. 120

Figure 5.14: Eight major individual vortices are captured by iterations at fourteen and nineteen threshold levels for the complex region, Structure0110. 120

Figure 5.15: This image shows the reason leading to the decreasing number of segments found using certain numbers of threshold levels. 121

Figure 5.16: This image shows, for each connected region in our dataset, the number of constituent vortices detected using one pass of our segmentation algorithm. 123

Figure 5.17: The left image shows the volume distribution of all connected regions. The right image shows the volume distribution of 100 largest connected regions. 124

Figure 5.18: The left image shows the distrubiton of detected structures. Locations of the entities' centroids are represented by dots. The right image shows the same distribution on the Y-Z plane. 124

Figure 6.1: Feature A has spatial correspondence with feature B and feature C. Regarding attribute correspondence, the size of feature A is more similar to the size of feature B than to that of feature C. Therefore, the feature A in time step t1 evolves as feature B in time step t2. 130

Figure 6.2: The left image shows that the contiguous features A and B are detected in time step t1. They are considered to be the same feature since a split event has never occurred. The right image shows that the features A and B are contiguous in time step t1 and separate in time steps t2 and t3. They are considered to be distinct features. 132

Figure 6.3: This algorithm describes a series of stages for segment tracking between successive time steps. Tracking information is maintained by each segment's index. 133

Figure 6.4: This algorithm describes a series of stages for the segmentation of individual vortices in a time-varying vortex ring. 143

Figure 6.5: This figure shows a series of individual vortices identified inside the volume at the following time steps: 10 (Top left), 15 (Middle left), 20 (Bottom left), 29 (Top right), 34 (Middle right), and 42 (Bottom right) viewed from the front. 145

Figure 6.6: This figure shows a series of individual vortices identified inside the volume at the following time steps 10 (Top left), 15 (Middle left), 20 (Bottom left), 29 (Top right), 34 (Middle right), and 42 (Bottom right) viewed from the side. 146

Chapter 1

Introduction

Scientific visualization of 3D turbulent flow is an important topic, as understanding the physics of turbulence remains one of the great unsolved challenges of our time. Researchers have proposed a variety of different algorithms to identify and portray features in 3D turbulent flow data, in order to develop an improved understanding of dynamically-evolving behavior in fluid dynamics. However, current techniques remain insufficient to efficiently and effectively provide the insights desired. The visualization and analysis of turbulent flows is complicated by the fact that the essential basic feature of turbulence, a vortex, or local region of swirling flow, does not have an exact, calculable definition. Understanding the behaviors of vortices is critical in many practical applications such as aircraft and automobile design, as well as burning chambers. Unfortunately, the relationship between variables relating to vortices and other physical phenomena in fluid dynamics is complicated and unclear. Of particular interest is understanding how groups of vortices interact and how their common behavior relates to specific characteristics of turbulent flow [2, 3]. Specific to the work

in this dissertation, the visualization of 3D flow data on vortices can help researchers understand how to better use computed quantities such as vorticity, velocity and swirl strength to more effectively identify relationships and structures of interest in the flow, and the ability to robustly identify individual vortices within a complex 3D turbulent flow can assist researchers in tracking vortex evolution and studying vortex interaction.

1.1 Motivation

Turbulent flow visualization has been an active research topic for several decades. Numerous practical applications rely on this research, including aircraft and car design [4, 5], combustion simulation and modeling [6], and more. The improved understanding of vortex evolution and dynamics is essential to investigations of related properties in fluid dynamics such as Reynolds stress, turbulent motion, and drag. Among the many questions raised about vortices or eddies are: How often does the merging of vortices occur? How do vortices merge? How does a vortex split? Does one vortex absorb others or do multiple vortices evolve into a new vortex? How do vortices contribute to drag? [7] Understanding these questions creates possibilities to more effectively control vortex generation and evolution. However, these questions are unfortunately not easily answered. A variety of techniques have been proposed to depict flow fields, but more development is required in particular to enable the effective visualization and analysis of 3D turbulent flow fields due to perceptual issues and clumping problems. In addition, the discrete nature of the 3D datasets makes the

accurate computation and extraction of small flow features particularly challenging. Knowledge of the physics of turbulence is essential to the development of effective visualization and analysis tools. However, the lack of a precisely calculable definition of a vortex makes effective feature extraction and visualization more difficult.

1.2 Objectives

The goal of this work is to develop enhanced visualization techniques for 3D turbulent flow and improved methods for identifying individual vortices in highly cluttered flows, in order to aid the understanding of the physics of 3D turbulent flow. Besides, providing ways to effectively investigate regions of strongly swirling flow and to robustly identify individual swirling structures is also very useful to assist researchers in understanding intrinsic features of vortices. Automatic segmentation and feature tracking throughout an entire time-evolving flow can facilitate the investigation of massive 3D flow data, and enable researchers to focus more effectively on the important information in the flow. We hope that our efforts to facilitate the understanding of 3D turbulent flow could eventually help reveal unknown phenomena in fluid dynamics and have a positive impact on real world applications. In automobile design, vortices are present in the chaotic air currents and should be reduced to prevent unnecessary resistance. In aircraft design, vortices influence not only resistance but also lift. Understanding the characteristics of drag with respect to vortices could inform the development of methods to reduce turbulent friction over aircraft, which could lead to

decreased fuel usage and cost, increased cruise range, and reduced pollutants and greenhouse gas emissions as well. In burning chambers, controlling vortices in the flow helps enhance the burning efficiency, because the existence of vortices can boost the mixing of oxygen and fuel.

1.3 Overview

This dissertation presents a series of novel methods to visualize, identify, segment, and track individual vortices in 3D turbulent flows.

Chapter 2 reviews previous work in three different areas: flow visualization (section 2.1), fluid dynamics (section 2.2), and vortex organization as well as extraction (section 2.3). This chapter is important because it provides the background knowledge and work that could be developed to form the dissertation. The visualization section introduces the general definition and knowledge of flow fields and reviews important visualization techniques for 2D and 3D flow fields. The fluid dynamics section reviews the relevant knowledge and research in fluid dynamics. The vortex organization and extraction section focuses on vortex organization in turbulent boundary layers and the most important schemes for the extraction of vortices.

Chapter 3 introduces techniques to identify vortices in 3D turbulent flow fields. A series of multi-variate visualization techniques are developed to portray the inner volume of the identified region. Different color coding methods are applied to different

flow properties in order to illustrate the characteristics of the vortices in 3D turbulent flow.

Chapter 4 presents a new method for differentiating individual vortex structures in a connected region. Detailed relationships between vorticity and swirl vectors are carefully derived. We notice that the behaviors of three kinds of characteristic vectors are quite distinct in some areas but align in some other areas within areas of high swirl strength. A vortex identification method is proposed to segment these clumps into individual vortices by using a region-growing algorithm.

Chapter 5 demonstrates a novel technique to segment individual vortices. This technique combines the methods of region-based vortex identification and line-based vortex extraction to distinguish different individual vortices within a complex region. Different threshold levels of swirl strength are to identify a target region and candidate sub-regions. The adaptation of a predictor-corrector method is used to determine the correlation of each candidate sub-region so as to provide the information for segmenting the vortex. In addition, the technique of hierarchical vortex identification significantly enhances the capability of vortitcal structure extraction on the complex clump.

Chapter 6 provides a tracking algorithm for automatically segmenting all vortices in the flow from all series of time-steps and examining and tracking the individual vortices in the entire time-evolving data of the flow to determine the final segments. This scheme segments each connected region into individual vortices at each time-step, correlates correspondence between successive time-steps, and further analyzes their global correspondence to determine the final segments corresponding to the important vortices

throughout all time steps. By enabling the effective identification and tracking of individual vortices, our methods have the potential to enable researchers to gain deeper insight into the evolving processes in turbulent flows, without being distracted by extraneous noise in the data.

Chapter 7 presents the conclusions and future work.

1.4 Contributions

The main contributions in this dissertation are as follows:

- Visual descriptions of different features with various color coding strategies. Multiple vector and scalar quantities in the 3D flow data are represented with different color coding schemes to provide insights into promising ways of differentiating individual vortices within a connected region.

- Vortex segmentation by combination of different quantities. This scheme is conducted by using the combination of multiple quantities such as vorticity and swirl vectors to separate vortices.

- Vortex segmentation by vortex core lines and hierarchical vortex region identification. This algorithm relies upon the two types of techniques, vortex region-based and core-based schemes, with the development of revolutionary

hierarchical vortex region identification for achieving the effective segmentation of extremely complex constituent vortex clumps.

- Automatically segmenting and tracking individual vortices within an entire volume of experimental flow data. Our schemes examine and segment the entire volume of the time-evolving vortex ring dataset automatically, providing clearer information of vortical structure and vortex evolution.

Chapter 2

Background

The content in this chapter includes the review of the background research and knowledge regarding the remainder of this dissertation. The main goal of our research is to investigate the physical properties relating to the vortices so as to understand, identify, segment, and track these vortices.

The techniques developed in this dissertation have been applied to the numerical simulation data set of the turbulent channel flow and experimental ring data in order to assist researchers in Department of Aerospace Engineering and Mechanics in the University of Minnesota to resolve their problems. The research that many interdisciplinary researchers work on together has been becoming important because a complicate problem sometimes does not involve only one specific field. Therefore, a project which involves many researchers in different fields provides a best opportunity to solve the problem which could be interesting in different fields. The persistent interaction among researchers coming from different departments is required in order to advance the achievements of the work continuously. The collaboration between

application scientists and visualization scientists has been proceeding for a period of time. The application scientists propose the interesting unsolved problems in their field and the basic knowledge in the specific area are introduced. They cooperate with other scientists such as visualization scientists to investigate these problems and develop the solutions. The visualization scientists, then, realize algorithms used to solve the problems and visualize them. The visualization results are sent back to application scientists for an objective assessment of the success in terms of the goal of solving the proposed problems.

The common challenging part of this research is the lack of the thorough understanding of the characteristics in fluid dynamics so the existing algorithms may be restricted. Moreover, the objective assessment of the results is also challenging since the success of the algorithm may not be deterministic in some cases.

In this chapter, we also review the basic visualization methods in 2D and 3D turbulent flow fields with their advantages and disadvantages. We also introduce the fundamental knowledge of the fluid dynamics, and characteristics, multiple quantities, as well as vectors in physics are investigated to be utilized in the rest of the chapters. Finally, we focus on the discussion about the vortex feature extraction methods.

Section 2.1 briefly describes the definition of the vector fields including pathlines, streamlines, and streaklines and also reviews the techniques in 2D or 3D flow visualization. Section 2.2 provides required background knowledge, and research in fluid dynamics and terminologies relating to turbulent flows are discussed. Experimental acquisition and numerical simulation for the source of data are also

described. Section 2.3 discusses the vortex organization in turbulent boundary layers and vortex feature extractions in which advanced understanding about the vortices is shown.

This dissertation builds upon the cross knowledge in different discipline and cross techniques among current methods so as to effectively achieve our goals. In the next section, those materials of different knowledge and techniques are reviewed.

2.1 Flow Visualization

Flow visualization has been an important and active research topic in scientific visualization for many years. The vector data which need to be visualized could be acquired from the real world or numerical simulations. The applications of the flow visualization richly range in many areas such as aerospace, automotive and airplane design, chemical engineering, burning chambers, weather simulation and so on. In the following, the mathematical description of vector fields is defined, and different algorithms developed to visualize vector fields effectively are reviewed.

2.1.1 Vector Field Definition

In this section, we describe the formal definition of vector fields. In order to make it less abstract, space dimension of generalization in the formula has been reduced as three since the dimensionality of the space we'll visualize is two or three at most.

Let v be a map: $v: R^3 \times I \rightarrow R^3$, which defines a time-dependent vector field. The value of $v(x, t)$ is a vector in three dimensional space R^3 where x is a position in R^3 and t in I serves as a time description. Therefore, this vector field maps a point in three dimensional space and time, (x, t), to a tangent vector at the same location, x, in space.

Pathlines

Integral curves are important elements to depict the directional structure of a vector field graphically. Let σ_{x_0,t_0} be an integral curve for the vector field, v:

$$\sigma_{x_0,t_0}: J \rightarrow R^3 \quad (1)$$

under the condition:

$$\sigma_{x_0,t_0}(t_0) = x_0 \quad (2)$$

and

$$\frac{d\sigma_{x_0,t_0}(t)}{dt} = v\left(\sigma_{x_0,t_0}(t), t\right) \quad (3)$$

with the initial condition $x = x_0$ at $t = t_0$. The integral curve is usually termed as a pathline. The property of a pathline is that tangent vector of any position in this path is

the same to the vector in the vector field at that position. These curves are very important to be able to provide intuitive description to visualize and understand the vector fields of the flow. Streamlines and streaklines are two other types of integral curves for different specific flow fields or characteristics.

Streamlines

Streamlines are the integral curves generated in a static vector field. In steady flow field, a particle released in the flow field follows the streamline, which is identical to the pathline. The streamlines are given by:

$$\sigma_{x_0,t_0}: J \to R^3 \tag{4}$$

under the condition:

$$\sigma_{x_0,t_0}(t_0) = x_0 \tag{5}$$

and

$$\frac{d\sigma_{x_0,t_0}(t)}{dt} = v\left(\sigma_{x_0,t_0}(t)\right) \tag{6}$$

The curve is traced by a particle released from the position x_0 in the space at time t_0. The time parameter, t, of the field is reduced in the formula above since the flow is static in the steady flow. In unsteady flow field, we consider a snapshot of the flow field at a specific time, τ. The instantaneous flow field at a fixed time forms an artificial steady flow field and the streamline is, thus, defined by:

$$\frac{d\sigma_{x_0,t_0}(t)}{dt} = v\left(\sigma_{x_0,t_0}(t), \tau\right) \tag{7}$$

Streaklines

Streaklines are the curves that represent all the points which have previously flowed through a specific spatial position at the evaluated time. In other words, if fluid particles are released continuously from a fixed point, they constitute a streakline. The definition of the streaklines, η, could be formulated from the pathline, $\sigma_{x_0,s}(t)$, as following:

$$\eta_{x_0,t}(s) = \sigma_{x_0,s}(t) \quad (8)$$

The curve of streakline always evolves with respect to the different evaluated time.

The characteristic curves could be derived by the integration from the ordinary differential equation above which governs these curves. The integral formula for the pathline is:

$$\sigma_{x_0,t_0}(t) = x_0 + \int_{t_0}^{t} v\big(\sigma_{x_0,t_0}(s), s\big)ds \quad (9)$$

And the streamlines and streaklines are defined accordingly.

2.1.2 2D Flow Visualization

Flow fields could be very complicate to extract the meaningful information and display in an image. How to visualize and understand the characteristics in the flows has been an interesting topic for decades. 2D flow visualization is a good start for this purpose. A bunch of techniques have been developed to visualize 2D flow fields effectively.

There is no specific boundary which clearly separates the 2D flow visualization techniques from the 3D flow visualization techniques. However, many concepts of those methods are similar and could serve the underlying bricks of the 3D flow visualization methods. Therefore, basic review of some important methods in 2D flow visualization is fundamental to development of new methods.

2.1.2.1 Classification

There are different kinds of classification for the approaches to flow visualization. We adopt the work by Laramee et al. [8] to categorize strongly related approaches in a group as direct flow visualization, dense texture-based flow visualization, geometric flow visualization, and feature-based flow visualization based on different needs of scientists and different types of approaches.

2.1.2.2 Direct Flow Visualization

Direct flow visualization is a simple, fast, direct, and intuitive technique which can provide the overall picture of the flow data. Common approaches in this category are to plot arrows at each grid position encoding the information of direction and magnitude of the arrows representing the direction of the flow and the magnitude of the velocity at that location respectively. This technique is efficient because the simple glyphs are

placed in the discrete positions where the local features are extracted and rendered without any intermediate processing for the data.

Klassen and Harrington [9] suggest a fast technique, hedgehogging, to visualize 2D slices of 3D vector fields. The use of shape and shadowing disambiguate the orientation of 3D vectors visualized in 2D slices. Other tools are shown to be able to visualize the flow fields effectively. Ebert et al. [10] presents several tools to preview through the flow rapidly, highlight the features in the data with a specific transfer function, and render with the realistic model. Boring and Pang [11] highlight directional information as well as other properties. Flow data are encoded into different colors by using HSV color model, and the use of the light sources highlights the flow with similar directions. The change of the light parameters could emphasize some directions or a particular direction within a specified angle in the flow. Leeuw and Wijk's probe [12] visualizes many characteristics of the flow including velocity and velocity gradient tensor. This technique decomposes the velocity gradient tensor and visualizes it with the intuitive meaningful geometric objects.

2.1.2.3 Texture-based Flow Visualization

Techniques in texture-based flow visualization are very powerful. They usually generate the dense representation of flow fields from the initial dense noise texture, and the initial texture is normally convoluted along the movement of the vector flows in order to produce the visualization image with the co-related texture values at each pixel.

The dense representation of the resulting image could achieve complete coverage of the flow so that most detailed features of the flow could be visualized simultaneously. Laramee et al. [8] review the most important solutions in texture-based visualization which portray the complete and detailed information of flow fields and discuss the advantages and disadvantages of these techniques.

Spot noise proposed by Wijk [13] is a technique to provide the dense and detailed flow visualization by distributing the spots, intensity functions, into the 2D flow space randomly and summing their contributions. Enhanced spot noise [14] is proposed by Leeuw and Wijk to improve the spot noise algorithm in the highly curved field. Better visualization results are produced with the spots distorted in different shapes according to the local velocity in the field. Telea and Wijk [15] present a method which could generate the simplified representation of vector fields automatically. By varying the parameters in the algorithm, various simplified images on different aspects inside the vector field are produced according to the hierarchical clustering of the vector data.

Line Integral Convolution (LIC) [16] is a widely used dense texture-based visualization algorithm which could convey directional information in 2D flow fields effectively. Regarding spot noise and LIC algorithms, Leeuw and Liere [17] compare these two important texture-based flow visualization techniques and address the advantages, disadvantages, performance, as well as the output images of them. An extension of Line Integral Convolution proposed by Forssell and Cohen [18] could further support the curvilinear grids, unsteady flow, and visualization of vector magnitude. Pseudo-LIC [19] is proposed by Verma et al. to generate a variety of different outputs ranging from

the streamline-like to LIC-like images. Compared to the traditional LIC algorithm, PLIC produces similar results with high performance. It also avoids the multiple occupations in a pixel from different streamlines, and reduces the aliasing problem. Okada and Kao [20] present techniques to enhance or color the LIC images in order to highlight the areas of the flow where the separation or reattachment occurs. Although traditional LIC is powerful algorithm to portray the characteristics of the flow fields, it is limited from delivering the orientation of the flows. Oriented Line Integral Convolution (OLIC) [21] is proposed to encode the direction and orientation into an image by applying the anisotropic convolution kernel to the sparse input texture. Fast Rendering of Oriented Line Integral Convolution [22] enhances the performance of OLIC to achieve about two orders of magnitude faster over OLIC and also shows two efficient techniques to animate the FROLIC images. Another algorithm which could demonstrate more properties inside the flow can be seen in Kiu and Banks' work [23] which applies LIC to multi-frequency noises. This technique uses different frequency of noise texture and various lengths of convolution kernels to produce the image which provides better description of the magnitudes and direction of the flows.

The efficiency is an important issue since techniques to render the full coverage information of the flow are usually time consuming. Bordoloi and Shen [24] present a technique to provide the interactive vector field visualization. Their scheme utilizes the graphics hardware as well as the hierarchical technique to render the high resolution images at the interactive rate. Another work [25] demonstrates the application of the feature of the pixel textures in the OpenGL extension and presents the benefits in

scientific visualization to realistic image synthesis with the high quality and high performance capability. Stalling and Hege [26] present an improved approach of Line Integral Convolution (LIC) to speed up the LIC algorithm by using the simple uniform filter kernels and reducing the number of streamlines being calculated. The capability of visualizing the flow fields at arbitrary resolution of this method provides the useful animation of the flow at different level of details. A parallel algorithm of Line Integral Convolution [27] is also developed to provide the interactive visualization on the flow fields while all benefits of the sequential fast LIC are still retained.

2.1.2.4 Geometric Flow Visualization

The approaches in the category of geometric flow visualization usually integrate the flow data first and use geometric objects to describe the integration result of the flows. The integral geometric objects can portray the long-term behavior of the flow dynamics and reflect the properties of the flow such as pathlines, streamlines, streaklines, streamsurfaces, timelines, and so on. Another common geometric approach which is not based on the integration is the visualization of isosurface generated with respect to some quantities of the flow such as swirl values, magnitude of the vorticity, and so on.

In 2D flow fields, Turk and Banks [28] propose image-guided streamline placement to solve the most basic and difficult problem of determining the proper placement of each streamline by carefully selecting the seed points and length in order to evenly distribute the streamlines and capture the important flow features as much as possible. Jobard and

Lefer [29] present a method to create evenly-spaced streamlines at arbitrary density by allowing users to assign the distance of any two adjacent streamlines as a parameter. Compared to other methods, this method provides same image quality with better user's control and computationally efficiency. Jobard and Lefer [30] also develop a multiresolution technique to create a series of streamline images of a 2D vector field with different densities. This technique enables users to zoom in or out interactively while still maintaining the local density of the streamlines in the image space. It is efficient and effective because the streamline images with different densities could be computed in the hierarchical order. The preview of the top image could be done very early even though the streamline images with more details have not been produced yet.

2.1.2.5 Feature-based Flow Visualization

The approaches in previous categories directly convert the data to the visible descriptive components for users to perceive. These approaches rely on users' interpretation to the visualization of the flow data to acquire the understanding of the flows. The methods in feature-based flow visualization extract features from the flow fields, and compact information remains through the filtering process. The remaining important or critical characteristics in the flow fields are drawn with the proper glyphs, icons, ellipses, etc according to the type of the features [31].

2.1.3 3D Flow Visualization

Three dimensional flow fields are even more complex than two dimensional flow fields. Not only 3D characteristics in the fields are more difficult to capture and categorize but also effective visualization of flows in 3D space are hard to achieve. Distinct 3D techniques for visualizing volumetric flow fields have to be developed while some of 2D techniques can serve the basics. The methods of 3D flow visualization in this section are discussed based on same classification of the previous section about 2D flow visualization, which are direct flow visualization, texture-based flow visualization, geometric flow visualization, and feature-based flow visualization.

2.1.3.1 Direct Flow Visualization

In 3D flow field, the approaches that work well in 2D flow fields may not be effective because of the perception issues. In direct flow visualization, the position and orientation of the graphical primitives in a 3D space is more difficult to perceive due to the projection from 3D space to 2D plane. For instance, the perspective projection could supply the depth perception in 2D images. However, the length change in the rendered image may lead to the inaccurate judgment of the original graphical primitives such as arrows. The information of the depth and the length of an arrow are mixed, and the orientation information of arrows is limited to the image display. The issue of occlusion may also be introduced during the projection because the closer arrows may occlude the important farther ones.

2.1.3.2 Texture-based Flow Visualization

In texture-based flow visualization, a variety of powerful schemes has been proposed to visualize 2D flow fields. However, these may not be applied to the 3D flow fields effectively and directly. Helgeland and Andreassen [32] present a method to visualize 3D vector fields effectively by the use of several techniques. A scheme, Seed LIC, is used to compute volume LIC textures, Region of Interest (ROI) could mask the visualized area to highlight important features in the flow fields, and a shading technique, limb darkening, is applied to differentiating the individual lines within the ROI. Rezk-Salama et al. [33] visualizes 3D flow fields efficiently by using 3D-LIC with the direct volume rendering technique. This approach produces animation of the 3D LIC images with high frame rate by using the commercial graphics hardware and provides better perception of the flow fields for users. Interrante [34] presents an approach to illustrate surface shape of 3D flow fields by the solid stroke texture. The set of principal directions and principal curvatures are used to illustrate the flow by strokes for the surface inside the volume data. Interrante and Grosch [35, 36] present the strategies for effectively visualizing 3D flow fields by using 3D line integral convolution. Discussion covers the generation of the input texture, enhancement of the different elements, the depth perception of the objects, and highlight of the region of interest.

2.1.3.3 Geometric Flow Visualization

In geometric flow visualization, there are a variety of geometric objects used to describe the flow fields such as streamlets, dashtubes, streamlines, streamribbons, streamtubes, streampolygon, streamball, and so on. Some of them could only be applied to 2D flow fields and some of them could be applied to 3D flow fields. A thread of streamlets shown in Loffelmann and Groller's work [37] can visualize the 3D flow fields. This technique is a trade-off between the lower dimensional manifold for the display of structural information and the streamlines or stream surfaces for the direct representation. The lower dimensional manifold such as fixed points and separatrices may lose some information to be rendered. However, the streamlines or stream surfaces usually introduce occlusion problems. A thread of streamlets reduces the occlusion while still maintaining the important information in 3D flow fields.

Dashtubes proposed by Fuhrmann and Groller [38] are visualization icons which can be used to visualize 3D flow fields. A different mipmap technique supported by the graphic hardware is used to keep the texture in similar level of details along a streamline. Other tools like magic lenses and magic boxes provide the enhanced opportunity to visualize the details of the flow in specified areas. These techniques can reduce the common problems in 3D flow visualization such as occlusion of distant information, insufficiency of direction and depth clues, and occlusion.

A streamline is a common visualization technique of 3D fluid flow fields which describes a curve where a particle flows in the fields. The proper illumination on the

streamlines is very important so as to enhance the perception of visualization in 3D flow fields. The realistic shading model for lines provided by Zockler et al.'s work [39], which is not supported in the traditional graphics hardware, incorporating the lighting coefficients such as the ambient, diffuse, specular, and transparency enhance the quality and realism of the rendered images. High rendering performance is achieved by implementing this feature on the texture mapping capabilities of commercial graphics hardware, providing an interactive visualization with the illuminated streamlines. The way to accelerate the integration is also important. Teitzel and Ertl's work [40] propose and compare two algorithms of accelerating particle tracing on sparse grids and demonstrate an adaptive method to trace particles on curvilinear sparse grids.

Some geometric objects could demonstrate the special properties in 3D flow fields. The techniques of streamribbons and streamtubes presented by Ueng et al. [41] could visualize the rotation and expansion of 3D flow fields. The proposed algorithm constructs the streamlines, streamribbons, and streamtubes efficiently with the use of the specialized Runge-Kutta method. Another method called stream polygon [42] can be used to visualize local deformation. Streamball developed by Brill et al. [43] demonstrates the property of the divergence or convergence in 3D flow fields in the form of slitting or merging automatically. It can be applied in very complex flow fields or tensor fields.

Another geometric objects, stream surfaces, are also common in the in 3D fluid flow fields. In steady 3D flow fields, a stream surface is the surface where a curve moves. A method based on implicit surfaces by van Wijk [44] is proposed to construct stream

surfaces and could also support the construction of the stream volumes and time surfaces. This method is efficient with only some overhead in the initialization and could handle the irregular topologies of originating curves and surfaces easily. The issues of the placement of seed points are important to produce well-illustrative flow topology. A principal stream surface algorithm is proposed by Cai and Heng [45] to produce stream surfaces automatically and efficiently so that it can properly illustrate the flow topology without the careful placement of the starting points. Wijk [46] also presents a flexible technique of surface particles which could generate various geometric icons. Particle trajectories, stream surfaces, moving objects, stream tubes and so on are created by various initial properties of the source particles. High quality images and animations are achieved to make the flow more understandable.

In 3D flow visualization, to solve the problem of perception for hidden line occlusion and illumination of the field lines is an important issue. One of the first haloed line effect algorithms [47] is proposed to solve the depth discontinuities of hidden line, and an approach to illuminate the streamlines is proposed by Zockler et al. [39, 48]. Ye et al. [49] proposes a multi-step strategy to try to capture the critical structures of flow fields and reduce the clutter of streamlines by identifying the critical points and carefully placing the seed points in the space. They identify and extract the critical points in flow fields and apply different seeding templates to different critical points based on the various patterns around those points and the distance between the neighboring points. Poisson seeding is used to populate the rest of the space. Then, all streamlines are produced. Another technique developed by Mao et al. [50] is able to

create evenly spaced streamlines on 3D curvilinear grid surfaces and the technique based on the Turk and Banks' work [28] designs a new energy function to guide the placement of the streamlines in the computational space of the curvilinear grid with the specified local densities.

Teitzel et al. [51] compares and analyzes different particle integration methods with regard to the numerical efficiency and accuracy on discrete data of the unsteady flows. The selection of multiple integration algorithms is suggested based on the error of interpolation on the space and time and the error of numerical integration.

2.1.3.4 Feature-based Flow Visualization

The approaches in this category extract features in the flow and draw the important or critical characteristics by using the 3-dimensional elements such as glyphs, icons, ellipses, or others. Numerous feature extraction visualization techniques in this category have demonstrated in the works [52, 53]. Sahner et al. [54] extracts vortex core lines and use different colorful iconic representation to depict different scale and extent of the vortex cores.

2.2 Fluid Dynamics

This section serves as the required background of the knowledge and research in fluid dynamics with which we developed a variety of techniques shown in this dissertation. Thorough understanding of the properties and terminologies in fluid dynamics is very important for researchers to be able to properly utilize those characteristics to develop new techniques.

The explanation of the dataset used in this dissertation and the mechanisms used to acquire the experimental data are also included in this section. Although our work focuses on the processing and visualizing provided data, we can not neglect the origin and relating information about the source data.

2.2.1 Turbulent Flow

Turbulent flow is one of the unsolved problems of fluid mechanism in physics. Although pioneering research has been continuing for more than one hundred year, understanding of turbulent flow has not been completed yet. The explanation can be as following [55, 56]. The word turbulence evokes the sense of randomness. Turbulent flow is characterized by the chaotic, disordered, and stochastic changes of flow properties which involve the roiling and churning phenomena of swirling vortical structures and vortices. It can be expressed as flows in which the irregular motion occurs with the sufficiently high Reynolds number. The irregularity of turbulent flows

may be ether mild or severe. In general, any flow can be characterized according to its Reynolds number [57, 58] defined mathematically as

$$R_e = VL/v \qquad (10)$$

where V is a characteristic velocity, L is characteristic length scale, and v is the kinematic viscosity of the flow field. The empirical observation shows that the flow changes from laminar to turbulent when the Reynolds number exceeds a certain value called the *transition Reynolds number*, $(R_e)_{tr}$. Speeding up the flow will cause the increase of the flow Reynolds number. One way to make the flow turbulent is, thus, to speed up the flow until the flow Reynolds number exceeds the value of the transition Reynolds number.

In the following section, we'll explain some other terminologies and quantities in fluid mechanics which are very helpful to understand and analyze the turbulent flow within the boundary layer.

Boundary Layer

When fluids flow over a stationary flat surface, they are influenced by the solid surface affecting the neighboring fluids moving differently in comparison with the distant fluids. The fluids next to the solid surface will be retarded and be characterized by a shear stress [59]. This kind of phenomenon is always present when fluids move in contact with the solid surface. The flow field can be categorized into two regions, one inside the boundary layer and the other one outside the boundary layer. The flows inside the boundary layer are viscous and the viscosity of the flows outside the

boundary layer could be ignored. By using this classification, the solution of Navior-Stokes equations could be derived to achieve the significant simplicity as a closed-form in both regions.

Vorticity

A fluid particle may rotate around three-dimensional reference axes as it moves in a three-dimensional flow field. The rotation of a fluid particle can be measured by the angular velocity of the particle and can be expressed by the vector quantity, vorticity, containing three scalar components. Vorticity, denoted by the symbol ω, is a kinematic property in flow fields and is defined by the following equations.

$$\vec{\omega} = \frac{1}{2}\nabla \times \vec{V} \quad (11)$$

$$= \frac{1}{2}\left[\hat{\imath}\left(\frac{\partial w}{\partial y} - \frac{\partial v}{\partial z}\right) + \hat{\jmath}\left(\frac{\partial u}{\partial z} - \frac{\partial w}{\partial x}\right) + \hat{k}\left(\frac{\partial v}{\partial x} - \frac{\partial u}{\partial y}\right)\right] \quad (12)$$

$$= \frac{1}{2}\left[\hat{e}_r\left(\frac{1}{r}\frac{\partial V_z}{\partial \theta} - \frac{\partial V_\theta}{\partial z}\right) + \hat{e}_\theta\left(\frac{\partial V_r}{\partial z} - \frac{\partial V_z}{\partial r}\right) + \hat{k}\left(\frac{1}{r}\frac{\partial r V_\theta}{\partial r} - \frac{1}{r}\frac{\partial V_r}{\partial \theta}\right)\right] \quad (13)$$

where vorticity is expressed in Cartesian and cylindrical coordinates by equation (12) and (13) respectively. In reality, the vorticity ω is as twice as the angular velocity of a fluid particle [57].

Vortex

A vortex is a rapidly swirling motion of flow around a center. The greatest rotation speed and the lowest fluid pressure are located at the center and decreases or increases respectively according to the distance from the center. Vortices usually appear in the

boundary layer where small masses of fluid are animated up and down to move toward the direction of mean flow and the direction perpendicular to the boundary surface. The faster fluids in the higher-speed regions are convected into the lower-speed regions by the vortices, increasing the speed of the fluids near the laminar sublayer. On the other hand, slower fluids are raised into the higher-velocity regions and decelerate the speed of those areas, expanding the thickness of the boundary layer [59].

Swirl Strength

Swirl strength could be used to determine the connected region of vortices and is calculated based on the velocity gradient tensor. The imaginary part of the complex eigenvalues of the complete velocity gradient tensor is suggestion of the local swirl strength for identification of the vortex regions [2, 3, 60] and is considered as the three-dimensional swirl strength. Two-dimensional swirl strength is calculated based on the two-dimensional velocity gradient tensor. The simplified version of swirl strength is used in the case in which the complete velocity gradient tensor is not available. Therefore, the two-dimensional swirl strength is defined as the imaginary part of the complex root which is the characteristic equation of the two-dimensional velocity gradient tensor [61].

2.2.2 Particle Image Velocimetry

The conventional particle image velocimetry (PIV) is a technique that employs imaging to experimentally measure a rectangular grid of the related properties and instantaneous components of a velocity field within a flow plane in a moderate to high Reynolds number [62, 63]. Passive tracer particles are added into the investigated flow in a non-intrusive way and are tracked with the fluid motion. Sheets of light cast from high-energy pulsed lasers illuminate these particles in a plane of interest at least twice within a short time step. Then, a camera which is synchronized with the laser pulses captures the light scattered by the particles in two images. The cross-correlation algorithm is applied to the image pair to determine the velocity vector field within a plane.

The standard PIV records the velocity vectors projected into a plane. Stereoscopic PIV, which eliminate the errors of the perspective problem [64, 65], is capable of reconstructing the out-of-plane motion of particles from different recordings and extracting three-dimensional velocity fields by utilizing two cameras recording simultaneously with different viewing directions [66, 67]. This technique works generally well but still has its inherent characteristics in which in-plane components are more accurate compared with the accuracy of the out-of-plane components.

2.2.3 Direct Numerical Simulation

Direct numerical simulation (DNS) has been a useful research tool for the analysis of wall-bounded turbulent flows during the past decades. The complicated behavior of turbulent flows is inherited from a set of equations named as the Navier-Stokes equations. However, the closed forms of the analytical solutions for the turbulent flow are not available. Direct numerical simulations are calculated by solving Navier-Stokes equations numerically and are capable of providing global descriptions of the turbulent flows from low to moderate Reynolds number in terms of space and time. Significant investigation into turbulent flow dynamics could be conducted with DNS of particular flows that can not be easily produced experimentally in the laboratory.

2.3 Vortex Organization and Extraction

This section provides the advanced discussion about the vortices in turbulent boundary layers. We focus on the research of the coherent structures in the turbulent flow and the various schemes of identification of the vortices. Different turbulent structures with respect to the properties of the flow and their correlations are examined. Feature extraction methods explain the taxonomies of vortex detection methods and discuss most popular schemes based on these taxonomies.

2.3.1 Vortex Organization in Turbulent Boundary Layers

Research in coherent structures in turbulent boundary layers has long been an interesting research area and usually relies on single or two-point hot-wire measurements as well as visualization in turbulent flow fields. Recent research relies on various flow quantities which are computed from direct numerical simulation (DNS) at relatively low Reynolds number, and particle image velocimetry (PIV) is used to acquire data at moderate to high Reynolds numbers.

The structure investigation in boundary layers could be traced back to several decades ago. The elongated streaky structures in the region near the wall of a turbulent boundary layer are identified and investigated in the 1950's [68, 69]. Corino and Brodkey [70] as well as Kline et al. [71] concentrate on the fluid motions very near the wall while character of fluid motions changes with respect to the distance from the wall. They observed the low-speed streaks on the near-wall region, which can trigger oscillation, bursting, and ejection to be as the dominant factors for the turbulence production and transport within the boundary layers. Cantwell [72], Robinson [73], and Panton [74] have done good literature reviews on the presence and role of coherent structures in wall turbulence. The near-wall turbulence has received the most scrutiny since more than half of the total turbulent energy is produced in the first 5% of the boundary layer. More recently, a various articles [75, 76] have used direct numerical simulations as datasets and have concentrated on analyzing the viscous near-wall region and the self-sustaining mechanisms in wall turbulence. The importance and existence

of hairpin-shaped vortices in the outer region of the flow have been first addressed in closely relating work by Theodorsen [77]. Head and Bandyopadhyay's result [78] strongly supported the existence of hairpin vortices in turbulent boundary layers. Their evidence motivated Perry and Chong [79] to develop a model for the mechanism of wall turbulence such as hairpin vortices based on Townsend's [80] attached-eddy hypothesis. Later, Perry and Marusic [81] extended the vortex model by using the modified hypothesis and incorporating both wall structure and wake structure into the model.

More recently, Adrian and co-workers [3, 82-84] have performed PIV experiments and have used direct numerical simulations (DNS) of a turbulent channel flow to find coherently organized hairpin vortices. They showed hairpin vortices in the outer layer are organized coherently in streamwise-aligned packets and the appearance of the hairpin vortex packet provides the explanation of the existence of long low-speed streaks, sweeps, and ejections that a single hairpin vortex can not account for. Christensen and Adrian [85] used linear statistic estimation and Marusic [86] used attached-eddy model calculations to support that hairpin vortex packets, which populate in the outer layer of wall turbulence along the streamwise direction, are statistically significant mechanism for Reynolds stresses and transport momentum in the logarithmic region. Same evidence in Ganapathisubramani et al.'s work [87] by using stereo particle image velocimetry (PIV) measurements and the feature extraction algorithm also shows that hairpin vortex packets may carry a significant amount of total Reynolds shear stress even though they occupy only a small portion of the total streamwise-spanwise area. In addition, mean values of spanwise lengthscales vary

linearly with respect to the distance from the wall and present the self-similar growth of spanwise structure by merging of neighboring vortex packets [83].

Research on rough-wall turbulent boundary layers is also a very important area in relation to environmental, geophysical, industrial, and transport applications. Jiménez [88] proposed ways to model rough walls without requiring detailed design and computation of the roughness elements by reviewing the existing experiments on the effect of rough-wall turbulent boundary layers. Schultz and Flack [89] showed that strong sweep events increase and strong ejection events decrease near the rough-wall layers by using quadrant decomposition. However, the flow properties such as mean velocity and turbulence effect in outer region appear to be independent of surface roughness, showing the high similarity with the results of smooth walls in that region. Also, recent experiments on PIV measurements performed by Wu and Christensen [90] have shown that wall-normal velocity may be correlated over streamwise velocity within the roughness sublayer. This might indicate the change of the underlying spatial structure of the flow in the rough-wall region although the exact cause for this phenomenon is still vague. Flores et al. [91] performed direct numerical simulation of turbulent channel flows over both the rough and smooth walls and found that the roughness of the wall had little effect on their properties especially for the geometrical and spatial distributions of wall-detached and wall-attached vortex clusters, indicating the independence of the details of the wall. Coceal et al. [92] investigated the turbulent flow over regular cubical roughness and observed that the hairpin-type vortex packets were much larger to those in smooth walled flows but not in the low momentum

regions. Another phenomenon has also been shown in which the vortices shed from the sharp edges of the cubical obstacles dominate the turbulence.

2.3.2 Feature Extraction Methods

Development of efficient and effective schemes for illustrating information in 3D turbulent flows has long been an important research area in the field of Visualization since McCormack's work [93]. A feature in a dataset is a kind of pattern which represents some correlation inside the data. Features in scientific data are usually expected to be defined precisely. However, some of them could not be defined in an exact expression. For example, a vortex is a feature in fluid dynamics in which the formal definition is not found. During the past decades, significant effort has been dedicated to the solution of developing reliable schemes for effectively identifying and visualizing vortical structure in 3D flow fields [53, 94]. Numerous vortex detection algorithms have still been proposed to identify most vortical structures in flow fields although the complication and reliability of these schemes are closely bound up to the lack of a sufficiently robust and precise mathematical definition of a vortex. Post et al. [53] presented various feature extraction techniques according to the type of features such vortex extraction, shock wave extraction, and separation and attachment line extraction. Algorithms of feature tracking and event detection are proposed in order to understand the evolution of features in unsteady flow fields. The results are visualized by different visualization techniques. Roth's thesis [95] and Jiang et al. [94] provided

the overview of the existing vortex detection methods. Jiang et al. also classified those methods based on three different taxonomies. Firstly, the definition of a vortex is used to classify the detection methods. A vortex can be defined as a region or a line and identified by the region-based algorithms and line-based algorithms respectively. Secondly, detection methods are classified according to the property of Galilean invariant. If a constant velocity is added to the flow fields and the result of the detection method is the same, this method is Galilean invariant. Thirdly, the classification of the taxonomy is based on the local or global detection methods. If the decision of the detection method is made only according to the computation of the local data such as velocity gradient tensor, it is considered local. If the detection method involves a large range of the grid cells such as the streamline integration, it is categorized as a global method. The geometric verification scheme is also addressed [96].

Region-based vortex detection methods could identify regions of vortices in the flow fields. Swirl-strength method [2, 3, 60] computes the swirl values. If the swirl values are greater than zero, these areas indicate the existence of swirling motion and vortex cores appear in the local maximum location of swirl values. This threshold level based method is one of the most popular methods for identifying vortices by using Galilean-invariant scalar quantity derived from the velocity gradient tensor. As the swirl-strength method, Lambda2 [97] could also detect the region of the vorticies. Some other quantities such as Q criterion [98] and ∇ criterion [99] are also used in similar ways. Q-criterion defines vortices as regions satisfying $Q = \frac{1}{2}(\|\Omega\|^2 - \|S\|^2) > 0$

where $S = \frac{1}{2}(\nabla V + (\nabla V)^{\mathrm{T}})$ denotes the rate-of-strain tensor and $\Omega = \frac{1}{2}(\nabla V - (\nabla V)^{\mathrm{T}})$ denotes the vorticity tensor. ∇-criterion defines vortices as regions satisfying the discriminant $\nabla = \frac{1}{2}\left(\left(\frac{Q}{3}\right)^3 + \left(\frac{\det \nabla V}{2}\right)^2\right) > 0$ and ∇V has one real and two complex eigenvalues. The above vortex regions identified by different quantities are shown to be very similar by Chakraborty *et al.*'s recent analysis [100]. Besides, Robinson [73] researches the coherent motions in turbulent boundary layers to construct predictive modeling of turbulent flows, to control the turbulent flows, and to illuminate for dynamical phenomena. The problem of the region-based vortex detection method is that an appropriate threshold level is required to demarcate the vortex region boundary. Successful identification for individual vortices could not be achieved if the chosen threshold level is not appropriate, the several vortices are too close, or some of the vortices are too weak. Alternatively, Bauer and Peikert [101] proposed a method based on the scale-space computation in order to improve the extraction of features.

Line-based methods [102, 103] are the other type of methods which could detect the vortex core lines. A promising identification method of vortex core lines [104, 105] is the predictor-corrector technique proposed by Banks and Singer [106]. In this method, vorticity is used to predict and perform the integration of the vortex core lines and the local pressure minimum corrects the location predicted by the vorticity from the last location. The predictor-corrector steps terminate when the corrected location is too far from the predicted location. An eigenvector method [107] proposed by Sujudi and Haimes extracts the vortex core lines by examining the eigenvalues and eigenvectors of the velocity gradient tensor and determining the local flow pattern. The combinatorial

method proposed by Jiang et al. [108] determines the cells which belong to the vortex core based on the Sperner's Lemma derived from the fixed-point theory of combinatorial topology. Roth and Peikert [109] introduced parallel vectors operator to extract vortex core lines. Eigenvector method is transformed into checking the parallel alignment between velocity, *v*, and its first derivative, J_v, in order to prevent explicitly solving an eigenvalue system. To improve the extraction of the vortex core lines achieved by the first-order eigenvector method, higher-order derivatives are taken in to account. The second derivative of *v* with respect to the tensor of second derivatives, *T*, is used and defined as:

$$w = \frac{D^2 v}{Dt^2} = \frac{Da}{Dt} = \frac{D(Jv)}{Dt} = JJv + Tvv, \text{ where } T_{ijk} = \frac{\partial^2 v_i}{\partial x_j \partial x_k} \quad (14)$$

A vortex core line is the region where velocity, *v*, is parallel to the second derivative w: $\{x: v(x) \times w(x) = 0\}$. A multistage vortex visualization algorithm [110] visualizes the vortex core line and its auxiliary information in four stages. The first stage is to search the cells intersecting the candidate vortex cores. The second stage determines the vortex core line. The third stage is to examine the vortex characteristics such as extent, position, strength, etc. The fourth stage is to visualize them. Some recent researches [111-113] have shown the effort to define frame-independent criteria for vortex by the use of Lyapunov exponents and Lagrangian coherent structures.

This paper [54] presents an approach to extract vortex core lines independently of the frame of reference by extracting ridge and valley lines of Galilean invariant vortex region quantities and uses an iconic representation for indicating their scale and extent. This technique simply combines the Galilean invariance of the vortex region detection

with the parameter independence of the vortex core line extraction. Feature flow field extraction scheme is used to extract the vortex core lines with respect to the Galilean invariance of the vortex region quantity from the seed points. This work provides a new innovative scheme for extracting the vortex core lines. However, it involves the first and second derivatives of a three-dimensional discrete real function as well as the computation of eigenvectors, making the inaccurate results in searching of seed points and integration of the feature flow fields.

Chapter 3

Visualization Methods

There is keen need for visualizing interesting areas and inspecting properties corresponding to multiple variables within those regions since the behaviors of the flow have not yet been well understood by scientists. Due to the lack of the thorough understanding of the fluid dynamics in turbulent flow fields, we aim at facilitating the integrated understanding of a variety of local measures extracted from 3D multivariate flow data, including quantities, directions, and orientation. We develop methods for illustrating the local relationships between scalar and vector values important to the vortex identification process such as vorticity, swirl, and velocity, along with their direction and magnitude. Our methods include the use of arrows and glyphs or 3D texture along with different color coding strategies. We demonstrate our methods on a range of data including 3D turbulent boundary flow data and time-varying ring data. The variety of multi-variate visualization methods that we have developed has succeeded in supporting fluids researchers in their efforts to gain deeper insights into these data. In this chapter, we first introduce two datasets we use. Then, we explain the

ways to identify vortices and isolate each of them. After that, we present direct flow visualization techniques on the vortex region by using 3D arrows with various colors to convey multiple variables. Finally, we will explain our LIC glyph method and also demonstrate its results on these two datasets.

3.1 Direct Numerical Simulation Dataset

The turbulent flow dataset we investigate in this dissertation is the direct numerical simulation of fully developed plane in a turbulent channel flow produced based on the work made by del Alamo et al. [1]. The dimension of this dataset is 263 × 393 × 192. Figure 3.1 shows the entire channel flow in a plane, and the rectangle in the upper left side is a sub-region extracted from Renolds number 934 for our dataset. The colors in this figure represent the different velocity speeds with the higher speed in red areas and lower speed in blue areas. Our dataset covers high and relatively low speed areas and provides enough variation in the flows. The data include three velocity components, swirl, and discriminant at each grid location. The three-dimensional velocity vector (u, v, w) represents streamwise velocity, spanwise velocity, and wall normal velocity respectively.

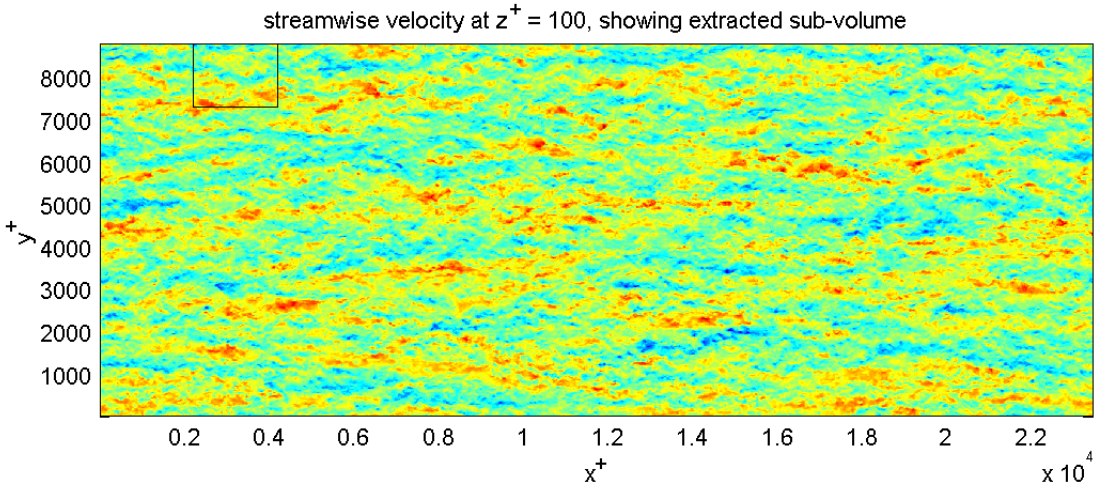

Figure 3.1: The entire turbulent channel flow in a plane. The rectangle in the upper left side shows a sub-volume of our dataset. Red and blue colors represent higher and lower speed areas respectively.

3.2 Time-Evolving Vortex Ring Dataset

The time-evolving vortex ring dataset used in this dissertation is provided by Dr. Daniel R. Troolin and Dr. Ellen K. Longmire [114]. The vortex ring data are produced by driving pistons within a circular cylinder whose inner diameter is D = 72.8 mm and are experimentally captured 3D time-varying flows with 70 time steps. The pistons are driven at a constant velocity over a distance L = D, and the Reynolds number is 2500. The inclined exits of the cylinder make the circular downstream flow much more complex. This dataset includes three velocity components at each regular grid location. Other quantities or vectors such as swirl strength, vorticity, etc. are computed based on these three-dimensional velocity components. Volumetric 3-component velocimetry (V3V) is used to examine this time-evolving three-dimensional flow, capturing details

of the flow structures and providing researchers a set of useful flow data. Several vortex rings are introduced and observed in this measurement. The major one appears first from the inclined nozzle as a primary vortex ring. There may be two vortex rings which are developed inside the cylinders, then, later interacted with the primary vortex ring, and finally tend to breakdown.

3.3 Vortex Identification

In this section we apply one of the vortex region detection methods to identify all vortices in the entire volume flow fields and isolate each vortex in order to conduct further visualization and analysis for each single vortex.

3.3.1 Vortex Region Identification

Among various quantities which indicate the existence of the vortices in a turbulent flow, the most popular one, swirl strength [2, 3, 60], is applied to identify vortex regions in this dissertation. There are some advantages supporting our selection for this method. Firstly, this quantity is Galilean invariant or frame independent so that effort to select the proper reference frame is reduced. Secondly, the complex eigenvalue pair exists only in the regions where local swirling motion appears so this excludes the areas appearing the existence of vorticity without any circular motion such as shear layers. The traditional iso-surface extraction method [115] is applied to our dataset with respect

to the swirl strength shown in figure 3.2. This figure contains an entire view of the channel flow and shows that there are more vortices identified near the wall areas indicating that the flows closer to the wall are more turbulent. A close-up of the turbulent channel flow is shown in figure 3.3. We can also notice that the vortices near the wall are more complicate in which not only the structure of the vortices are irregular but also more than one vortex join together while the vortices farther to the wall are simpler.

Figure 3.2: An entire view of vortices in a turbulent channel flow identified by iso-surface extraction on swirl strength.

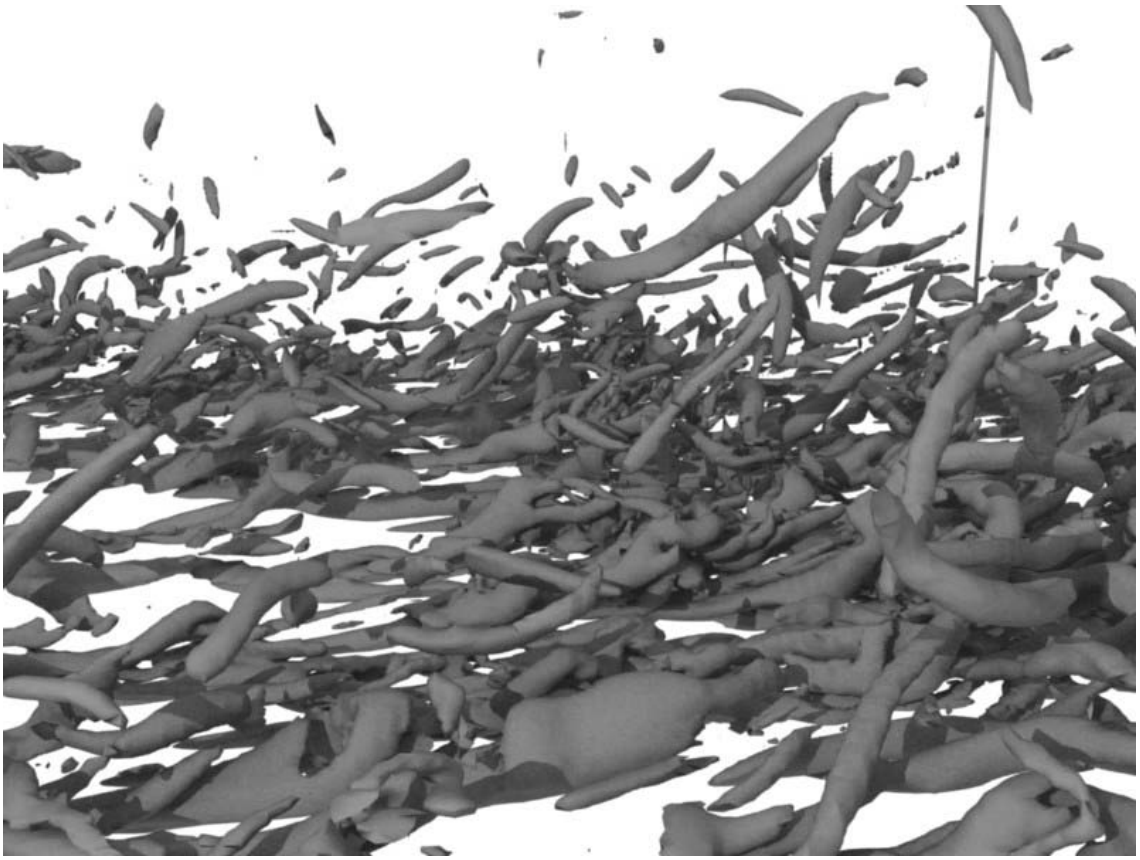

Figure 3.3: A close-up view of vortices in a turbulent channel flow identified by iso-surface extraction on swirl strength.

3.3.2 Individual Vortex Identification

In the previous section, a variety of vortices have been identified by the vortex region detection method and are located near the wall. In order to further investigate each vortex individually and carefully, an intuitive separation algorithm has been applied to the flow dataset. The separation algorithm scans the grid cells in the entire dataset sequentially in order to check the connectivity of each part of vortex inside each cell by examining the topology of each cell according to quantity values at each cell vertex

with respect to the predefined threshold level. The rendering system could filter all other vortices based on the connectivity information and render the remaining interesting vortex.

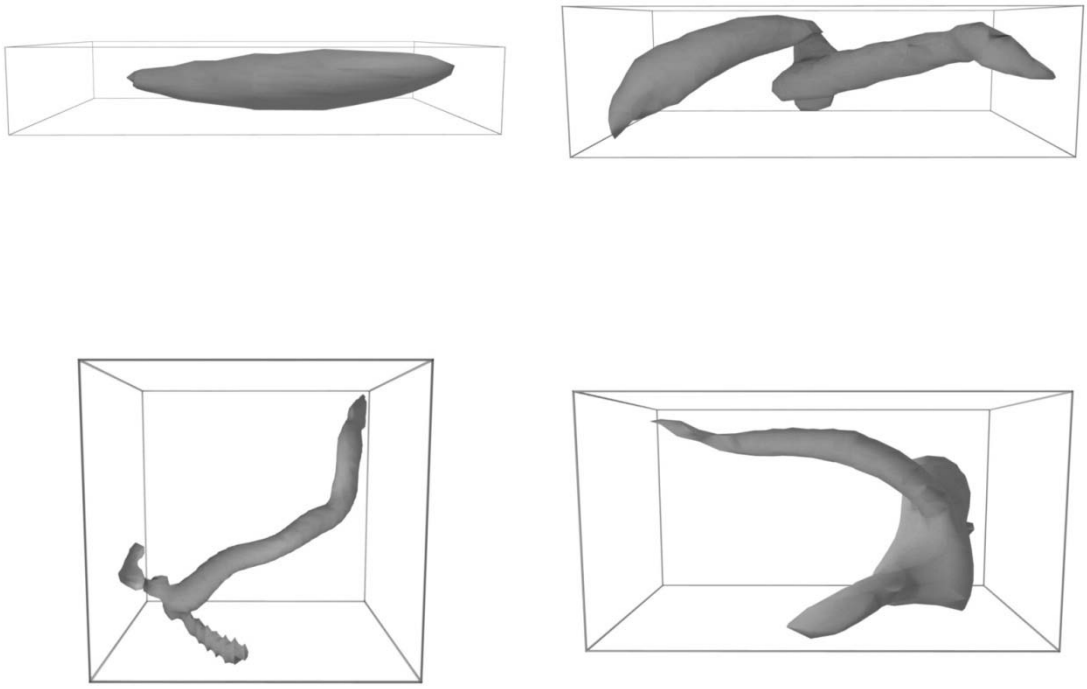

Figure 3.4: The upper left image shows a vortex with simple structure. The upper right image shows a connected region form by two individual vortices touching each other. The lower left image shows a region with several complicated elongated structures. The lower right image shows a complicated clump containing multiple interacting structures.

The upper left image in figure 3.4 shows a simple elongated structure of a vortex with a little bit bending. The upper right image in figure 3.4 shows a connected region formed by two roughly symmetric elongated structures touching near the one end. The vortices of two lower images in figure 3.4 are more complicated with more irregular parts.

There are at least three elongated tubes in the vortex in the lower left image in figure 3.4, and the length of each tube varies. The lower right image in figure 3.4 shows a complicated clump containing multiple interacting structures.

3.4 Vortex Feature Visualization

The vortex region identification method could detect the swirling regions in turbulent flow fields. However, it does not provide any details of the flow within the vortex regions. In this section, we describe our efforts to help researchers to better understand relationships between local measures of vorticity and other possible measures of swirling motion through the use of visualization methods involving 3D arrows, glyphs, geometric objects, and various color coding schemes.

3.4.1 Direct Flow Visualization

We demonstrate the use of the direct flow visualization techniques on a vortex region of interest, by using 3D arrows with different colors to portray multiple variables. The simplest and most intuitive visual objects in direct flow visualization are arrows. Three dimensional arrows are constructed here, and graphics rendering for 3D arrows provides shading effects automatically. Figure 3.5 shows two categories of arrows, red and blue, which represent the vorticity and swirl (rotation plane normal) directions respectively. The heads of the arrows in this figure are rendered with fully saturated primitive colors

while the bodies of the arrows are half saturated. All of the arrows are placed at the sample locations encompassed by transparent surfaces representing the outline of a region of high swirl strength. In this figure, the directions of vorticity and swirl are visualized only at the points where the swirl strength is larger than a certain value. However, this scheme can not satisfy our need for investigating the angle between these two types of vectors at each grid location. Therefore, we vary the colors of the 3D arrows' heads to provide one more dimension of color representation, by transitioning an arrow's original color toward a common purple color according to the angle between the two vectors at the same location. As the angle between the vectors becomes small to non-existent, the head colors of the pair of arrows become similar or indistinguishable. When this occurs, these two arrows tend to be very nearly overlapping with each other; however the particular variable each arrow represents can still be recognized by the color of its body. Figure 3.6 shows this visualization in both far away and close-up views. In this figure, the head colors of 3D arrows are linearly interpolated according to the maximum and minimum of all angles in the entire region of interest. If the extreme values occur only in some isolated cases, those minor cases may cause the color distribution of the remaining arrows to be less distinguishable. Thus, we vary the colors based on boundary values which are twice the standard deviation away from the mean value. Figure 3.7 demonstrates the use of this method to achieve more noticeable variations of colors for the change of angle difference.

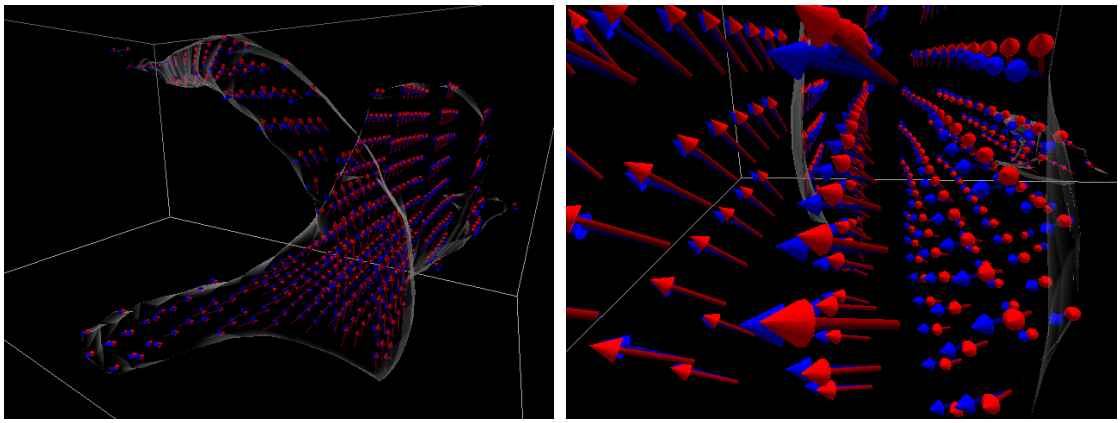

Figure 3.5: Left figure shows two categories of arrows, indicated by distinct red and blue colors. The red arrows show the vorticity direction and the blue arrows show the normals to the rotation plane defined by the swirl. Right figure provides a close-up view of a central portion of the image on the left.

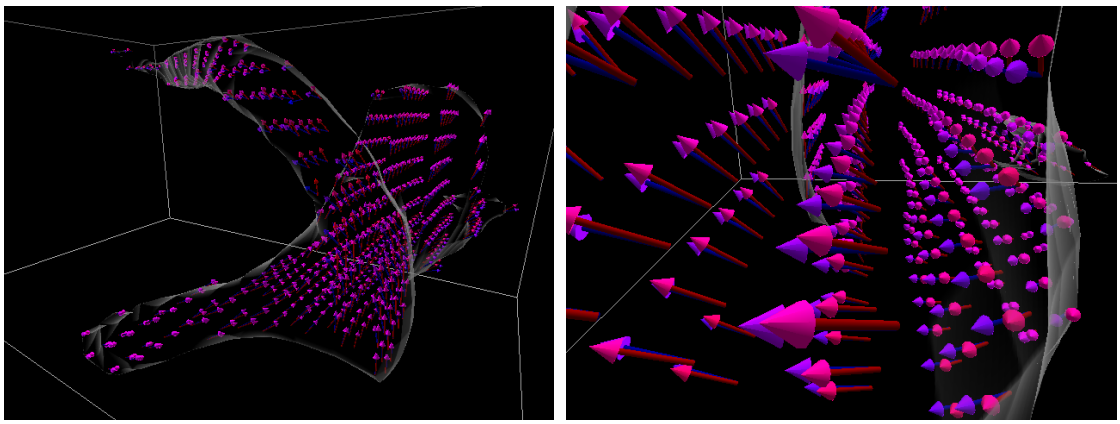

Figure 3.6: In these images, the colors of the arrow heads are defined using a weighted common mixing color (between red and blue) according to magnitude of the angle between the paired vector values. Vectors that are more aligned have more similarly colored tips. The shafts of the arrows remain rendered in the original colors (red and blue).

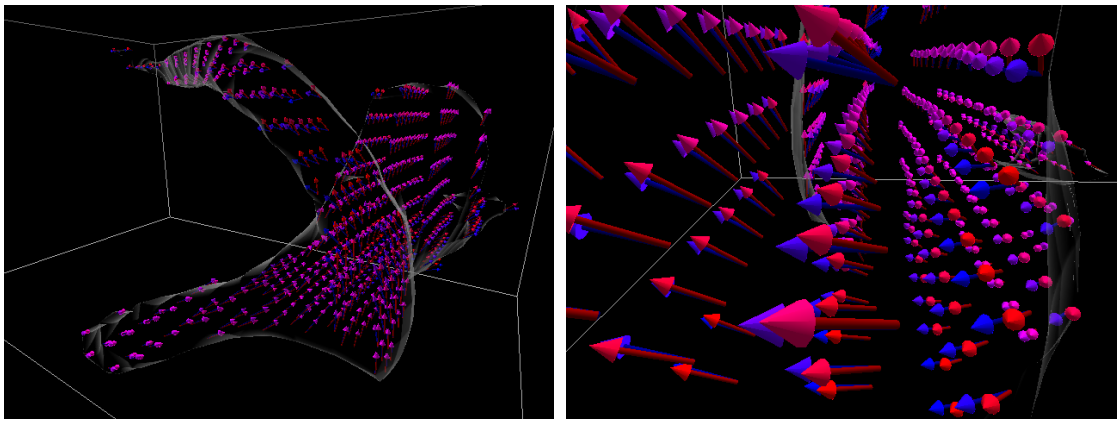

Figure 3.7: Here the colors of the arrow heads are defined using a weighted common mixing color (between red and blue) according to magnitude of the angle between the paired vector values, with the interpolation occurring between boundary values that are twice the standard deviation away from the mean angle size.

3.4.2 LIC Glyph Method

We have developed a novel technique, LIC glyph method, in this section in order to convey more information at more locations in one image without regular patterns at each grid as shown in 3D arrow visualization. The LIC glyph method technique could portray the flow information inside the interesting region such as vortices. These kinds of information help researchers to understand and analyze the behaviors of the turbulent flows and possibly further predict them.

3.4.2.1 LIC Glyph Algorithm

The essential steps in our LIC glyph algorithm, which have the potential to provide vivid and effective visualization within interesting regions, are described in figure 3.8 and below.

1. Identifying Interesting Areas

We begin by identifying interesting regions in the flow, within which we wish to visualize detailed local scalar and vector information. These regions can be defined in a variety of ways. The simplest approach is to manually select a rectangular subset of grid cells that appears to contain potentially interesting flow features, based on a pre-visualization of a single scalar feature of the data such as swirl strength [2, 3, 60]. However, we have also implemented a method that automatically defines target regions for visualization around connected subsets of sample points where the swirl strength is above a specified threshold value. This design for automatically detecting and separating particular regions throughout the entire space assists researchers to identify the most important areas for investigation and also allows for further developing an automatic mechanism of this algorithm to define all of the interest targets.

2. Super Sampling

The next step is to super-sample the data within the target region, in order to provide sufficient resolution for the effective portrayal of local 3D scalar and

vector data using glyphs. Both of the turbulent flow datasets we are working with are discrete, and in the turbulent channel flow dataset each of the thousands of critical regions in it may occupy only a few grid cells. In order to provide highly detailed information in these areas, a super sampling step is required to accommodate a reasonable number of high resolution glyphs distributed throughout each of the regions. However the level of super sampling has to be chosen carefully. A lower level of super sampling will provide higher efficiency performance, but the glyphs may not be capable of delivering finely enough detailed information. On the other hand, a higher level of super sampling enables conveying more information with more glyphs, but the computational efforts may be extremely large. Moreover, extremely high interpolation of the data may introduce unwanted side effects. Therefore, some tradeoff has to be made according to the computation speed, memory usage, and disk capacity.

3. Generate 3D Texture

In this step, we generate a 3D texture within the regions of interest, consisting of multiple spherically-shaped particles (Gaussian balls) seeded at randomly selected locations but maintaining a minimum separation, approximating a Poisson distribution. The purpose of this distributed particle placement is to prevent artifacts caused by particle conglomeration while providing an equal opportunity for every location to be occupied by a particle. Keeping the seed points apart by a certain distance is required to avoid the chance of overlapping particles. This has to be done carefully to maintain the particles still dense enough in the space.

4. Region-of-interest Mask

We typically apply a region-of-interest mask to the input texture before conducting the LIC in order to reduce the number of particles and to preferentially emphasize the display of information in the areas of particularly strongly swirling flow. This step placed ahead of the 3D LIC step is capable of limiting the processing areas within certain regions so as to enhance the efficiency of the algorithm, which has been addressed in Interrante's work [34-36]. All the particles within the mask remain in the process to be visualized later.

5. 3D LIC

Once the particles have been distributed into the space, as densely as possible but with a certain distance between each other and a region-of-interest mask has been applied to filter out some unneeded particles, we perform 3D line integral convolution (LIC) [16, 26] with a small kernel size throughout this area, following tangent curves through one of the vector fields. This process causes the originally spherical particles to become elongated in the direction locally specified by the vector field while allowing the particles to assume a non-linear shape in areas where the flow direction is changing rapidly, providing important hints of the vector direction throughout the space.

The selection for the size of the filter kernel is based on the density of the particles produced in step 3. If the size of the kernel is too large, neighboring particles warped into elongated shapes could touch each other, forming unclear and

unexpected conglomerate particles. If the kernel size is too short, the shape of the particles will not be distinct and the glyphs will not represent the local vector field in a clear manner. For the images shown in this paper, we selected the kernel size as long as possible while keeping most neighboring LIC glyphs separate.

6. Auxiliary 3D LIC

The regular LIC algorithm uses uniform (box) filters to integrate streamlines in vector fields, which we can apply to different vector fields with the 3D texture to deliver information about the fields through the shape of the 3D glyphs. Non-uniform filters can also be applied in order to generate auxiliary information about the direction of the flow. This auxiliary information could be used in the implementation of different color coding methods so as to encode rich information on the 3D LIC glyphs. The technique we use is similar to the thick oriented stream-line algorithm developed by Sanna et al. [116] in which a monotonically increasing luminance ramp is used to depict the direction of the flow.

7. Outline Creation

All of the visual objects created in this algorithm are located within the identified interesting regions defined by strong swirl strength areas. Outlines are created to depict and encompass the interesting regions by using the traditional iso-surface extraction technique. Outlines are implemented by making the extracted surfaces fully transparent when they are orthogonal to the line of sight but more opaque when they are viewed at a grazing angle, making them fully transparent in the

central regions but not at the boundary. This method enables effectively conveying the boundaries of the regions of interest without occluding major parts of their interior.

8. Color Coding for Features

Various types of color coding are used to visualize the LIC glyphs in order to convey additional information. These are described as follows.

Color coding for vector direction – Step 6 applied non-uniform filters to vector fields to produce auxiliary information indicating the direction of the flow. The produced convolution result is skewed and provides the additional information that is utilized by the color coding methods. A transition of colors is painted on the surfaces of the LIC glyphs, in which the color at each point is defined by referencing the different skewed values at the locations on the glyph surfaces and looking up the corresponding color in a rainbow color scale shown in the top left image of figure 3.9. A nearly perceptually linearlized rainbow color scale that ranges from white to purple could deliver the vector direction easily and clearly according to the variation trend of the colors on the glyph surfaces, with the white portions indicating the leading part of the glyph with respect to the vector direction around this glyph area.

Color coding for vector direction and orientation – This method applies two main colors to glyph surfaces in order to represent information about vector direction and orientation similar to the 3D color wheel scheme by Hall [117]. We first

create a unit sphere given different colors for each location on it and position this sphere's center at the origin. Different color models can be used here. For the first model, we use a blue color varying according to the vertical axis (180º) and red and green colors varying according to the horizontal axis (360º) as shown in the top right image of figure 3.9. The second model uses the HSV color model to define the hue according to the horizontal direction and the luminance according to the vertical direction, constrained to range between 0.5 and 1.0 in the value channel as shown in the bottom right image of figure 3.9. Then, we decide one main color by looking up colors on these spheres according to the direction a vector points from the origin. The color coding in this method transitions from a main color, representing the vector orientation, toward white, representing the vector direction, and colors on the glyphs are given by referencing the auxiliary information produced in step 6 with respect to the color scale here.

Color coding for scalar value – This color coding strategy uses transparency to represent how a scalar value varies in the interesting regions. This method allows a color in the surface to be transparent according to the value of a scalar variable. When the scalar value is large, the glyphs become opaque and prominent. Otherwise, the glyphs are transparent and obscure. This technique can be combined with other techniques described above to convey one more dimension of information. Color coding method by using color saturation can be designed in a similar strategy as shown in the bottom left image of figure 3.9.

9. Other 3D Visual Primitives

We also use 3D arrows to help deliver vector information. Basically, the arrows are placed at grid positions. Different dimensions can be represented according to the orientation, colors, and lengths of the arrows. We may use more than one arrow at the same grid location, to representing the values of different vector variables at that point, so we use distinct colors for each arrow to distinguish different categories. We use the most saturated color for the arrow head while rendering its shaft in a half-saturated version of the same color to avoid visual overload. We can also vary the color of an arrow head to convey additional information while the color of its shaft remains the same.

10. Proceeding for another Time Step

This algorithm could be applied to either static flows or time varying flows. If the flow data involve different time steps, we need to jump to the first step to proceed with the same algorithm for the next time step until all of the data have been rendered.

11. Rendering

This step renders the 3D visualization result, which is either one static image when the input is a single time step or a series of images when the input is a time varying dataset.

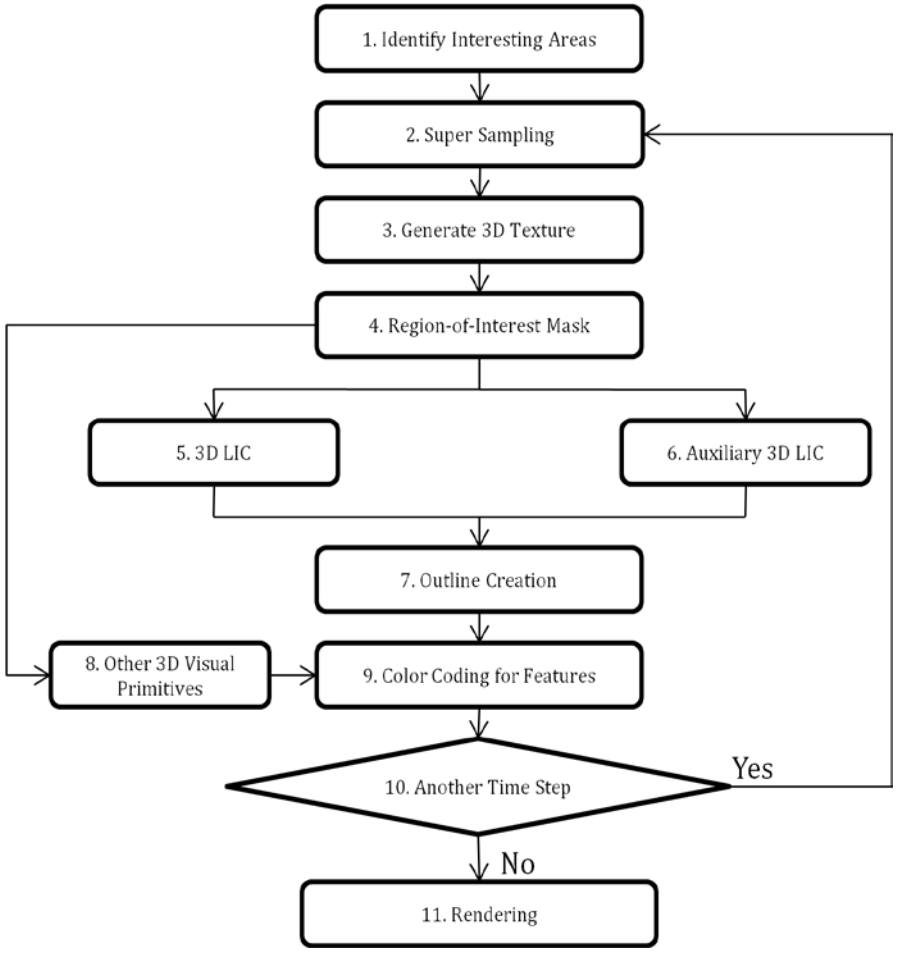

Figure 3.8: This diagram shows the implementation details of the LIC glyph method, which portrays detailed information in the regions of interest in the flow using glyphs and other meaningful visual primitives.

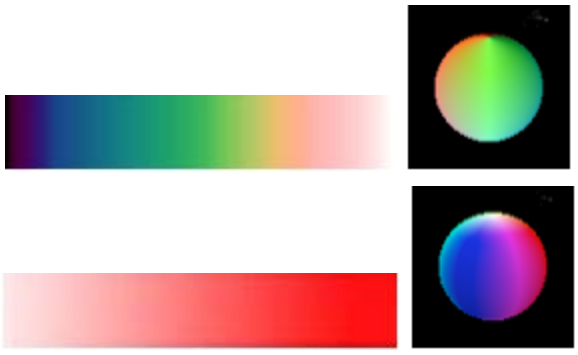

Figure 3.9: The upper left image and lower left image show the rainbow colormap and color saturation respectively. The upper right image and lower right image show color wheels of the RGB color model and HSV color model respectively.

3.4.2.2 Experimental Results

The LIC glyph algorithm is applied to our two datasets, 3D turbulent flow and time-evolving vortex ring data. The strength of the LIC glyph algorithm is that these glyphs are capable of conveying multiple dimensions through the visual variables of size, shape, color, and orientation. They could also provide dense and random visualization at all locations in interesting regions without the issue of full occlusion.

3.4.2.2.1 LIC Glyph Method for Vorticity Direction

We apply the LIC glyph method to the vorticity field within a subspace containing an interesting vortex region. Spherically-shaped particles in the 3D texture are warped with respect to the vorticity when 3D LIC is performed on those particles, so the shape of glyphs indicates vorticity directions. Moreover, transition of colors painted on the surfaces of glyphs is achieved by referencing the different skewed values, produced in step 6 of the algorithm in figure 3.8, at the locations on glyph surfaces. Color coding by using rainbow color scale on those glyphs could make the vorticity direction salient. Figure 3.10 shows using the LIC glyph method to indicate vorticity direction within a vortex region composed of two elongated tubes touching each other near one end of both tubes. The thin boundary outlines represent the vortex region we are interested in, and the opaque inner LIC glyphs convey the information inside the vortex region. The thin boundary outlines are composed of iso-surfaces which are completely transparent when they are facing the viewing direction. This transparent technique is very useful

because it helps researchers view everything inside the vortex region directly and can still have a sense about the boundary of the region. The LIC glyphs using rainbow color scale provide the leading direction of the glyphs with respect to vorticity direction clearly. The white leading end and the clear variation of colors on the glyphs disambiguate the direction of the vorticity field effectively. This LIC glyph method by using rainbow color scale could effectively show the behavior inside this clump and provide the hint of the vortical structure with these two touching individual vortices.

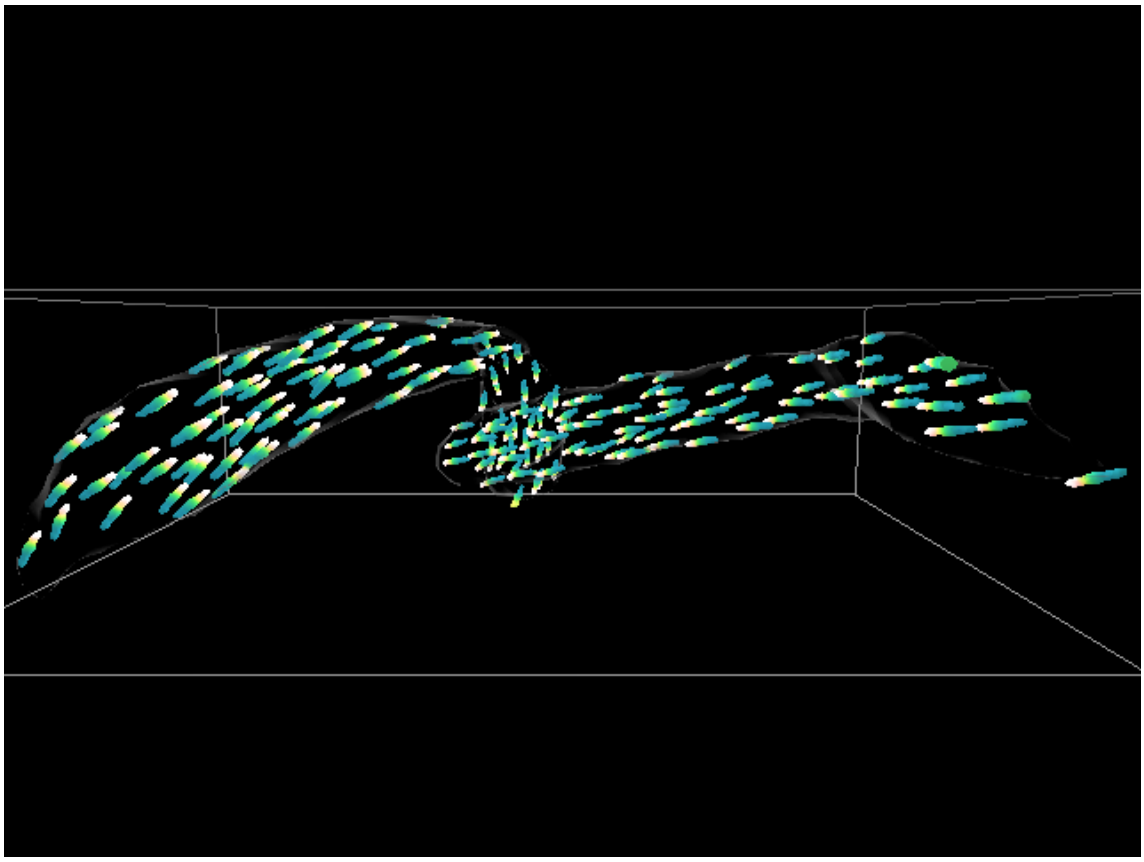

Figure 3.10: Using the LIC glyph method to indicate vorticity direction within a vortex region. Glyphs with color transitions encompassed by thin gray outlines convey vorticity direction effectively.

We also apply our LIC glyph method to a time-dependent vortex ring dataset which includes 70 time steps. Figure 3.11 demonstrates the flows within a higher swirl strength region clearly and delivers vorticity direction by the variation of colors on the LIC glyphs implying the flow rotation of the ring. This image also shows the flow rotation of the left vertical structure is clockwise while the right one rotates counter clockwise.

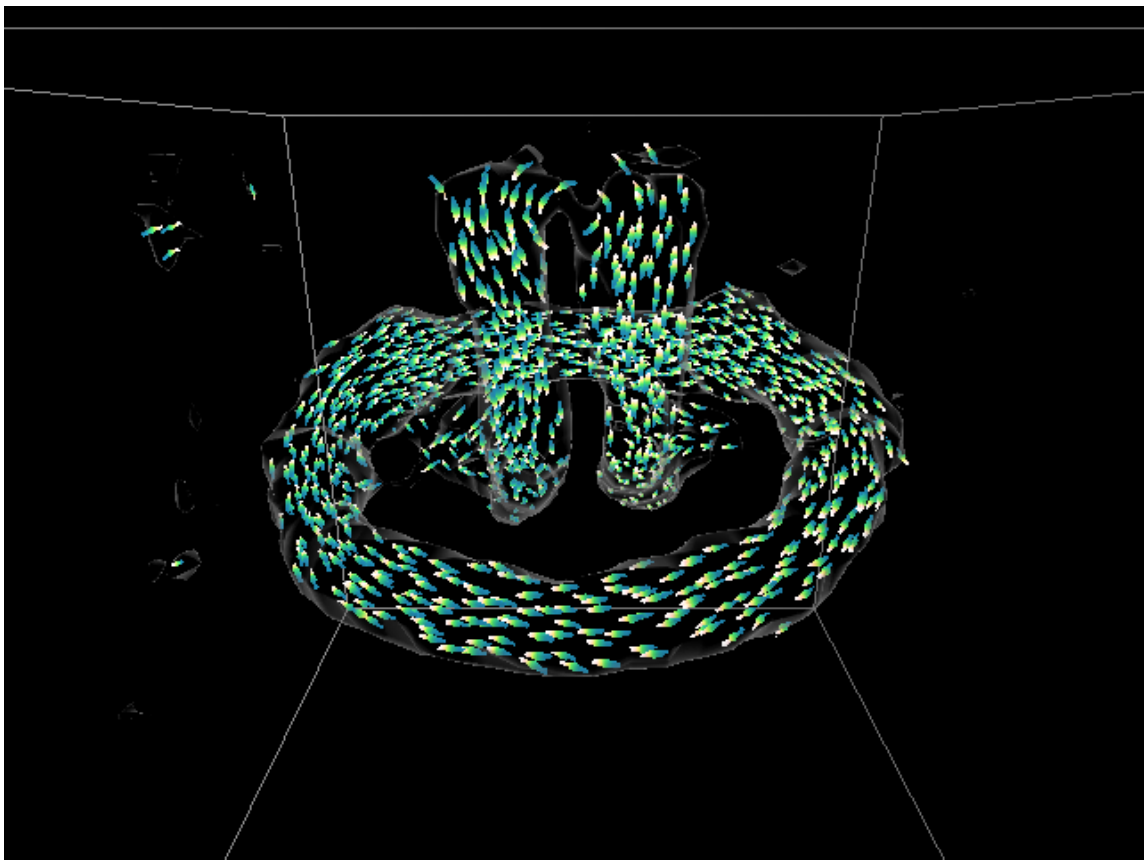

Figure 3.11: Using the LIC glyph method to visualize vorticity directions withing a vortex ring. This figure shows regular LIC glyphs representing vorticity direction using the rainbow color model.

3.4.2.2.2 LIC Glyph Method for Vorticity Orientation

In the previous section, we have observed the vorticity direction according to the white leading part and color variation of the glyphs. However, we would like to develop a color coding method, which could convey the orientation, not just rough direction of vorticity. The color coding method for this idea is performed in the way that the color at each vertex on the surface of glyphs is assigned by looking up colors on a given sphere from the origin along the vorticity vector at that vertex. The colors on the sphere are not restricted to any design as long as colors at any two points on this sphere are distinct. We proposed two sphere color models for our experiments. Our first model, regular color model, varies blue color channel according to the vertical axis and red and green color channels according to horizontal axis. Our second model looks up the HSV color model to assign each color on the sphere.

Figure 3.12 shows a complex vortex, composed of several elongated vortex tubes, with numerous glyphs inside depicting the information of the vorticity orientation at each point on the surface of glyphs. This figure clearly demonstrates color differences from one end of the vortex to the other end, and the sphere of our regular color model shown in the left-bottom corner provides the assistance for the mapping of colors and vorticity orientations. We may observe from the difference of colors that colors around the joint part of those elongated vortex tubes vary greatly, providing an important research hint for us to further analyze its insight.

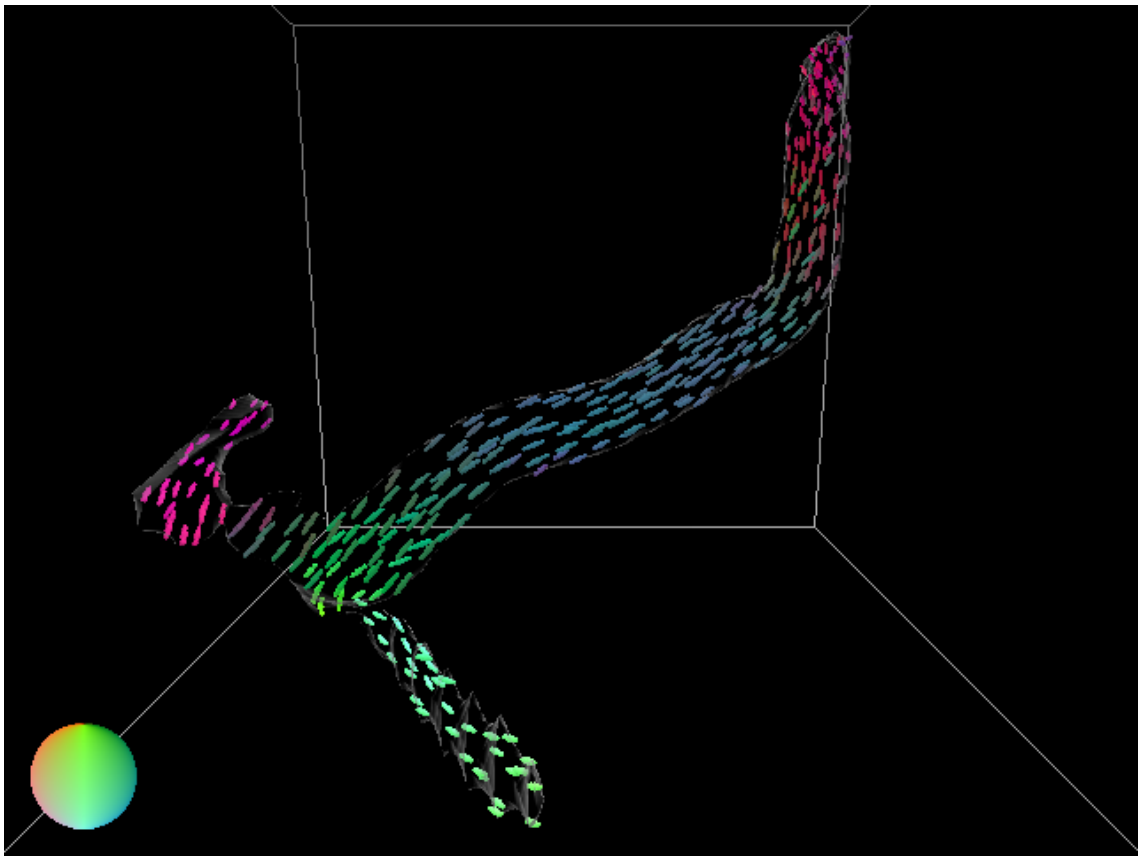

Figure 3.12: Using the LIC glyph method to show the orientation of the vorticity vectors within a complex. Different vorticity orientations are represented using different colors.

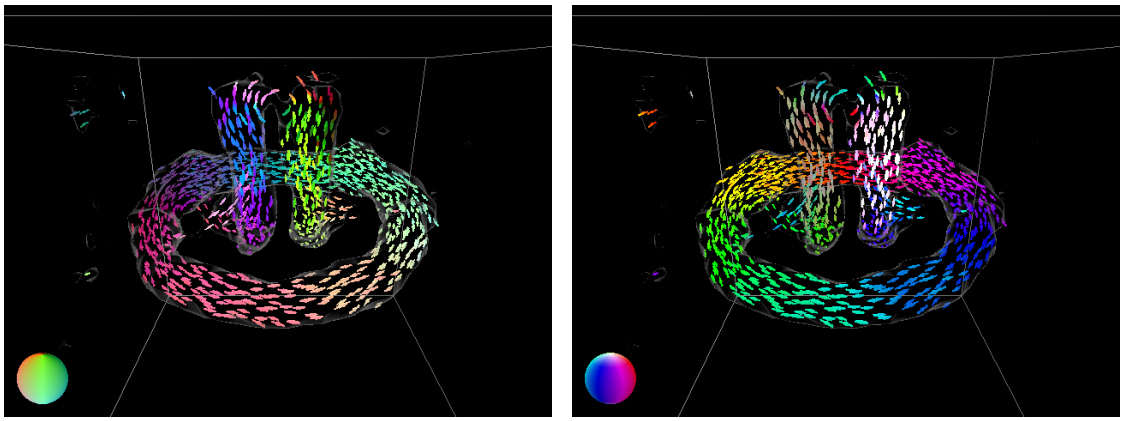

Figure 3.13: Using the LIC glyph method to convey information about the orientation of the vorticity vectors within a vortex ring using our regular color model (left) and HSV color model (right).

We also apply the LIC glyph algorithm to the vortex ring dataset. Two images in figure 3.13 show the clear color variation throughout the vortex according to vorticity orientation by using two different models. In the left image, different colors of LIC glyphs depict variation of the vorticity orientation at the glyphs' locations. We noticed that the colors in the top region of the left vertical structure are similar to the colors in the front of the ring, and the vorticity directions are supposed to be distinct, toward down and left. In addition, there exist two singular points on the sphere, at the top and bottom. Another color coding based on an HSV color model is applied and demonstrated in the left bottom figure where no singularity exists on the sphere. We designed the value channel of the colors on the sphere to be above 0.5 in order to maintain higher variation among different locations on the sphere, and the result shows its effectiveness.

3.4.2.2.3 LIC Glyph Method for Vorticity Orientation and Direction

We have developed ways to visualize vortex direction and orientation within a target vortex region. However, developing a proper method for viewing different features simultaneously is very useful. In this section, we combine two previous color coding strategies in order to visualize vorticity orientation and direction at the same time in one image. This task can be achieved by first assigning a main color for the glyph according the regular color model to represent vorticity orientation and, then, varying

this color toward white according to vorticity direction. Figure 3.14 demonstrates hints of vorticity direction and orientation on each glyph according to a combination of colors and their variations in which the main color depicts the vorticity orientation, and the white leading part of the glyphs represents the vorticity direction. This method could deliver vorticity information more clearly and effectively than just single encoded information.

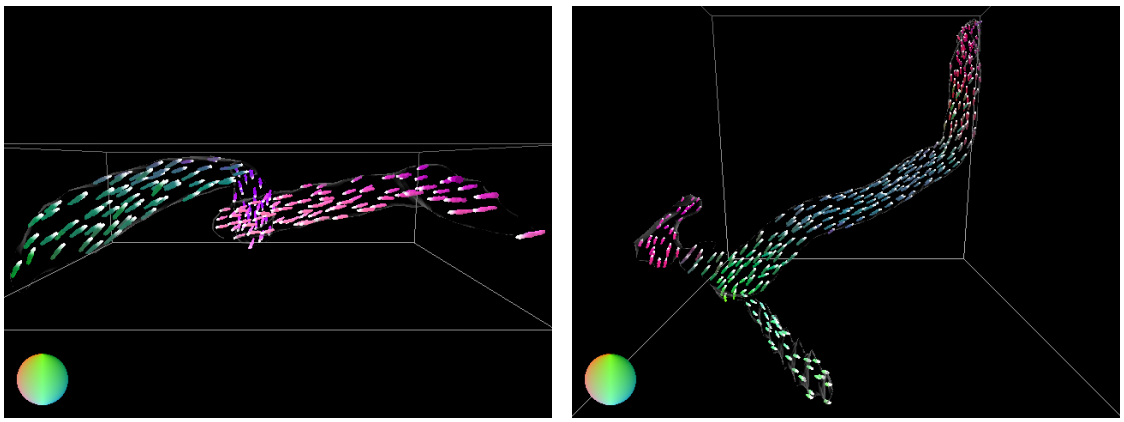

Figure 3.14: A combination of two different color coding methods for visualizing vorticity direction and orientation within a target region in a 3D turbulent flow.

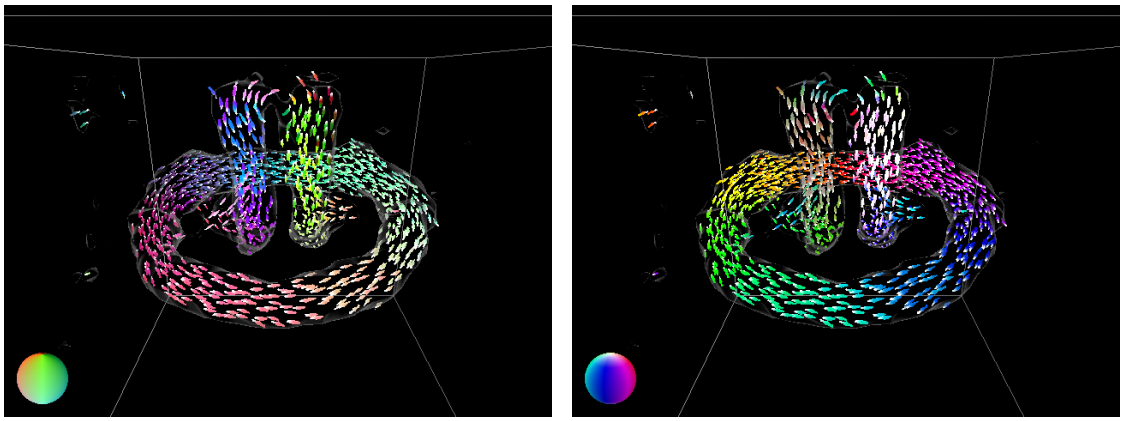

Figure 3.15: A combination of two different color coding methods for visualizing vorticity direction and orientation for a time-evolving vortex ring dataset. In the left image, regular LIC glyphs are used to portray vorticity direction and orientation using our regular color model. The image on the right shows the same information using the HSV color model.

Figure 3.15 shows that this method has been applied to the vortex ring dataset by using our regular color model and HSV color model and has clearly demonstrated the structure inside the ring as well as the two vertical tubes. The effectiveness of this color coding method is that not only the shape of the glyphs could convey the vorticity information but also the combination of multiple color coding methods provides corresponding hints.

3.4.2.2.4 LIC Glyph Method for Vorticity Magnitude

In this section, we investigate methods for visualizing strength of flow quantity and encoding multiple scalars and vector information into colors and shape of glyphs. Our method conveys flow quantities within interesting areas by painting colors according to the strength of quantities. The vorticity magnitude within the target vortex region is interesting to us, so two intuitive color coding methods are developed for this purpose. Our first method is to assign a fully saturated color in the highest vorticity magnitude and gradually decrease its saturation according to the decrease of vorticity magnitude. The fully saturated color is applied to the extreme value of flow quantity, vorticity magnitude, within the current sub-volume in order to be capable of utilizing saturation variations of that color for target flow quantity. The left image in figure 3.16 demonstrates that the vorticity magnitude is higher in the center of the big chunk of the vortex and near the bottom of the upper elongated vortex tube. Our second method visualizes vorticity magnitude by varying transparency of glyph surfaces instead of saturation of colors. Therefore, we can apply this method on top of previous methods to

encode one more dimension of information and deliver a variety of useful information in one image. The right image in figure 3.16 shows that the vorticity magnitude, direction, and orientation within a higher swirl strength region are visualized clearly in one image at the same time by applying the LIC glyph method with our regular color coding and transparency-varying method for the vortex ring dataset. The transparency makes some LIC glyphs faded out so that those prominent glyphs clearly represent the area with high vorticity magnitude.

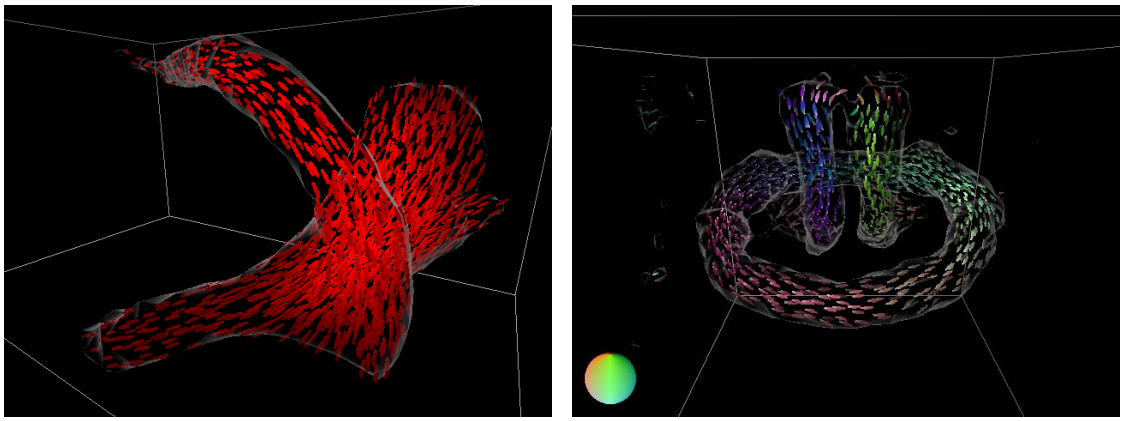

Figure 3.16: Using LIC glyph method to portray vorticity magnitude. Left: Vorticity magnitude within a target region in a 3D turbulent flow is depicted by the variation of color saturation. Right: Vorticity magnitude in the vortex ring data is depicted using transparency.

3.4.2.2.5 LIC Glyph Method for Velocity Fields

Velocities in 3D vector fields serve as the most basic flow data on which many important quantities and features in fluid dynamics rely. In this section, the LIC glyph method with a simple color coding algorithm is applied to visualizing the velocity fields by gradually varying a single color on all the glyphs toward white representing the

leading part of the glyphs with respect to velocities. This similar but simpler method is designed in order to be applied with other color coded glyphs to make the multi-variate visualization clear. The velocity within the interesting vortex region may vary dramatically. If different colors are applied to depict different velocity orientation, the colors presented on the glyphs may turn to be very chaotic and the information can not be conveyed effectively. Therefore, simply transitioning a single color, red, in the glyph body toward the white in the leading part is developed to convey the information of velocity directions shown in figure 3.17. The velocity orientation is still encoded in the shape of glyphs. This figure also demonstrates that the glyphs are circling around the vortex tubes, which is the phenomenon of swirling motion within the vortex.

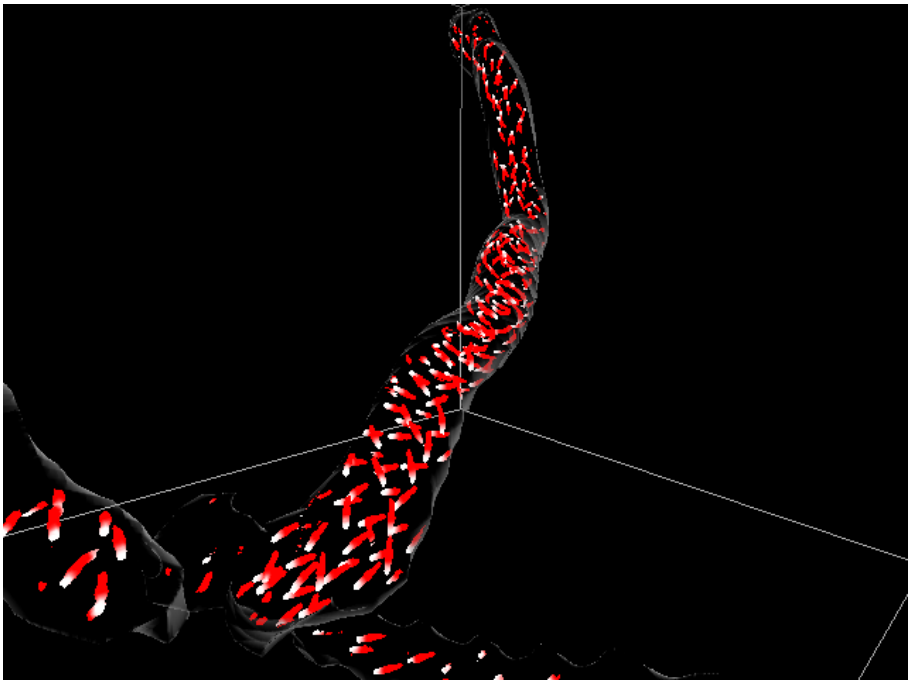

Figure 3.17: Using the LIC glyph method to show velocity information within an interesting target region. A simple color coding method is applied by varying the red color toward white to depict velocity direction, with velocity orientation still delivered by the shape of the glyphs.

3.4.2.2.6 LIC Glyph Method for Vorticity and Velocity

In this section, we demonstrate the possibility to visualize two vector fields simultaneously by our LIC glyph method. The technique places two groups of glyphs together rendered for two fluid vectors, vorticity and velocity, with respect to two different color coding methods for each group of glyphs shown in figure 3.18. The purpose of the investigation on the velocity vector in addition to vorticity is an attempt to differentiate closely paralleled vectors of vorticity by another vector such as velocity here. The vorticity in this figure is colored based on the rainbow color scale for researchers to observe vorticity direction according to the transition of colors on the glyphs. The red glyphs with the white leading parts demonstrate the velocity direction within the same vortex regions. Since the types of coloring for these two groups of particles are distinct in which one is using rainbow color scale with various hues of colors, and the other is using the single red hue, the combination of these two groups does not introduce the confusion or conflict between different information delivered on the glyphs and is able to visualize various information simultaneously and effectively. Moreover, this scheme is still capable of conveying the vorticity and velocity orientation according to the shape of each glyph, and the distinct characteristic of color coding for each glyph group makes this combination a successful strategy. With this investigation, we have seen that the velocity couldn't help us differentiate closely paralleled vectors of vorticity. Its lack of Galilean invariant property is the main reason in which this quantity does not provide reliable results and is less useful in this research.

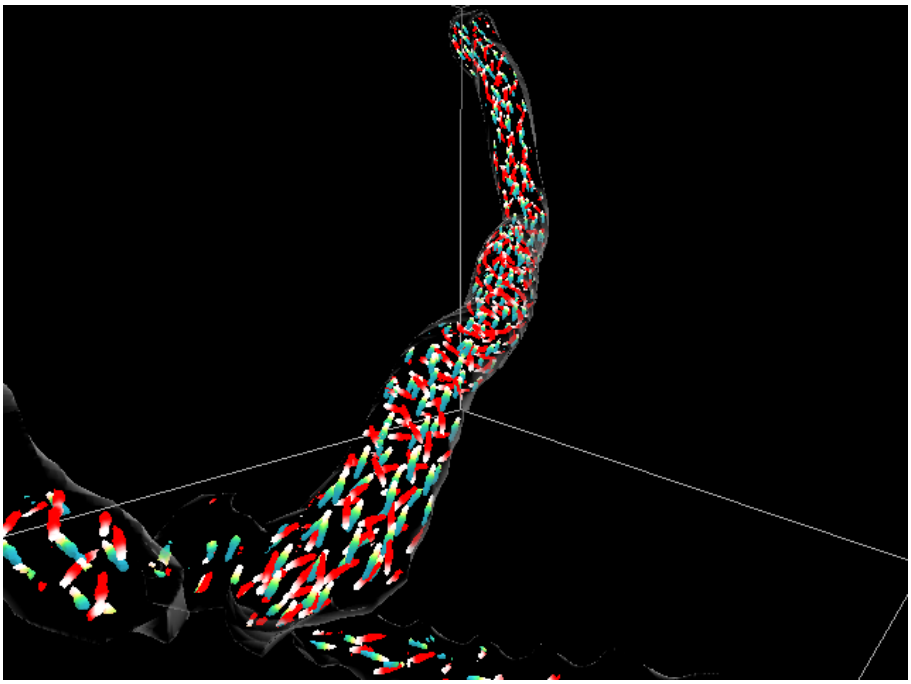

Figure 3.18: Two groups of LIC glyphs convey information about vorticity and velocity simultaneously. The vorticity direction is encoded by color coding using the rainbow color scale, and the velocity direction is encoded by color coding using a single red color varying toward white in the leading part.

3.4.2.2.7 Variation of LIC Glyph Method

Figure 3.19 and figure 3.20 show four images of multi-variate visualization using LIC glyphs. The left image in figure 3.19 represents a structure of a region identified by high swirl strength in which the LIC glyphs are defined by the vorticity vector field. The color coding is defined by a rainbow scale, representing a clear variation of colors on the LIC glyphs, and effectively depicting the leading direction of each glyph. Although this variation of colors on the glyphs helps to show the direction, colors can alternatively be used to show another dimension of information. The right image in

figure 3.19 shows the same LIC glyphs but color coded according to the vorticity orientation. The color coding method used in this figure varies colors with red and green channels when vorticity varies horizontally, and change of vertical orientation varies the blue channel. Colors conveying orientation are looked up on the color wheel according to the vorticity. Since the colors on the sphere do not include white, one more dimension of information can be conveyed by using the white color to represent the leading direction of the vorticity vectors. This visualization shows that there may be multiple different vortex structures in this region. One is the tube that extends from the top to the front, and another one is oriented from left to right. A third segment is visible in the chunk behind. Since the length of each LIC glyph is long, we can encode more variables by varying this dimension. Two images in figure 3.20 show the use of a similar algorithm but adaptive noise sizes and LIC filter lengths according to the velocity magnitude at the location of LIC glyphs. It shows some regions with less velocity magnitude clearly such as the left and right ends of this vortex as well as the top side of the chunk.

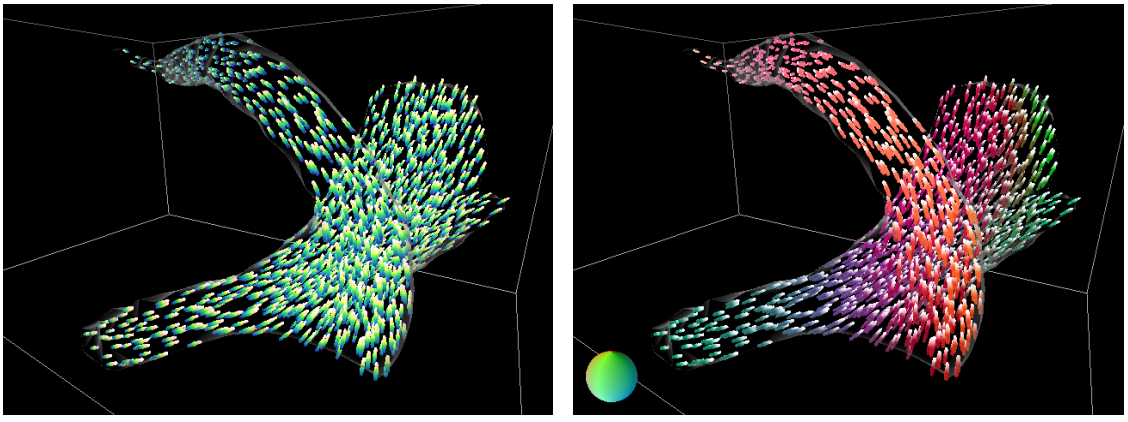

Figure 3.19: The left image shows that regular LIC glyphs are used to portray vorticity direction. The right image shows that regular LIC glyphs encode both vorticity direction and orientation.

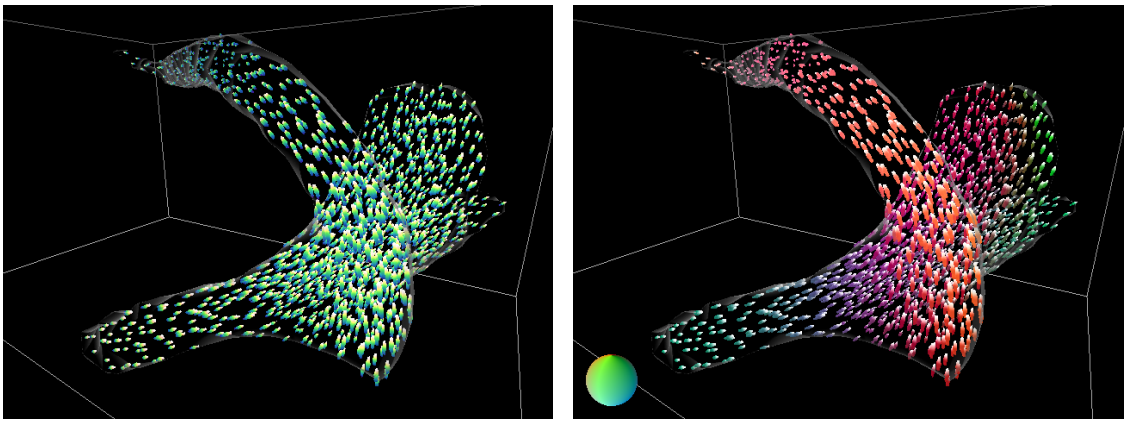

Figure 3.20: LIC glyphs being used to encode a combination of vorticity and velocity information. The glyph direction is defined by the vorticity direction, and the glyph size is defined by the velocity magnitude.

3.4.2.2.8 LIC Glyph Method with 3D Arrows

In figure 3.21, we try to render LIC glyphs and 3D arrows at the same time; however, it doesn't seem to be very effective. The left image in figure 3.21 shows lengthy LIC glyphs, created by LIC filters with different length and noises with different sizes for vorticity direction, as well as 3D arrows at the same time. The right image in figure 3.21 shows a close-up with the arrows colored by using a weighted common target color according to the statistical distribution of the angles formed by the vorticity and swirl vectors at each sample point. The two vectors and their angles we try to deliver by using arrows are obscured by the LIC glyphs, and the space is filled with glyphs and arrows completely, introducing a serious occlusion.

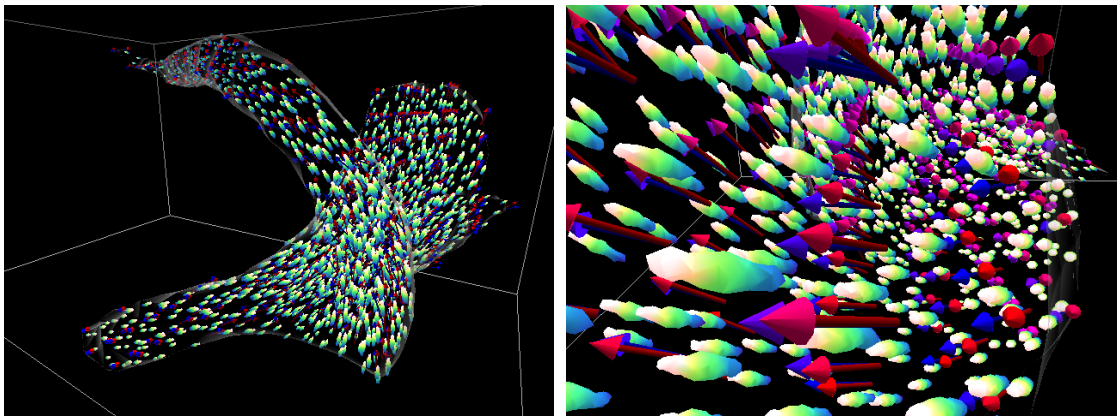

Figure 3.21: Using LIC glyphs and arrows to visualize multiple vector fields. Here, the LIC glyphs are used to portray the vorticity direction while arrows show the swirl vectors.

3.4.2.2.9 LIC Glyph Method for Unsteady Data

We also apply our LIC glyph method to all 70 time steps of the time varying vortex ring dataset with comparisons of two different results. We note that if we just blindly repeat the same algorithm, by randomly generating a new noise texture for the locations of the LIC glyphs for each time step, individual LIC glyphs might appear to be shifting in orientation from frame to frame, which we feared could create an inaccurate impression of motion that was not consistent with the data. In fact it is the animation with the randomly changing glyph locations that introduces unwanted motion artifacts into the animation. But this problem may be reduced if we use a constant initial texture for each iteration. We produced two videos in video 3.1 to decide which one is best for observing these time evolving flows. We also considered advecting the LIC glyphs along the vorticity direction like we would if they were indicating the flow direction. However, this does not deliver correct information for visualization because there is no

inherent motion of the flow in the direction indicated by the vorticity vector field. Our first video shows the animation of the random LIC glyphs, in which generation and production of particles are performed randomly for each time step in the stage of the 3D texture creation. The second video shows the animation of the constant LIC glyphs in which the texture generated in step 3 remains constant throughout all the time steps. In these videos, we are able to observe the evolution of the vortex ring and the two main vertical structures clearly. The mask and outline for the regions of interest in our algorithm provide the focus of visualization without blocking the view of the inner structure. The random location of LIC glyphs in our first video shows a little distraction between successive images. The constant LIC glyphs shown in the second video are applied to eliminate this issue for better coherence between frames in the animation. In fact, the difference between these two videos is hard to perceive, and it is very difficult to judge which one is better.

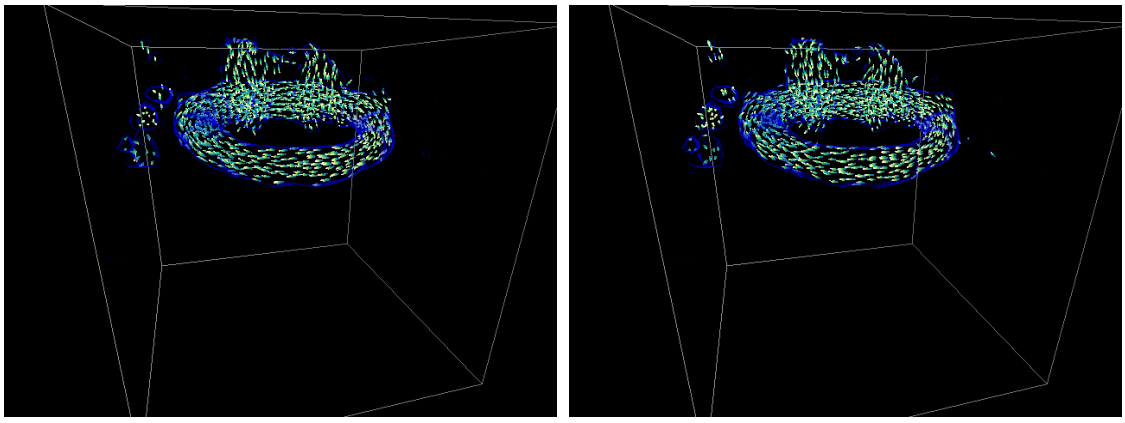

Video 3.1: Left image shows the first video of the random LIC glyphs for the unsteady ring data. Right image shows the second video of the constant LIC glyphs for the unsteady ring data.

3.5 Discussion

One of our challenging parts of the research in visualization of 3D turbulent flow field is the lack of exact physical definition in fluid dynamics such as the vortex and effective visualization tools for the interesting phenomenon in the flow. In this section, we have demonstrated the use of the LIC glyph representation to achieve effective multi-variate visualization in two different 3D flow datasets. Our approach is capable of portraying numerous types of features such as vectors and quantities within interesting target regions. This technique could avoid perception issues such as depth and clump because of the use of uniformly and sparsely distributed noises in the 3D texture as well as traditional rendering method of the iso-surface extraction. We have successfully visualized magnitude, direction, and orientation of vorticity and velocity individually or simultaneously within a region of higher swirl strength by using a variety of color coded glyphs or 3D arrows. The thin outline surface representing the interesting target vortex region and encompassing warped LIC glyphs is a very effective technique for the visualization of an interest region. Our results demonstrate strengths and weaknesses in the use of various different mappings between data features and visual variables. Our algorithm applied to time-varying data shows the effects of portraying a number of different variables at the same time regarding maintaining the coherence of the flow evolution.

The contribution of our LIC glyph method in this chapter provides insight into promising approaches in the design and use of glyphs for the purpose of development of

more effective vortex segmentation methods. Some observations of phenomena in our 3D turbulent flow data are as follows. Firstly, vorticity direction indicates the information about rotation of the vortices. Secondly, there is high correlation between vorticity orientation and topology of a vortex region. Thirdly, our investigation shows that vorticity follows the topology of vortex tubes and still keep their orientation with respect to corresponding tubes around the joint region. This phenomenon leads to significant orientation difference among each vortex tubes near the joint region. These observations are very helpful for us to perform advanced analysis on vortices. Video results of our vortex ring data also provide invaluable research contributions for the future.

Chapter 4

Segmentation Using Multiple Scalar and Vector Quantities

This chapter proposes a novel idea of distinguishing individual structures of the vortex. Different measures of rotation direction are studied individually and derived with their underlying theoretical relationships. We notice that the orientations of some characteristic vectors seem to have certain correlation among neighboring grid locations and may imply structure information in it. Thus, we investigate angle difference for some vectors and partition the grid cells inside the vortex region. A region-growing algorithm is proposed to segment connected clumps into individual vortices, and thresholds are assigned as the tolerance of each vector.

4.1 Approach Ideas

In turbulent channel flows, the vortices that occur near the boundary often appear in densely intertwined, tightly packed clumps as the flow in figure 4.1 was obtained from a three dimensional, high Reynolds number (934), direct numerical simulation of a turbulent channel flow [1]. The red vortex in figure 4.1 is a complex vortex obscured by other gray vortices, and, thus, it represents the difficulty of presenting the details of flow properties within the neighboring volume of the red vortex. In this data, we have found that methods that identify regions of swirling flows according to any single globally-defined threshold level of a scalar quantity such as swirl strength inevitably fail to differentiate individual structures in regions of the flow that are close to the wall, which is the bottom plane of the channel, while at the same time failing to capture individual structures in regions of the flow that are far above the wall.

In our first efforts to robustly identify individual vortex structures in turbulent flow, we sought to investigate the extent to which it might be possible to achieve a superior segmentation of a flow dataset by using multiple scalar and/or vector flow features in combination rather than relying on a single scalar feature alone. The first step in this process is to identify promising complementary flow features indicative of the presence of a vortex.

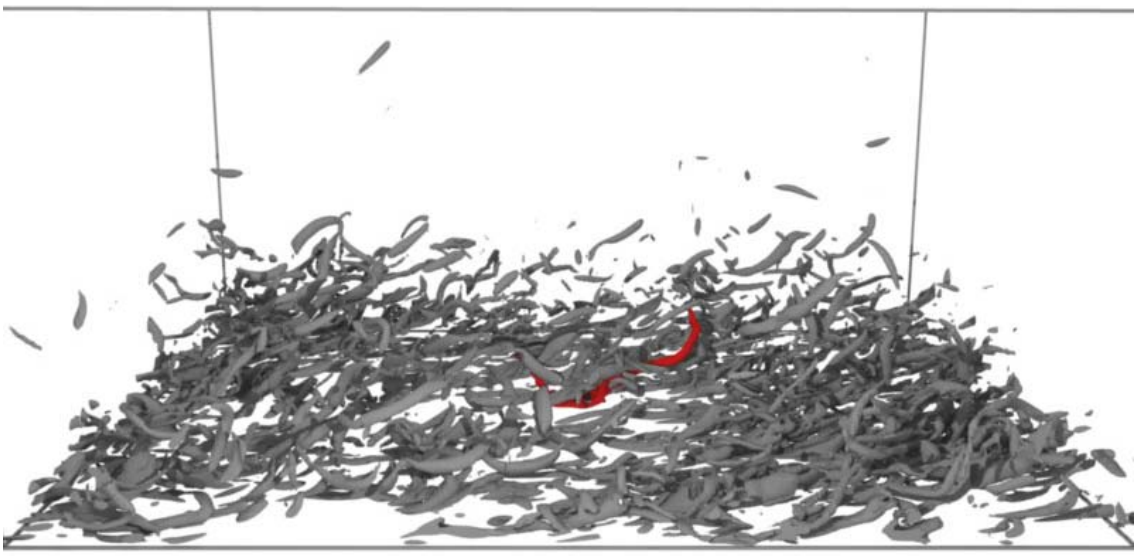

Figure 4.1: Vortices defined by a threshold level of swirl strength. The region marked in red represents a compound structure defined by a connected set of neighboring voxels all with supra-threshold values.

We begin by observing that although Q, Δ, and λ_2 represent different scalar measures, the regions identified by isosurfaces of each of these quantities are typically very similar, especially at high Reynolds numbers [100]. Hence we investigate the potential of using vector valued features to differentiate neighboring structures. Three vectors relating to fluid rotation are investigated. First one, $\bar{c}$, is vorticity which could be used to measure the rotation in the flow. Second vector, $\bar{r}$, is the real eigenvector of velocity gradient tensor. The direction of this vector could determine the orientation of vortex core and provide information about vortical structure. Third vector, $\bar{n}$, is normal vector of a characteristic plane that is composed of $\bar{t}$ and $\bar{s}$ where $\bar{s} \pm \bar{t}i$ are complex eigenvectors of velocity gradient tensor. The exact behaviors of these three characteristic vectors are quite vague. However, they tend to align in some parts but distinct in some other parts within the vortex region identified by swirl strength. Angle

difference for these three vectors provides the indication of partitioning the grid cells within the interested vortex clump, and a region-growing algorithm is performed for segmentation of complex vortices. Not all of vectors are applied at the same time and different combination of vectors provides different segmentation results.

4.2 Quantities of Vorticity and Swirl

In the velocity vector field

$$\bar{V}(x,y,z) = \langle P(x,y,z), Q(x,y,z), R(x,y,z) \rangle,$$

there are two distinct kinds of rotation defined by the vorticity vector and the swirl vector. The vorticity of a velocity vector field *V*, also called the *curl* of *V*, is defined as

$$\bar{c} = \nabla \times V = \langle R_y - Q_z, P_z - R_x, Q_x - P_y \rangle.$$

The direction of this vector $\bar{c}$ determines the local axis around which rotation occurs as well as the sense of the rotation (using a right-hand rule). The *swirl* of a velocity vector field is defined when two of the eigenvalues of ∇V are complex. This measure is designed to differentiate swirling motion about an axis from rotation due to a simple shear. In this case, there is a rotation in the plane determined by the two complex eigenvectors.

Swirl and the swirl vector $\bar{v}_s$ are defined as follows. First we compute the eigenvalues and eigenvectors of the Jacobian of *V*

$$A = \nabla V = \begin{pmatrix} P_x & P_y & P_z \\ Q_x & Q_y & Q_z \\ R_x & R_y & R_z \end{pmatrix}.$$

Suppose the matrix A has one real eigenvalue λ with real eigenvector $\bar{r}$ and a pair of complex conjugate eigenvalues $\lambda_1 = a + bi$ and $\lambda_2 = a - bi$ with $b > 0$, with associated complex eigenvectors $\bar{v}_1 = \bar{s} + \bar{t}i$ and $\bar{v}_2 = \bar{s} - \bar{t}i$. We can assume the eigenvectors are of unit length so $1 = |\bar{v}_1|^2 = |\bar{v}_2|^2 = |\bar{s}|^2 + |\bar{t}|^2$. Then swirl is defined as $s = b$. Complex eigenvalues indicate a rotation in a plane. We claim that this plane is spanned by the real vectors $\bar{s}$ and $\bar{t}$. To see this, we first note that

$$A\bar{s} = \frac{A\bar{v}_1 + \bar{v}_2}{2} = \frac{(a+bi)(\bar{s}+\bar{t}i)+(a-bi)(\bar{s}-\bar{t}i)}{2} = a\bar{s} - b\bar{t}. \qquad (15)$$

Similarly, we can show

$$A\bar{t} = b\bar{s} + a\bar{t}. \qquad (16)$$

Equations (15) and (16) together imply that the matrix of the linear transformation A restricted to the plane spanned by $\bar{s}$ and $\bar{t}$ looks like

$$A = \begin{pmatrix} a & -b \\ b & a \end{pmatrix}$$

with respect to the basis $\bar{s}$ and $\bar{t}$. If we now let $d = \sqrt{a^2 + b^2}$ and define θ by $\cos\theta = a/d$ and $\sin\theta = b/d$ we can rewrite A as

$$A = \begin{pmatrix} d & 0 \\ 0 & d \end{pmatrix} \begin{pmatrix} \cos\theta & -\sin\theta \\ \sin\theta & \cos\theta \end{pmatrix}.$$

That is, in the plane spanned by $\bar{s}$ and $\bar{t}$, A is performing a rotation by θ followed by scaling by d. This describes a spiraling motion. The right-hand normal to this plane is

$\bar{n} = \bar{t} \times \bar{s}$. There are two different ways to think of the axis of this rotation. On the one hand, it is common to think of the normal, $\bar{n}$, to this plane as the axis of rotation so we could define the swirl vector as $\bar{v}_s = \bar{n}$. On the other hand, the real eigenvector, $\bar{r}$, better defines the direction the swirling plane is moving as shown in figure 4.2 and [3], so we could also define the swirl vector as $\bar{v}_s = \bar{r}$ (If $\bar{r} \circ \bar{n} < 0$, we replace $\bar{r}$ by $-\bar{r}$). We explore using $\bar{c}$, $\bar{r}$, and $\bar{n}$ to segment the vortices.

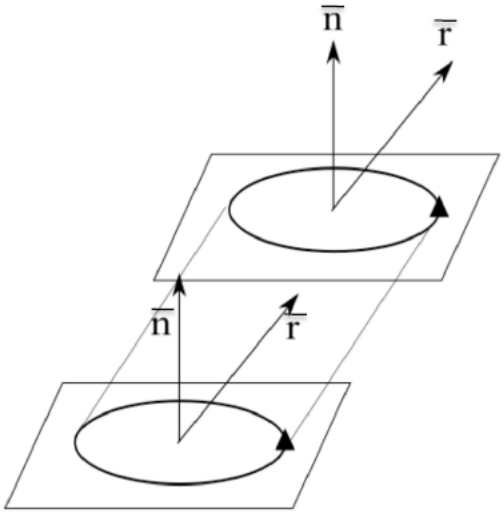

Figure 4.2: Swirl rotation axes represented by the plane normal $\bar{n}$ and swirl vector $\bar{r}$.

4.3 The Relationships between Vorticity and Swirl

Although $\bar{c}$, $\bar{n}$, and $\bar{r}$ all tell us something about rotation direction in 3-space, in general they each point in a different direction. In order to better understand how vortices change over time and to help us devise disentanglement algorithms, we need to know

how these vectors are related mathematically. The following facts can be established (proofs are provided in the appendix).

Let $\lambda_1 = a + bi$ and $\lambda_2 = a - bi$ with $b > 0$ being the complex eigenvalues and $\bar{v}_1 = \bar{s} + \bar{t}i$ and $\bar{v}_2 = \bar{s} - \bar{t}i$ with $|\bar{s}|^2 + |\bar{t}|^2 = 1$ being the associated eigenvectors of the Jacobian ∇V of a velocity vector field V. Let λ be the real eigenvalue with associated real eigenvector $\bar{r}$.

Theorem 1. $\bar{c} \cdot \bar{n} = b$, so that the angle θ between $\bar{c}$ and $\bar{n}$ is given by:

$\cos\theta = \frac{b}{|\bar{c}||\bar{n}|}$.

An immediate corrolary to Theorem 1 is:

Corollary 1. The swirl b is always less than half of the magnitude of the vorticity.

Hence regions with high swirl must also have high vorticity.

Theorem 2. Let

$$B = \begin{pmatrix} \bar{s} \\ \bar{t} \\ \bar{r} \end{pmatrix}, \qquad \bar{w} = \begin{pmatrix} (a-\lambda)\bar{s}^T\bar{r} - b\bar{t}^T\bar{r} \\ b\bar{s}^T\bar{t} + (a-\lambda)\bar{t}^T\bar{r} \\ 0 \end{pmatrix}$$

Then

$$\bar{r} \times \bar{c} = B^{-1}\bar{w},$$

So that the angle α between $\bar{c}$ and $\bar{r}$ is given by

$$\mathrm{Sin}\,\alpha = \frac{|B^{-1}\bar{w}|}{|\bar{r}\,||\bar{c}\,|}\,.$$

Theorem 3. If any two of $\bar{c}$, $\bar{n}$, and $\bar{r}$ are in the same direction, so is the third.

These theorems suggest that we may be able to gain insight into how turbulence evolves over time by exploring how the various rotation directions change relative to each other.

4.4 Segmenting Compound Structures Using Vorticity and Swirl

Figure 4.3 shows that turbulent structures have been segmented solely on the basis of scalar values of swirl strength. The segmentation is defined as follows. We begin by choosing an aribtrary point whose swirl strength is above the threshold level. We then define the structure to which that point belongs by implementing a recursive flood fill algorithm, adding a neighboring point to the structure if and only if its swirl strength is also above the threshold level. When we find that no additional points can be added to a structure, we repeate the process by choosing a new seed point and continue until all points in the volume whose swirl values are above the threshold have been tagged as

belonging to one structure or another. The structures in each image are each displayed in a different color to clearly label the segmentation.

Figure 4.4 shows that structures have been segmented both on the basis of swirl strength and on the basis of angles between the directions of $\bar{c}$, $\bar{n}$, and $\bar{r}$ at neighboring voxels. Specifically, the same flood fill approach is used to define a connected region, but in this case a region is expanded to include a neighboring voxel only when the swirl and vorticity directions at that voxel are within a threshold degree of consistency with the swirl and vorticity directions at its neighboring points, in a discretiztion of the domain, that have already been identified as belonging to the region. It can be clearly seen that, regardless of the particular threshold values chosen, superior segmentation results are achieved using this combination of scalar and vector flow features than are achieved using swirl strength alone, providing an assist of identifying individual vortex segmentations with distinct surface colors. It can also be seen, by inspection, that introducing the directional consistency criteria does not result in the spurious subdivision of coherent structures into fragments, even in cases where the vortices are quite bent in their overall shape.

This suggests that there is inherently more promise in an approach that uses both swirl strength and the consistency of swirl and vorticity directions between neighboring points to identify individual vortex structures than there is in an approach that considers only the level of swirl relative to a threshold. The problem of automatically defining appropriate thresholds of both the scalar quantities and vector differences to use in this process is a separate question, which we intend to address in future work.

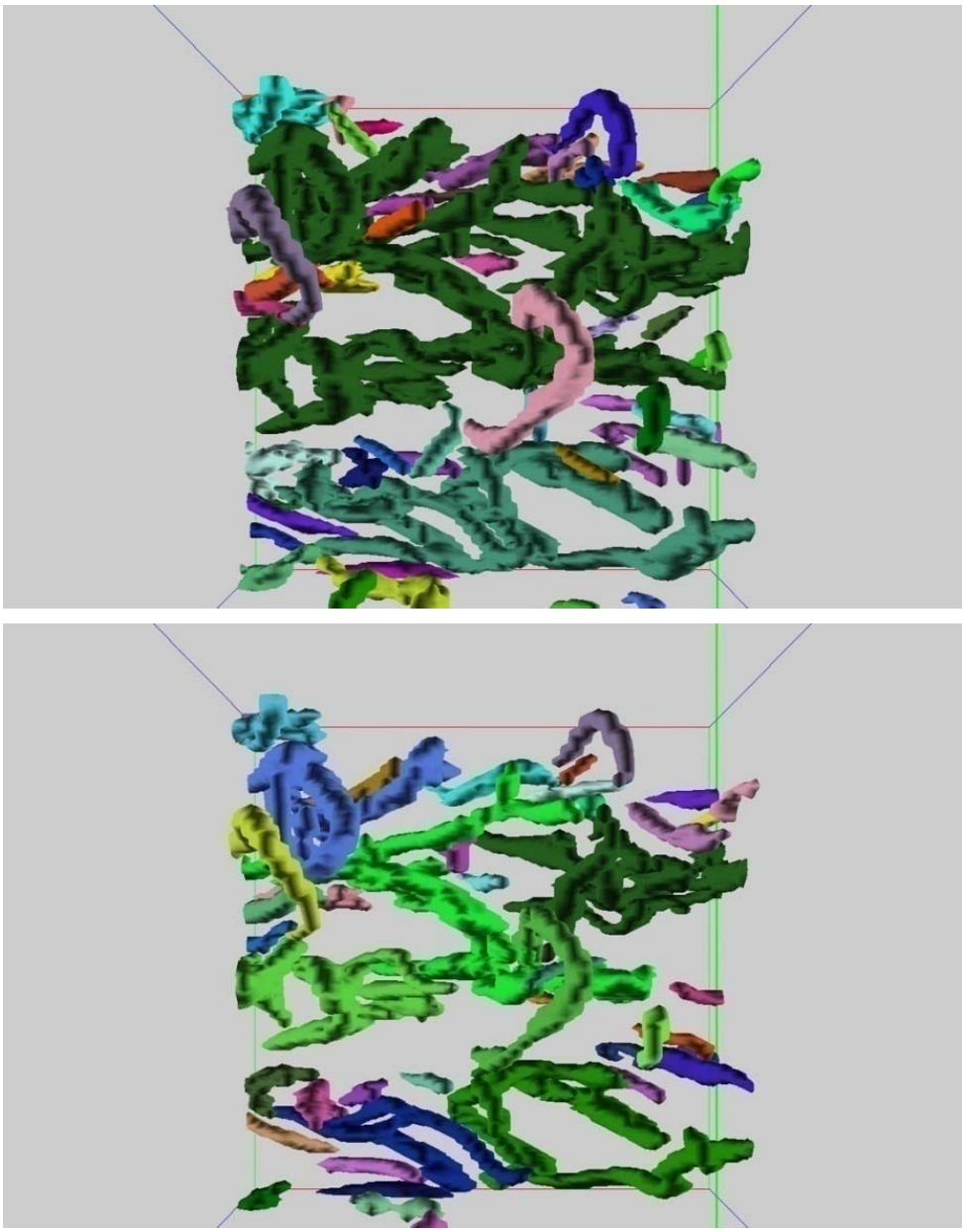

Figure 4.3: Individual vortices segmented according to a threshold level of swirl strength (only), for two different thresholds.

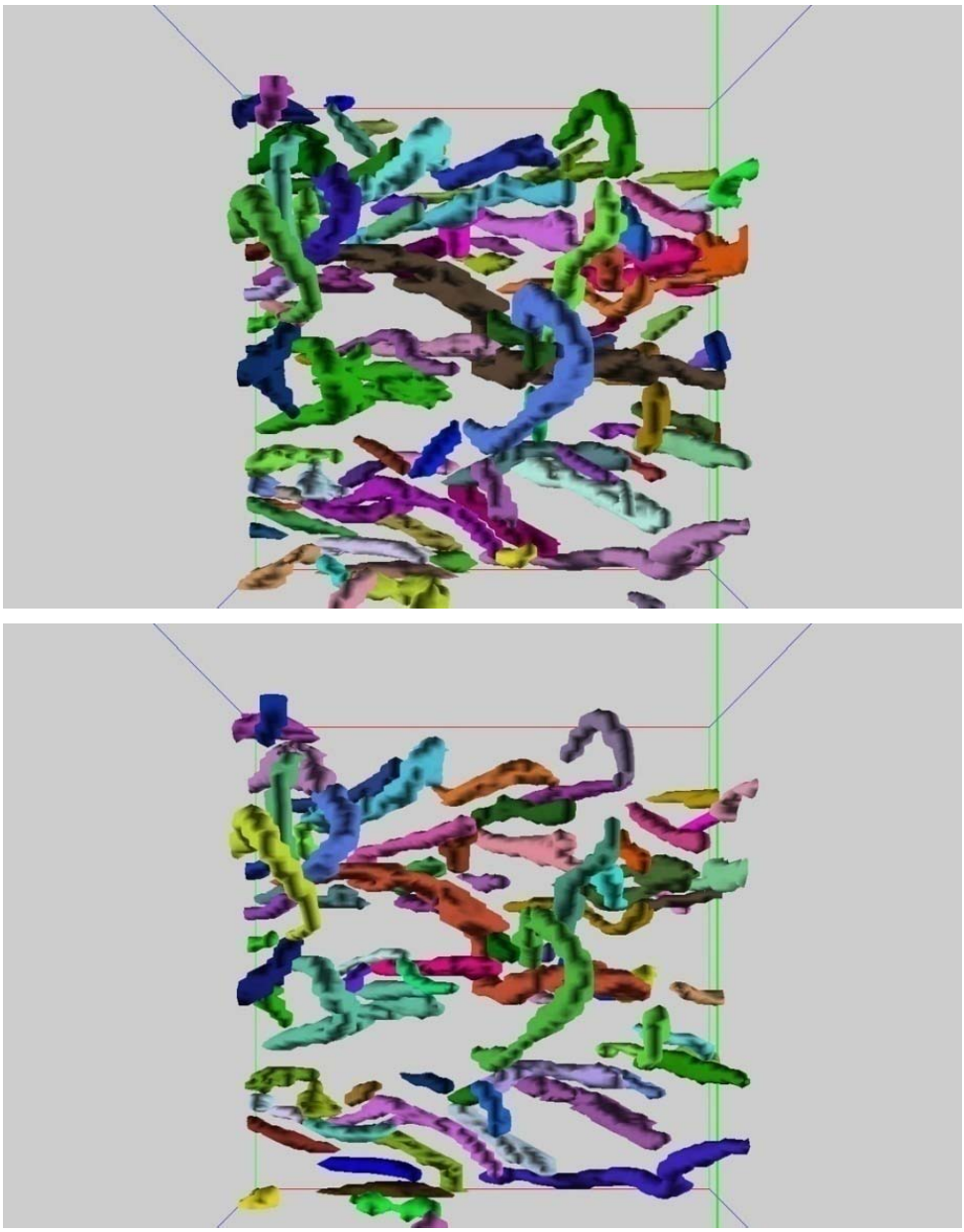

Figure 4.4: Individual vortices defined by similar threshold levels of swirl strength, and by threshold differences between the swirl and vorticity directions at neighboring points.

4.5 Experimental Results

This method performs segmentation of a vortex by examining angles of adjacent rotation vectors with respect to a pre-defined angle tolerance. It is very simple and efficient as the examination is performed at each grid. We have demonstrated the close relations of three vectors, $\bar{c}$, $\bar{n}$, and $\bar{r}$, and applied these vectors to this method. Figure 4.5, figure 4.6, and figure 4.7 show that three interesting distinct clumps of vortices are identified at the level of swirl strength 5.0. Those regions are bounded by transparent layers with one or more distinct colors. The upper image in figure 4.5 shows that two individual vortices are found and given with blue and red colors when using vorticity, $\bar{c}$, with the angle tolerance, 17 degrees. Each 3D arrow is composed of a red or blue cylinder body and a white cone head. The orientation of the 3D arrow represents where a vorticity vector points at. Red and blue colors of cylinder bodies represent vectors' locations within different segments. Only vorticity, $\bar{c}$, is used and is visualized by the white color of the cone head. In the lower image of figure 4.5, normal vector, $\bar{n}$, is utilized with the same angle tolerance, 17 degrees, instead and capable of identifying more individual vortex segments, represented by cyan, blue, and red arrow bodies and transparent surfaces. The color of cone heads is blue, representing that the normal vector, $\bar{n}$, is used.

Figure 4.6, and figure 4.7 demonstrate the use of vorticity, $\bar{c}$, and swirl vector, $\bar{r}$. The upper image in figure 4.6 shows that the swirl vector is used to segment individual vortices as blue and red transparent surfaces and arrow bodies by the angle tolerance, 25

degrees. The green cone head represents the use of swirl vector. In the lower image of figure 4.6, vorticity is denoted by arrows with white cone head and could provide better segmentation compared with the upper image. Three segments are represented with cyan, blue, and red colors on the surfaces and arrow bodies. The upper image in figure 4.7 shows that no individual vortex is found within the identified interesting clump. Only a single vortex is found, so the color for this entire segment is red. The white color of the cone head represents vorticity, $\bar{c}$. The lower image in figure 4.7 shows that the segmentation can be achieved by examining both vorticity, $\bar{c}$, and swirl vector, $\bar{r}$. The red and cyan colors of the transparent layers and arrows' cylinder bodies represent different individual segments of this interesting vortex. At each grid position, two arrows appear with different colors in their cone heads, white and green. Arrows with white cone heads represent vorticity vectors while arrows with green cone heads are for swirl vectors. This method successfully segments the individual vortices one of which is a long tube touching the main portion of a vortex in one end by using both tolerances of vorticity and swirl vectors at 20 degrees.

Although this new method is capable of segmenting individual vortices, the success of this algorithm relies on the angle tolerance and rotation vectors chosen as well as the isosurface value. Advanced investigation for selection of these factors is an important future research topic.

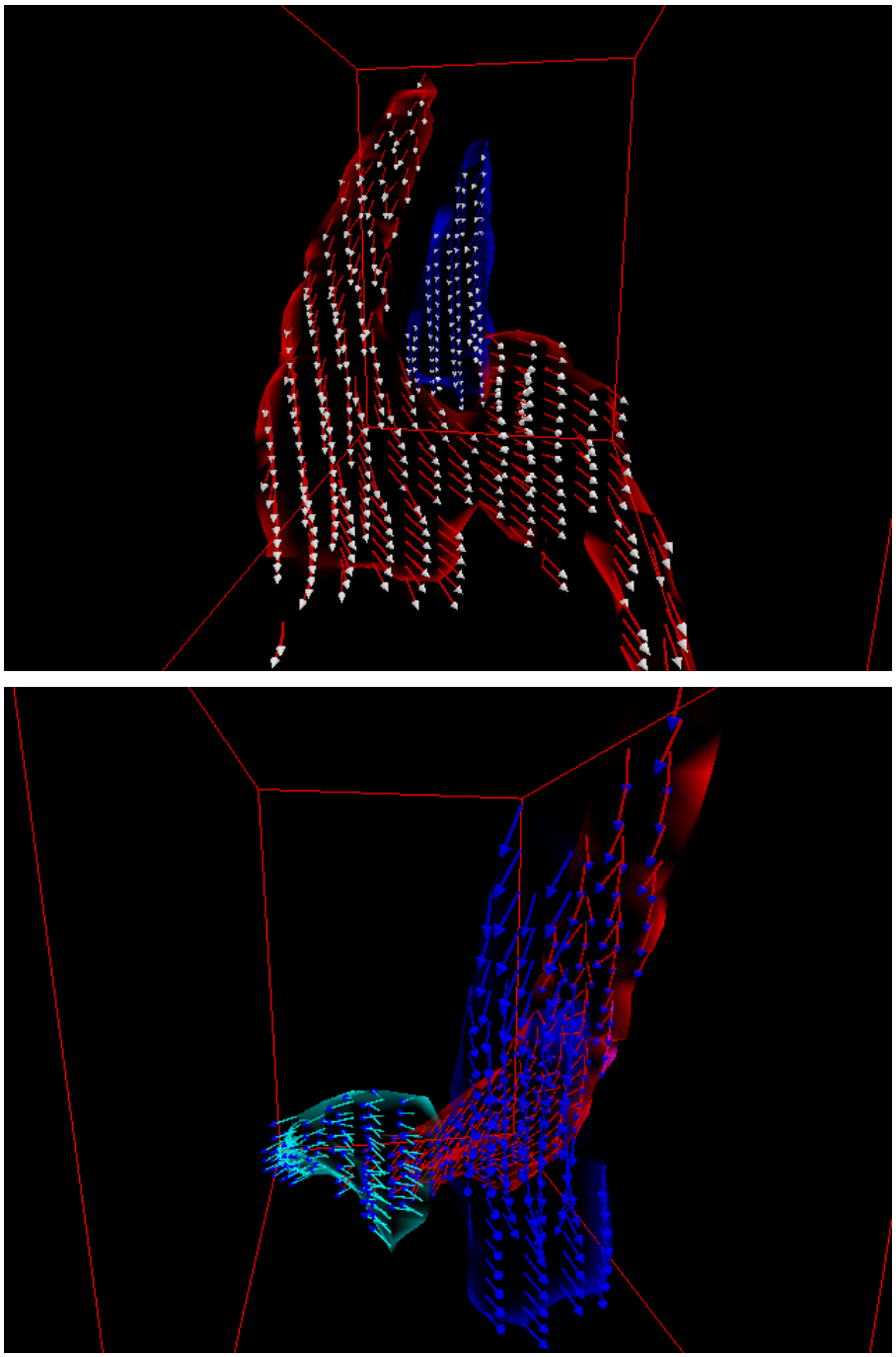

Figure 4.5: Vortex segmentation using vorticity $\bar{c}$ (Top) and normal vector $\bar{n}$ (Bottom).

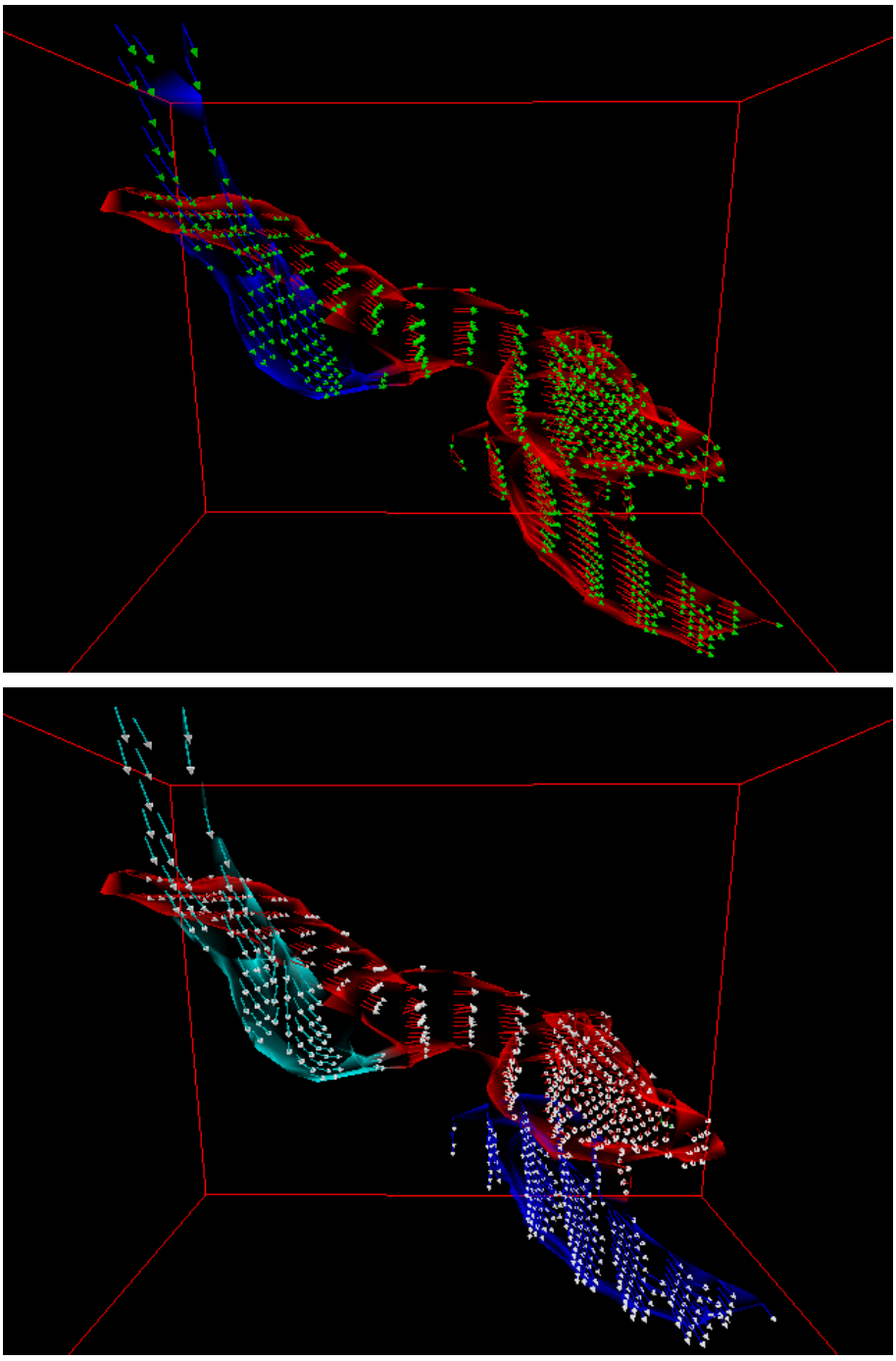

Figure 4.6: Vortex segmentation using swirl vector $\bar{r}$ (Top) and vorticity $\bar{c}$ (Bottom).

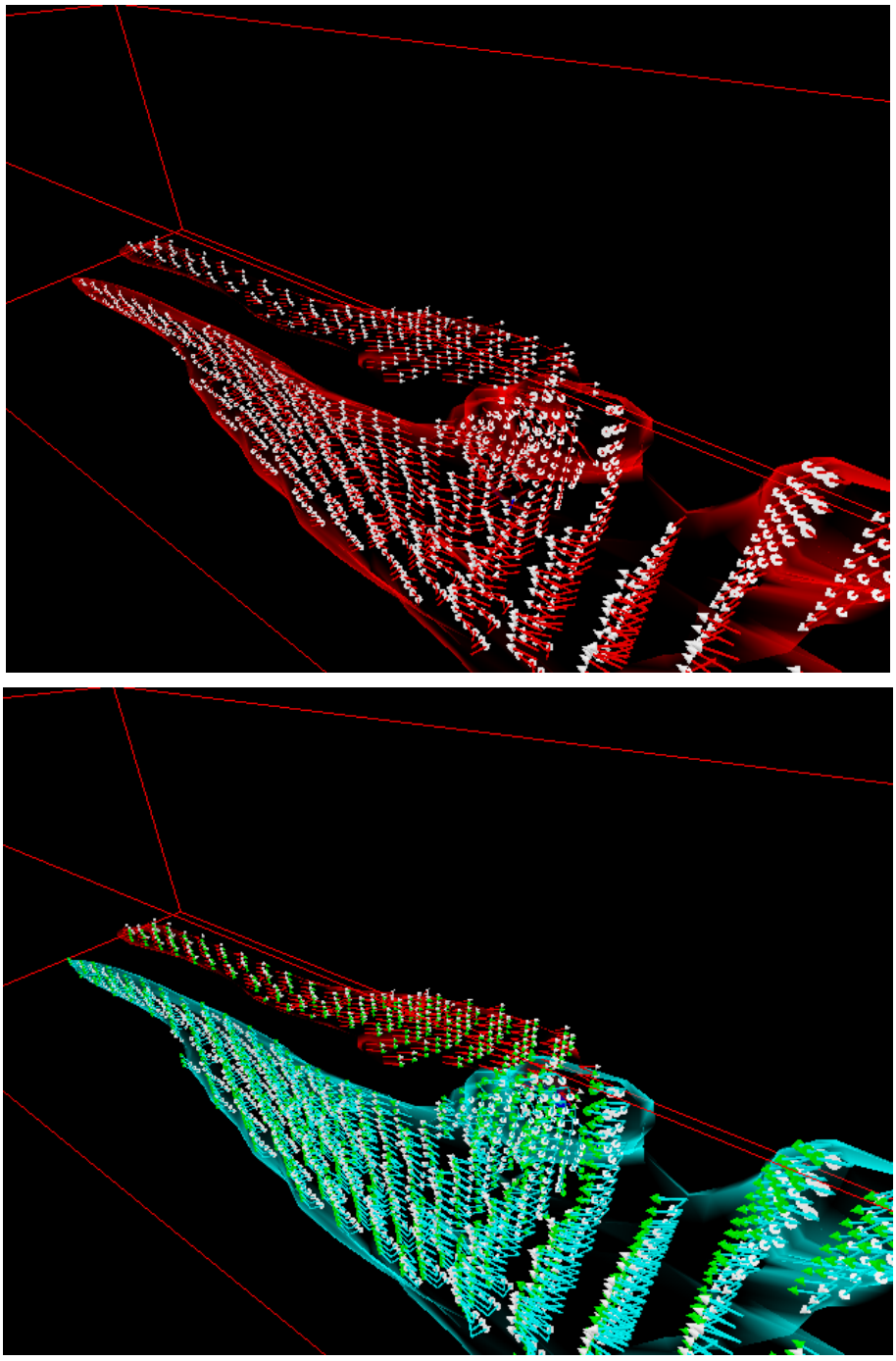

Figure 4.7: Vortex segmentation using vorticity $\bar{c}$ (Top) and both vorticity $\bar{c}$ and swirl vector $\bar{r}$ (Bottom).

4.6 Discussion

We have presented a novel method in this chapter for segmentation of individual vortices in turbulent channel flows within a boundary layer. Our method derives the underlying theoretical relationships among different measures of rotation direction in the flows. The possibility of using these properties for distinguishing different structures of vortices inspires a new research area. Combinational use of these rotation measures and the swirl quantity superiorly improve the segmentation of the vortical structures compared with only a single measure used. Further investigation of proper selection of thresholds and advanced coherence of these measures with respect to the fluid dynamics are left for future work. Our current method could convey clear representation of vortices with properly assigned colors on each distinct individual vortices, providing an effective visualization of vortices for advanced study of turbulent flows. In the future, we will apply our methods to different flows and investigate the potential capability of our approaches.

Chapter 5

Segmentation Using Vortex Cores

Vortices are the most fundamental feature in a turbulent flow field. Segmenting a clumped region is a new and interesting topic. Not only visualization techniques but also careful analyses are required to achieve this task. However, no previous research has proposed methods for answering this problem. We have investigated properties of vectors and quantities in turbulent flow fields in chapter 3, and observation of visual relationships could assist in the segmentation task in this chapter. The understanding of the variables relating to turbulence inspires us to further analyze and segment a connrected region in flow fields. The combination of variables and techniques in computer science and physics provides the capability of segmenting a complex region into individual vortices.

In this chapter, we propose a novel method for automatically identifying an individual (potentially compound) vortex in a flow and then identifying individual constituent vortices in each of these structures by leveraging fundamental known characteristics about the physics of flows. Specifically, we make use of the basic intuition that vortices

don't branch; each individual vortex in what appears to be a composite clump will generally be characterized by a separate core line. If we can robustly determine the core line locations, we should be able to use that information to accurately segment each cluster into its true constituent individual vortex. Essentially, our method works by integrating vortex core line detection with hierarchical region identification.

5.1 Vortex Region with Multiple Joint Vortices

Vortices are the most important physical phenomena in fluid dynamics. Their exact definition is not well understood so far. Chapter 3 has demonstrated vortex detection schemes to identify all vortices in the entire three-dimensional volume and also to isolate each one for advanced analysis. The previous results of turbulent channel flows show that the flows are more turbulent near the wall, the bottom of the volume, in which more vortices accumulate. Most vortices appear in the forms of very simple and thin tube or small blobs. However, some complex vortices existing in the strong turbulent areas may join together.

Different threshold levels can identify different swirling regions in a flow shown in figure 5.1. If a threshold for lower swirling regions is applied, larger regions are identified. Different vortices tend to be identified with connected regions. Structures of identified regions are more complex. If a threshold for higher swirling regions is applied, smaller regions are identified. Different regions tend to be separate, and the integrity of an original structure may be lost.

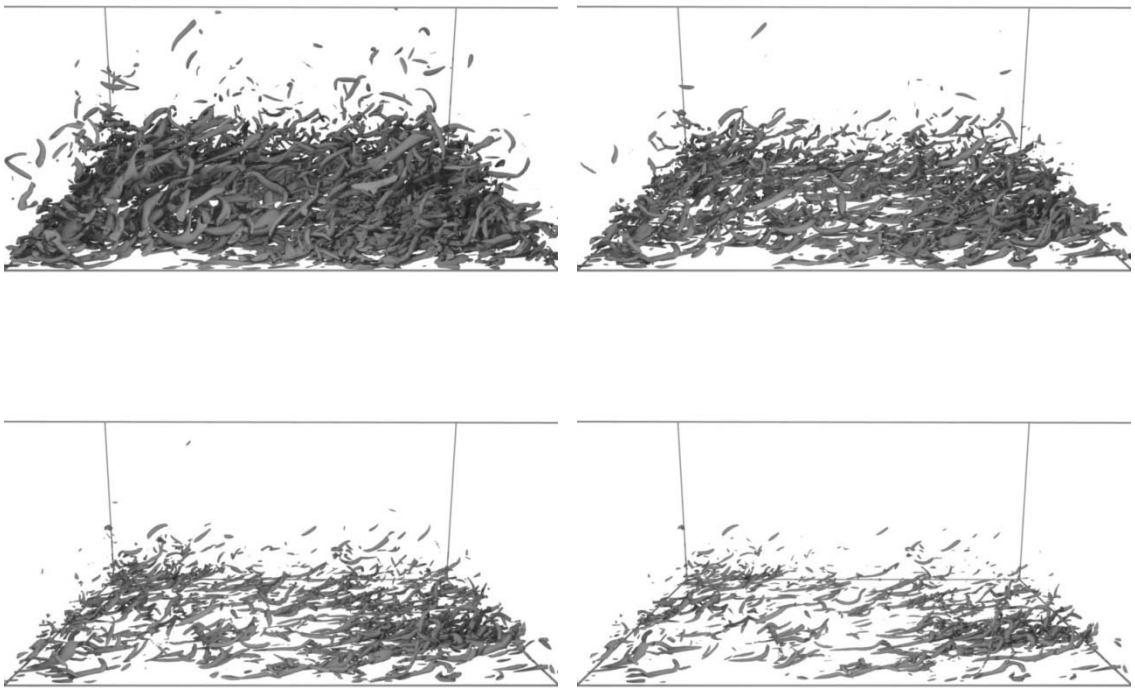

Figure 5.1: Upper left, upper right, lower left, and lower right images show different regions by four different thresholds which increase in equal steps.

Regions identified in a flow by a single threshold may be simple or very complex. Images in figure 5.2 represent two interesting vortices. The left image in figure 5.2 demonstrates a vortex composed of two roughly symmetrical elongated tubes joining each other near one end. The right image in figure 5.2 demonstrates a more complex vortex representing more than three elongated tubes with different lengths. In figure 5.3, an extremely complex connected region, the red entity, exists in the volume. In this chapter, we will develop an effective method for analyzing the structures of these entities and segmenting them into individual vortices. Our results have shown the success of segmentation tasks on different shapes of entities.

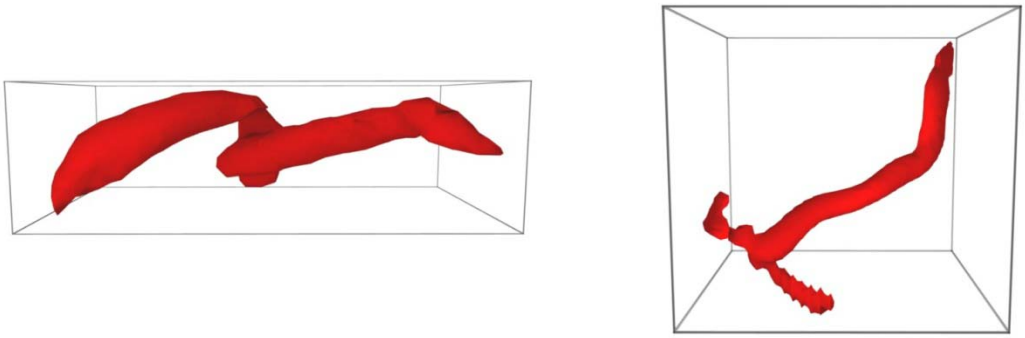

Figure 5.2: The left image shows a connected region with two roughly symmetrical elongated tubes that join each other near one end. The right image shows a region with three elongated tubes and one small blob that all join together.

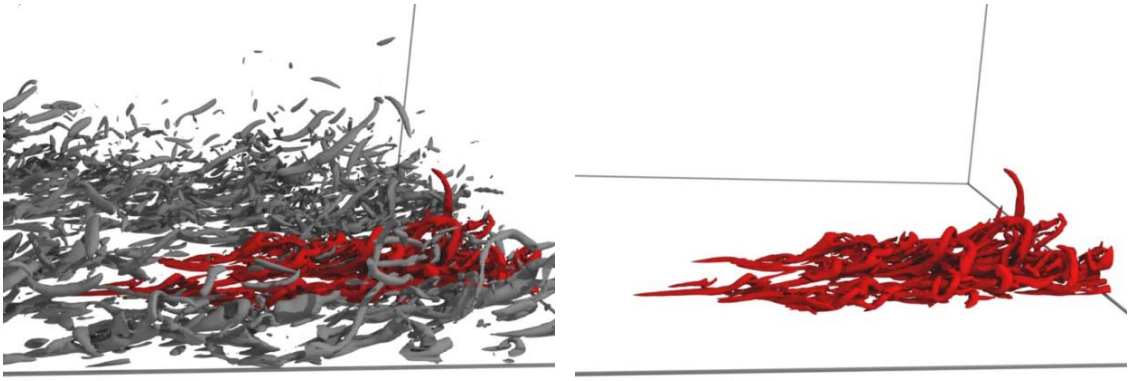

Figure 5.3: The left image shows an extremely complex connected region, the red entity, that exists in the volume. The right image shows the same entity in isolation.

5.2 Vortex Core Line Detection Method

The predictor-corrector technique [106] is one of the most effective methods of locating vortex cores in turbulent flow fields. This line-based vortex detection method could extract compact representation of the structures in the flow, reducing the amount of 3D flow data by a factor of an order or more. This technique performs well at producing

the continuous core prediction and self-correct algorithm, better than the eigenvector method [107] producing some core segments that cannot link to others. Moreover, it particularly captures the elongated vortices well, and the vortices with elongated tubes are the typical types of vortices we want to investigate in our dataset. We will describe the details of the predictor-corrector method and the version of our variation in this section.

5.2.1 Predictor-Corrector Method

The concept of predictor-corrector method is based on the vorticity-predictor and pressure-corrector methods. The procedure of this method is searching for seed points, extracting the vortex core line, as well as terminating the core line and will be explained as following.

1. Searching for Seed Points

The step of the predictor-corrector method is to search the entire three-dimensional flow data for proper seed points from which the vortex core will be grown. Seed points have to be located in the vortex core line. This method claims that the combination of low pressure and large vorticity magnitude are more likely to locate the candidate positions of the vortex core. The search is conducted through all grid points where pressure and vorticity magnitude satisfy their own thresholds respectively. The selection of these two thresholds for pressure and vorticity magnitude has to be careful. If these predefined thresholds are too strict, many

structures will be missed. If thresholds are too loose, there will be too many unnecessary seed points. This process is heuristic and could define the thresholds as some fraction of the extrema.

2. Extracting the Vortex Core Line

The purpose in this stage is to extract the vortex core lines from the seed points. After all seed points have been found, the vortex core will be constructed from those seed points. The algorithm is composed of two steps: First step is to predict next point in vortex core line according to vorticity. Second step is to move the predicted point to the vortex core line. As shown in the left top image of figure 5.4, vorticity ω_i is computed at a point v_i, which is located in the vortex core. This point v_i is a seed in the beginning. Next point v'_{i+1} is predicted according to the point v_i and the vorticity ω_i shown in the right top image of figure 5.4. Vorticity is not directly related to vortex. It is a rotation measure as a function of the instantaneous vector fields so the vorticity might proceed away from the actual vortex core. The predicted point requires to be moved to a correct location. Left bottom image of figure 5.4 shows that vorticity ω'_{i+1} at the predicted location v'_{i+1} is computed. Finally, the right bottom image of figure 5.4 shows that a point v_{i+1} is corrected from the predicted location v'_{i+1} based on the assumption in which the plane perpendicular to vorticity ω'_{i+1} at v'_{i+1} intersects the vortex core line at the location with pressure minimum in this plane. Repeating this two-step process from each new corrected point generates a series of points belonging to the vortex core line in one direction. Similarly, conducting the same process along the opposite direction of vorticity generates the other series of vortex core points in the

inverse direction. This stage plays the most important role in predictor-corrector algorithm and can most reliably depict the elongated vortices.

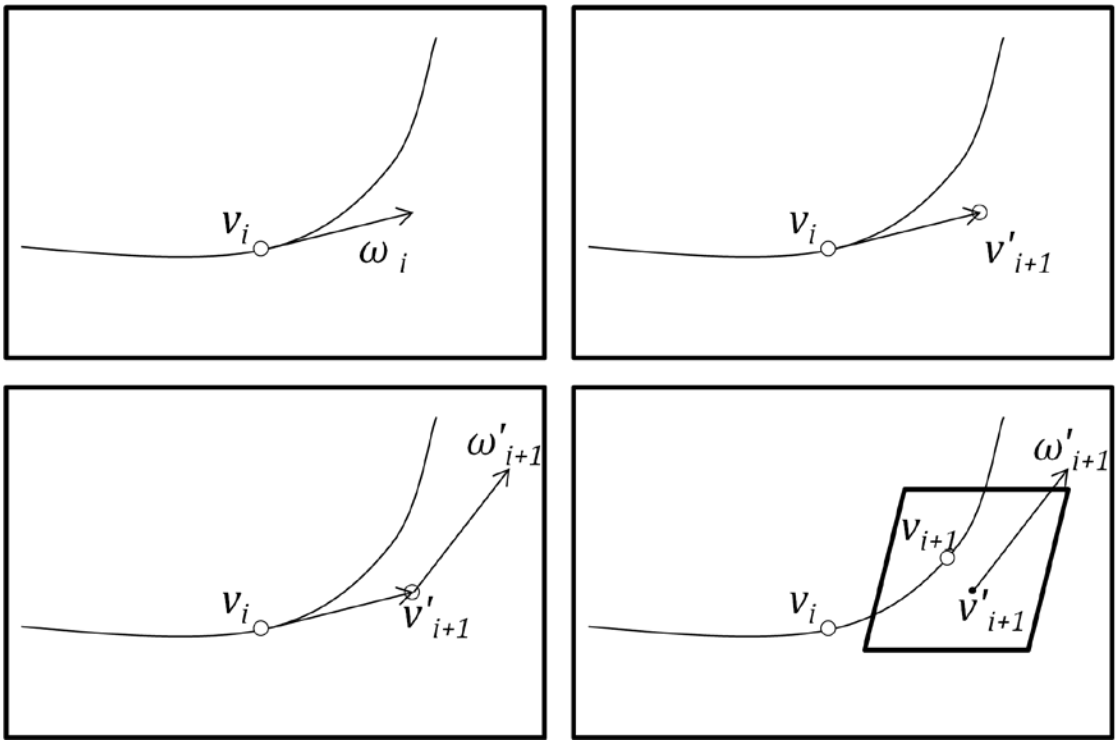

Figure 5.4: Upper left: vorticity ω_i is computed at a vortex core position v_i. Upper right: the next vortex core position v'_{i+1} is predicted from the last position v_i and the vorticity ω_i. Lower left: vorticity ω'_{i+1} is computed at the predicted vortex core position v'_{i+1}. Lower right: the predicted vortex core position v'_{i+1} is corrected to v_{i+1} according to the local minimum of pressure on the plane perpendicular to the vorticity direction ω'_{i+1} at position v'_{i+1}.

3. Terminating the Vortex Core Line

The vortex core line could terminate within the domain. However, vorticity terminates only when it reaches the domain boundary. The algorithm proposes some criteria for terminating the growth of the vortex core line. Firstly, if the vortex core line grows beyond the volume flow domain, it then terminates. The second condition states that the vortex core line terminates when the area of the

vortex cross-section is zero. This criterion is not sufficient because the core line might form a loop and never terminate. Therefore, the third condition states that termination occurs when the total arc length along a vortex core line increases more than twice the length of the longest grid dimension of the flow data.

5.2.2 Variation of Predictor-Corrector Method

The predictor-corrector method proposed by Banks and Singer [106] applies vorticity-predictor and pressure-corrector to locating vortex cores. We modify this algorithm for each stage so that the new algorithm can perform well in our application and dataset. The variation for each stage is explained below.

1. Searching for Seed Points

The predictor-corrector method uses high vorticity magnitude and low pressure to locate the vortex core. However, this method requires two thresholds for vorticity magnitude and pressure respectively. If threshold values are too strict, many structures in the flow will not appear. If thresholds are too loose, there will be too many seed points, and there might be many grown core lines indicating same vortex cores. In addition, many unimportant structures may also appear in this situation. In order to prevent these drawbacks, we start to grow a line from the grid with maximum swirl strength within a certain region. Multiple vortex cores indicating same vortices are reduced since the seed, maximum swirl strength, in each region is unique. In addition, one quantity, swirl strength--instead of two

quantities, pressure and vorticity magnitude--is considered for location of vortex cores; number of thresholds required is reduced as well.

2. Extracting the Vortex Core Line

We use vorticity-predictor and swirl-corrector rather than pressure-corrector in this dissertation because we use swirl strength suggested by Zhou [2, 3] to identify vortex regions. For extracting the vortex core, we suggest applying swirl strength, which is the same quantity in our method for identifying vortex regions instead of pressure quantity in order to provide the consistency of the vortex core with respect to the vortex region. Therefore, the algorithm in this step is almost exactly the same as the predictor-corrector method except we reference swirl strength in the corrector stage.

3. Terminating the Vortex Core Line

The termination criteria in the traditional predictor-corrector method consist of three conditions. Firstly, the vortex core line terminates when it exceeds the 3D turbulent flow domain. Secondly, termination occurs when the area of vortex cross-section decreases to zero. We can reduce the computation and complexity of calculating the cross-section information of the vortex since that information is not required in our application. We terminate the core line simply when it grows beyond the vortex region. Thirdly, termination occurs when the length of a vortex core line is longer than twice the length of the longest grid dimension of the 3D flow data. Two additional criteria are added in our application. The fourth condition states that the angle formed by the successive three points cannot be too

large. This is because our application detects next points located in the vortex core by a very short step, and the curvature is small within a short segment. Considering that extremely short successive segments form a nearly straight line in the extreme case, two successive segments formed by three successive points cannot have a large angle. Moreover, in order to prevent failure to detect the maximum swirl strength in the correction step, the fifth condition states that the next point in the vortex core cannot exceed beyond a threshold from the current point.

5.3 Segmentation of Individual Vortices

In chapter 3, our particle representation for multivariate visualization has demonstrated the inner structure of the vortex region effectively. Interesting properties of variables in the flow field have been found. Vorticity has strong relationships to vortices and is one of the most interesting of the variables. Firstly, the vorticity direction indicates how vortices rotate and implies indication of the curve of the vortex core. Secondly, the vorticity orientation has high correspondence with respect to the shape of the vortex region. Thirdly, vorticity tends to follow the vortex tubes, maintaining the orientation with respect to their corresponding tubes. Significant difference of orientation has been found among different vortex tubes near the joint region. Fourthly, swirl quantity has higher strength in each tube, and the areas with higher swirl strength are not located within the joint region.

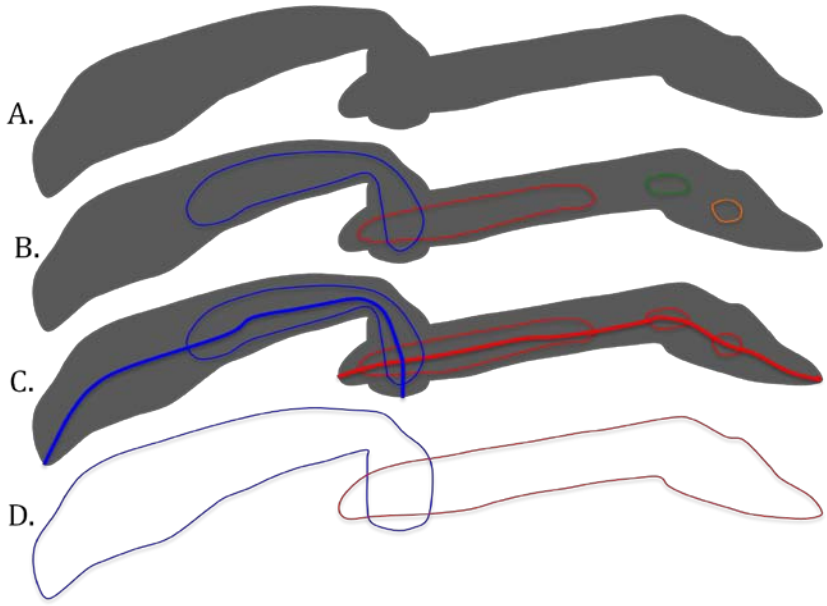

Figure 5.5: These four images illustrate the basic concept of the segmentation algorithm presented in this chapter. Image A shows an interesting region of the flow, consisting of two elongated touching tubes. Image B shows some candidate sub-regions inside the interesting region. Image C shows that some of these sub-regions are joined by vortex core lines, and two groups of related sub-regions have been identified. Image D shows that the group information enables the segmentation of the compound region into two distinct vortices.

Based on the observations above, an algorithm is developed to have the capability of performing segmentation of individual vortices. The key concepts of this algorithm are based on the combination of vortex region identification and vortex core line detection methods and are shown in figure 5.5. This approach basically identifies vortex regions as candidate individual vortices and correlates those candidate vortices according to detected vortex core lines. In addition, a technique of hierarchical vortex region identification is developed. More details of this algorithm are shown in figure 5.6 and described below:

1. Identify an Interesting Vortex

We begin by identifying a potentially compound structure defined by a connected set of voxels that correspond to locations in the flow where the swirl strength is higher than a specified threshold level. An example of such a structure has been shown in red in figure 4.1 in the context of other surrounding structures (drawn in grey) within a small region of the flow; the same structure is also shown in figure 5.9 (Top) in a closer view without the surrounding structures. A more complex example shown in figure 5.3 demonstrates that a very large compound entity may exist as well. This initial structure is defined by building the connectivity of each of the grid points in an entity, and all the grids are examined.

2. Determine Candidate Sub-Vortices

Once we have identified a single connected region, we begin the process of determining whether and how it should be segmented. Our fourth statement above shows that the regions with higher swirl strength are located within each individual vortex and are not located in the intermediate region where multiple individual vortices intersect. This fact inspires us to use higher swirl strength to provide the preliminary segmentation candidates. We initially consider the swirl strength at the threshold level close to the highest strength within the interesting vortex. Sub-vortices, at least one, are identified as candidate sub-vortices at current threshold level.

3. Determine Seeds for Each Candidate Sub-Vortex

The criterion for searching for the seeds discussed in the section on our adaptation of the predictor-corrector method is based on the assumption that each sub-vortex belongs to only one individual vortex. We will extract vortex core lines for each

candidate sub-vortex. To best represent core lines that correspond to each blob of vortices, we examine each region to find the position of its strongest swirling motion. The seed is determined from all grid cells within each sub-vortex and identified in each region where the swirl strength assumes a maximal value.

4. Extract Vortex Core from Each Seed

The vortex core is grown in both directions from each seed according to the vorticity and swirl strength as stated in our adaptation of the predictor-corrector method described by Banks and Singer [106]. Our work relies on vorticity and swirl strength, which is the same approach reported by Stegmaier *et al*. [104], rather than vorticity and pressure for the prediction and correction steps. The criteria we use to determine when to terminate the extension of a vortex core line are essentially similar to Bank and Singer's work as follows. Firstly, we ensure that the vortex core line does not extend beyond the boundaries of the domain. Secondly, we stop tracing a core line when the cross sectional area of the portion of the structure through which the core line is currently passing decreases to zero. This scheme can be simplified as a stop criterion of terminating the core line when it exceeds the interesting vortex region. Thirdly, as a safety precaution, we terminate the growth of a core line if it reaches a total length that is more than twice as long as the longest side of the domain. Therefore, there will be distinct vortex core lines expanding from or penetrating each sub-vortex.

5. Merge Sub-Vortices on Same Vortex Core

This stage determines if any sub-vortices belong to a same individual vortex. If the vortex cores emanating from each region intersect the other region, we consider the two sub-regions as belonging to the same vortex. Because the vortex core line paths can be noisy, we also need to consider additional circumstances. If one of the vortex core lines passes very close to but just misses intersecting the subregion from which the other emanates, and the second subregion is very small, we also consider the two subregions as belonging to the same structure. The decision of how close two lines are considered to represent a same vortex core is, in fact, not sensitive. We can consider a simple algorithm that determines the distance between two vortex core lines by picking only several points on the core lines such as seeds, end points, or others. We allow each point to be in two-grid distance within another core line representing the same vortex core. If the total distance of those points with respect to the other core line exceeds the total threshold length, we decide these two lines belong to different vortex cores, and vice versa. This criterion is not sensitive and strict since the two distinct vortex core lines are usually spacially distinct, and the distance between two lines is basically very large. This implies the computed distances of two lines representing a same vortex core or two distinct vortex cores form two distinct clusters, which can be separated by reasonable selection of a decision boundary based on the number of points which decide the distance of two lines. Besides, not only the distance but also the rotation direction of two core lines has to be considered. Only two vortex core lines with the same rotation direction can be considered as the same one. The good choices of points determining core distance includes both

ends of core lines because it is common that a vortex may consist of fat blobs inside the elongated vortex, introducing the possibility that two core lines branch within that area due to a discretization of the domain and computation inaccuracy.

6. Determine Segments by Sub-Vortices

After vortex core lines have been extracted, the expansion of the regions from grid cells of individual candidate vortex cores is conducted by a recursive flood fill algorithm from each seed or the lines and simplified K-Nearest Neighbor clustering algorithm with only a single pass at each iteration. Then, the grid cells within the compound vortex are categorized in different groups, and each group of grid cells belongs to one of the individual vortices.

7. Store and Update Temporary Segmentation Results

At each step in this hierarchical progression, as new subregions develop, we determine whether or not they should be classified as an extension (possibly dis-connected) of one of the existing subregions or as an independent subregion belonging to a different component vortex in the compound cluster. We make this determination on the basis of the paths taken by the vortex cores through each subregion. The previous stage produces a temporary segmentation result for a compound vortex. This result has to be stored so that the program can start over on another examination with similar processes. We can store these data in the memory because the sub-domain we are examining is relatively small and the information we retrieve can be compacted together.

8. Examine Another Candidate Level

After this, we successively consider subregions, within our initial structure, that are defined by decreasing threshold levels of swirl strength, beginning from the maximum value and continuing down to the value that was used to define the extent of the initial structure. We continue this process until all threshold values of swirl strength have been examined. The number of iterations with the decreasement of threshold values can be predefined or based on how many more individual vortices are detected. In the extreme case, we could run through all the threshold levels for extracting core lines exhaustedly, which is virtually a parameter-free approach in this stage. However, this ultimate case is not achievable according to computation theory. Selecting too many threshold levels would be time consuming without much gain, and it may possibly introduce false positive detection of vortices especially where noises exist. Our algorithm examines multiple candidate levels, one each time, to insure that all individual vortex cores can be identified. When all levels have been examined, our algorithm proceeds to the next stage.

9. Determine Individual Vortices by Segments of All Candidate Levels

This stage is similar to stage 6. However, we consider all the segments stored from each intermediate iteration, and determine final individual vortices existing within the interesting region based on all previous results. Stage 6 may be skipped for efficiency as long as the intermediate result of segmentations is not required for display. Sub-vortices from all candidate levels with the same or similar vortex

core lines are considered as the same group. The final individual vortices are determined by expanding regions from different final candidate sub-vortices.

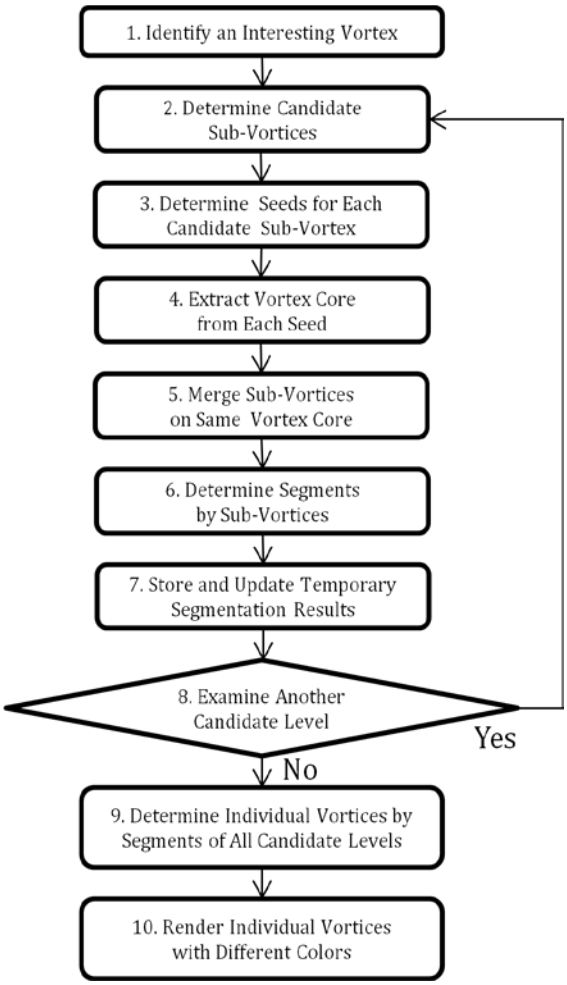

Figure 5.6: This flow chart describes the algorithm used for the segmentation of individual vortices.

10. Render Individual Vortices with Different Colors

At the last step, each different group of grid cells is assigned one distinct color that is given by a random procedure; and all primitives are painted according to the color of its own group. This target vortex is rendered with different colors, each

for one individual vortex. The segmentation procedure of a vortex is completed, and the results are visualized.

5.4 Experimental Results

Our hierarchical vortex identification method successfully segments a variety of compound regions into individual structures, and clearly renders each structure by distinct colors. Hierarchical level regions provide premature information for the candidate sub-vortices, and the corresponding core lines are used to correlate different candidate sub-vortices with each other at each level region. All possible levels are examined to determine the proper categorized regions. The results are shown in a series of figures below.

The left image in figure 5.7 shows the intermediate result of the segmentation algorithm. The semitransparent boundary is the identified interesting vortex. Several opaque blobs inside the interesting vortex represent the candidate sub-vortices. There are several vortex core lines starting from one sub-vortex, penetrating the interesting vortex region, and connecting to another sub-vortex. These connections group different disjoined sub-vortices together and only two groups remain in the end. The sub-vortices in these two groups are determined and painted by two colors, red and blue. The right image in figure 5.7 shows the final result of this algorithm that segments the vortex clump into individual vortices. Two different colors, red and blue, indicate two

distinct individual vortex tubes clearly in the images. This result matches our intuition in which two vortex tubes with distinct orientation tend to be separated apart.

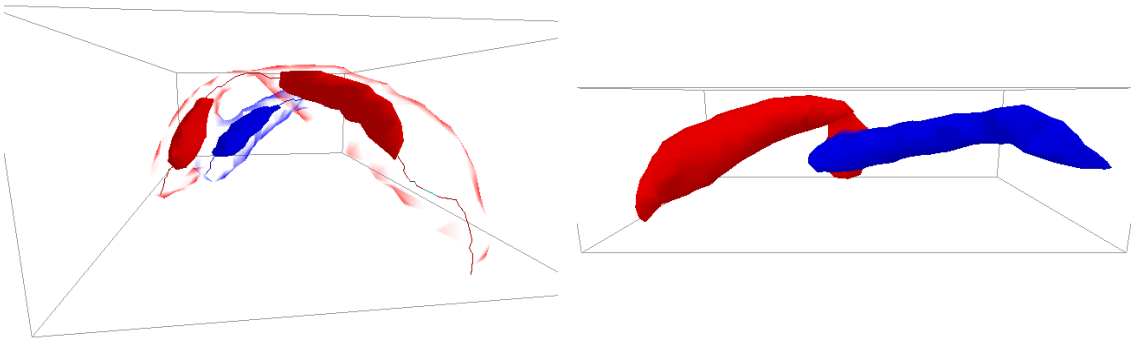

Figure 5.7: The left image shows the intermediate result of the vortex segmentation algorithm. The right image shows the final result of the vortex segmentation algorithm. Two individual vortices are identified and distinguished by using red and blue colors.

Figure 5.8 shows another successful case of our algorithm; a formerly compound structure is successfully segmented into four component pieces. The images illustrate two intermediate results at different hierarchical levels and a final image. In the top image, we can see three groups of sub-regions are identified by using multiple core lines grown from seed points located within long blue, small cyan, and tiny red sub-regions. The middle image shows that four groups of sub-regions are identified with the additional tiny cyan blob. The green and cyan blobs in this figure compose a larger cyan portion in the top image. The cyan blob in the middle image is identified at current swirl level but not at the previous levels. A transparent layer in these two images encompasses these candidate sub-regions and illustrates our interesting target clump. Different colors of a transparent layer represent different individual vortices corresponding to the candidate sub-regions at the current threshold level. The bottom

image shows the final result of our algorithm. This approach successfully considers all possible sub-regions detected at each threshold level and makes an overall decision for final segments of a connected region.

Figure 5.9 shows that our algorithm clearly demosntrates the segmentation of a complex connected clump with different topology of individual vortices. We can see a compound structure that has been automatically segmented into eight different portions. The size of each segment varies, and the ways in which segments connect are also different. Each component in the structure appears to be appropriately defined, with the possible exception of the large red structure that may or may not remain in another compound form.

Figure 5.10 illustrates a sucessful application of this algorithm on an extremely complex and large connected clump. Each individual vortex in this extremely complex constituent entity is identified and segmented properly, and rendering with distinct colors on each individual vortex makes visualization of distinct segments effective. Figure 5.11 shows that the individual vortices can be identified from this extremely complex connected clump. Further analysis of each individual structure and the organization can be investigated.

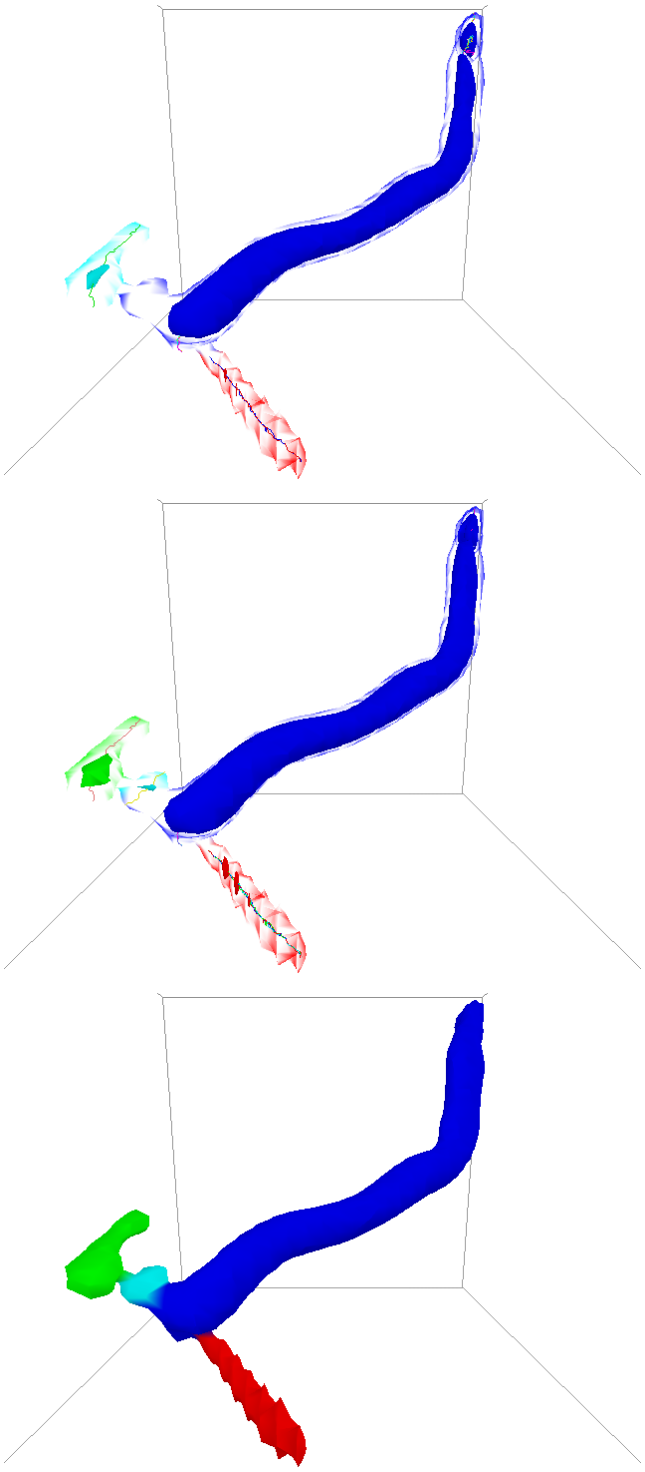

Figure 5.8: A success case of our algorithm. The top and middle images show the different segments that are identified at each intermediate level, and the bottom image shows the successful segmentation after multiple iterations.

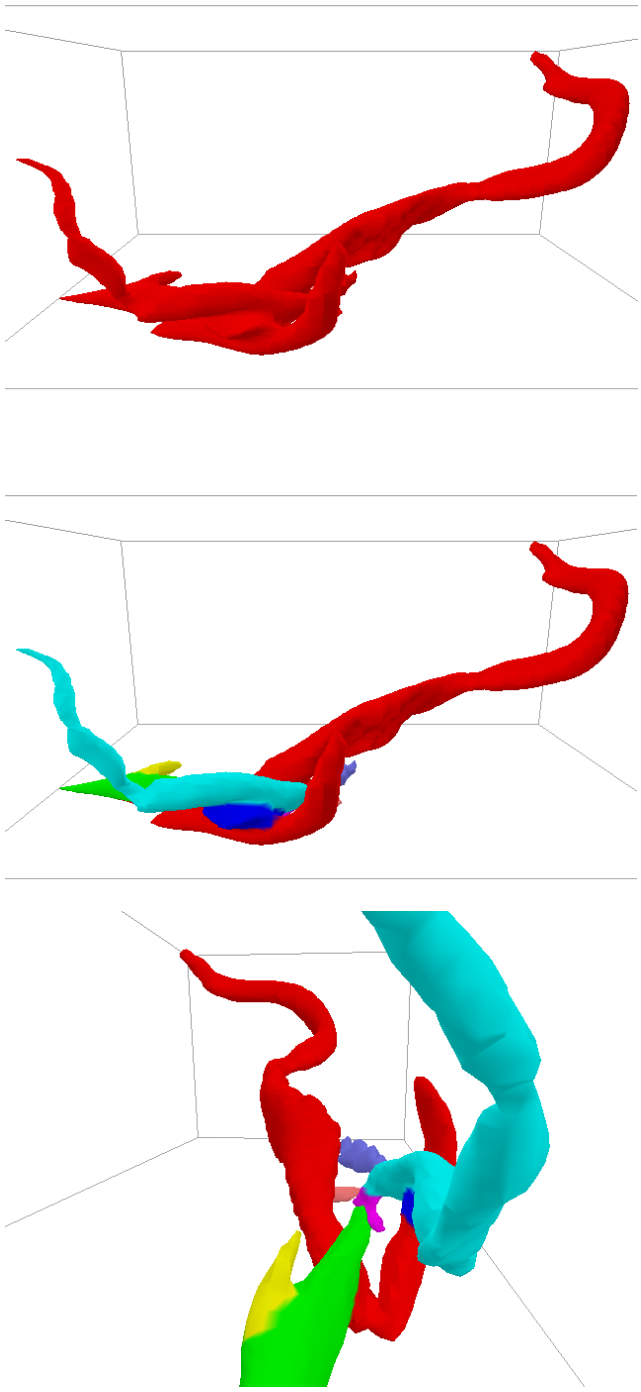

Figure 5.9: Another automatic segmentation produced by our algorithm. The top image shows one connected clump. The middle and bottom images show the segmentation result with eight individual vortices from different viewing angles.

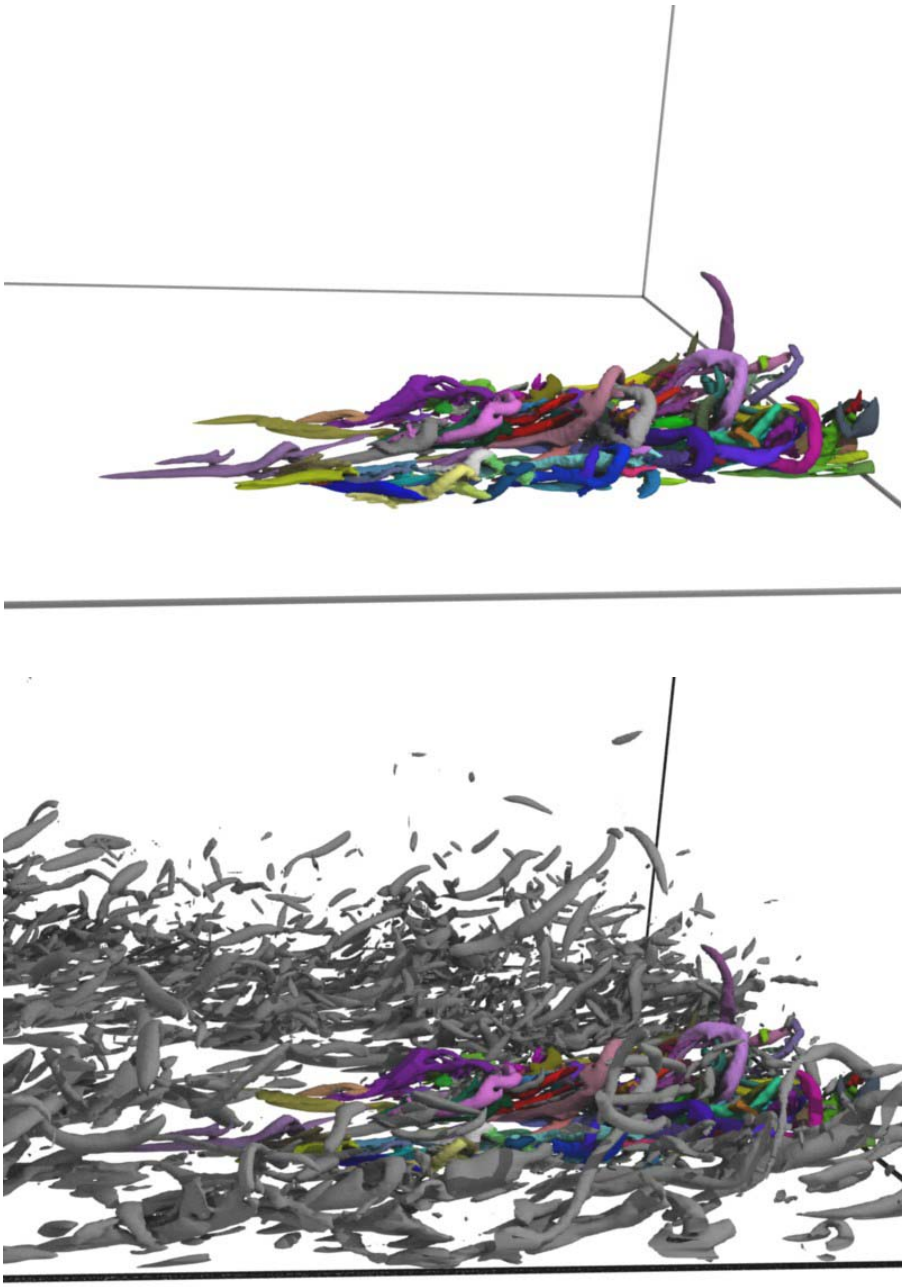

Figure 5.10: The top image shows a successful segmentation of a very complex and large vortex clump. The bottom image shows the individual vortices of this region in the context of the surrounding flow.

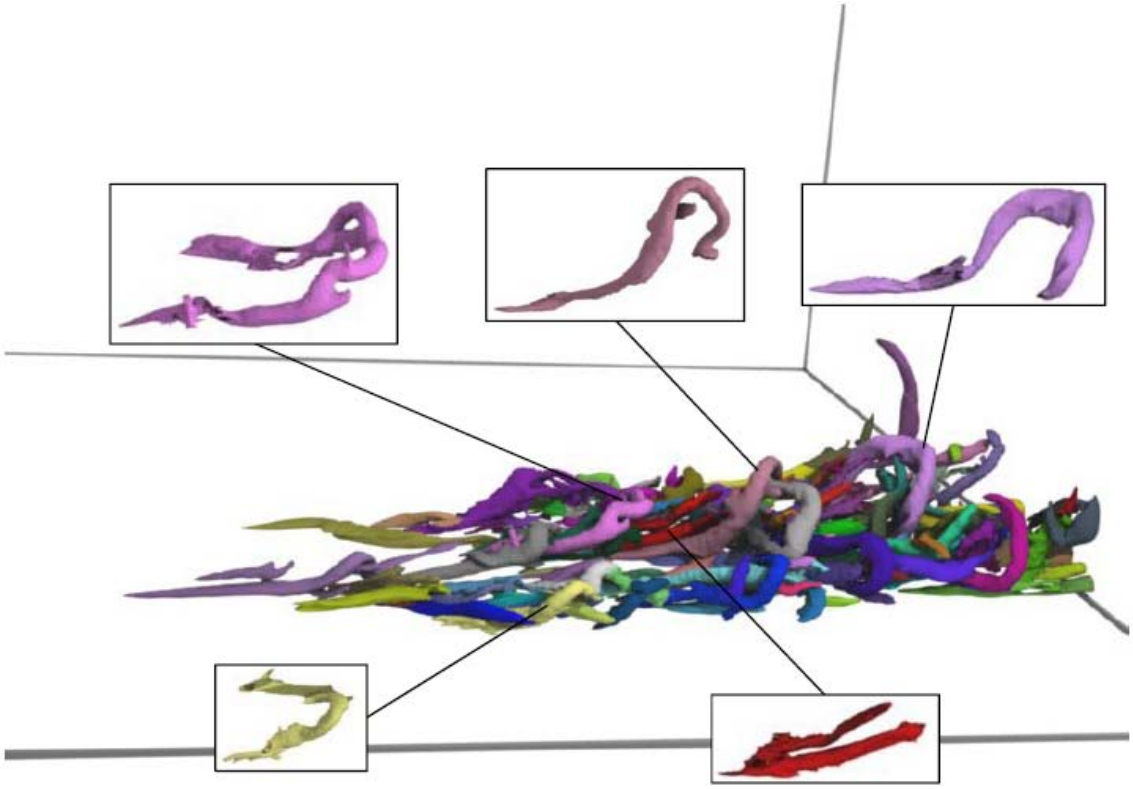

Figure 5.11: This image shows that the individual vortices can be identified from this very complex and large vortex clump.

5.5 Sensitivity Analysis

Sensitivity and robustness of our segmentation method are important issues for investigation. A significant factor in our hierarchical vortex segmentation method that influences the results is the design of the iteration. We can expect that more segments will be identified when more iterations of segmentation are performed. An experimental study of how the number of segments changes when the number of iterations changes is discussed below.

Figure 5.12 shows careful analysis of the number of threshold levels with respect to the number of individual vortex segments. Two vortices, Structure2128 in figure 5.8 and Structure0110 in figure 5.9, are analyzed. Number of threshold levels used ranges from six to nineteen in our study. The number of threshold levels influences the selection of thresholds. Generally, threshold levels near high swirl values are less sensitive to the number of final segments identified. That is because regions of extreme swirl values are too sparse to represent the structure of a vortex. Another reason is that regions identified are less sensitive to the threshold change for a high swirling region. In order to make the best use of threshold levels, nonuniform selection of levels between maximal swirl value and interesting target value are performed with sparsely selected levels near higher swirl values. Moreover, a too large number of threshold levels is not required since the selection of threshold levels with reasonable distance between successive levels has been a good design for capturing important vertical structures.

The horizontal red line in figure 5.12 shows the stable outcomes of segmentation throughout the entire range of level selection in this case study of the entity Structure2128. This entity is composed of the simple vortical structure with four individual vortices and can be correctly segmented by only six iterations. The complex one, Structure0110, generates different segmentation results while more levels are applied. The overall trend of segment number tends to increase until all possible individual vortices at fourteen iterations are captured. However, at thirteen iterations, the number of vortex segments decreases. This result implies the curve of the trend may not be monotonic. The reason for this is that the selection of levels at each number

is independent, which does not guarantee the monotonism of the curve. The purpose of independent level selection is to make the best use of each level according to the number of threshold levels for distributing the threshold selections over the range properly. When the number of levels is large enough, the results of segmentations tend to converge and be stable. In addition, uniform selection at number nineteen is applied, and number of segments remains eight. This result shows that more levels in the higher swirl values do not obtain more segments, and neither do too many levels.

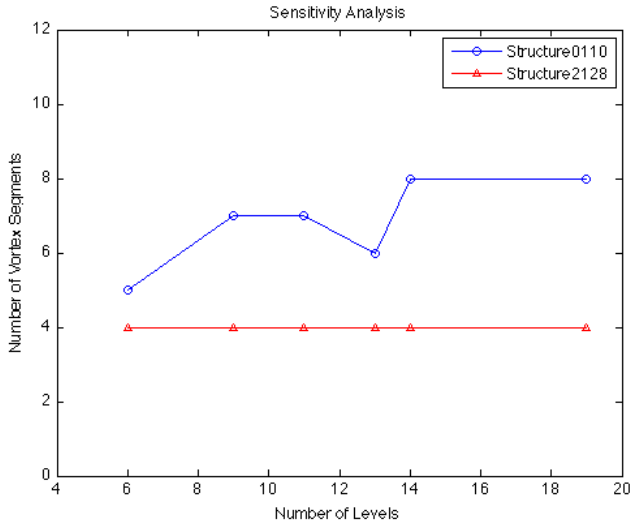

Figure 5.12: An experimental investigation of the sensitivity of the segmentation to the number of threshold levels used, for two different compound regions.

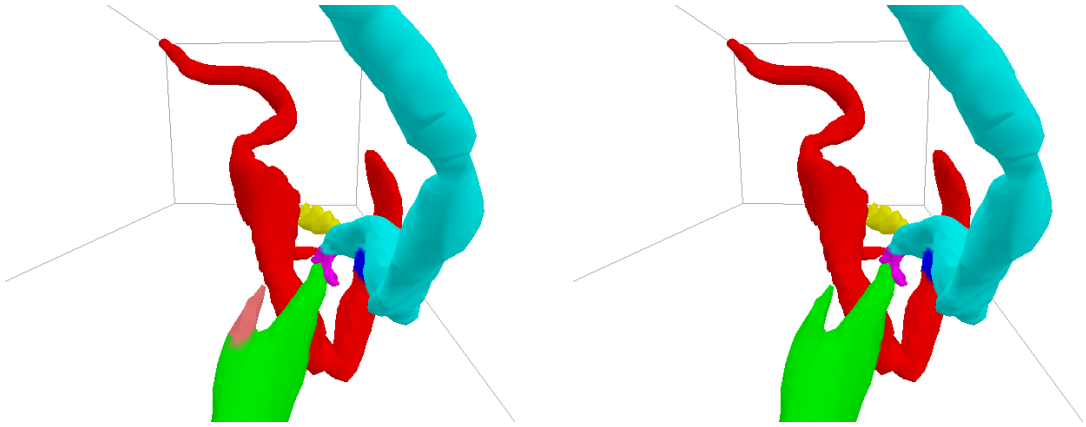

Figure 5.13: The left image shows seven major individual vortices captured by iterations at eleven threshold levels for the complex region, Structure0110. The right image shows six major individual vortices captured by interations at thirteen threshold levels for the same complex region.

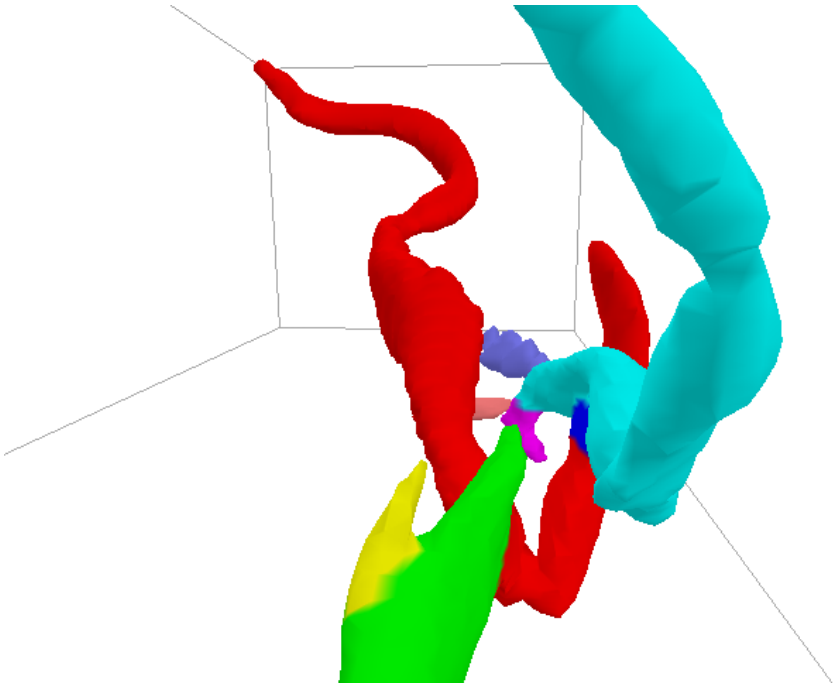

Figure 5.14: Eight major individual vortices are captured by iterations at fourteen and nineteen threshold levels for the complex region, Structure0110.

Figure 5.13 and figure 5.14 show the difference of segments with regard to the total level numbers, eleven, thirteen, and fourteen respectively. A small portion of the green structure in the right image of figure 5.13 is missing. Figure 5.15 explains the reason

why this portion is not identified. When the swirl strength increases, the corresponding regions shrink from black, blue, red, yellow, to green. Except for blue regions containing two subregions, all other regions consist of only one region, and, thus, only one subvortex is identified. In this figure, the blue region contains a small separate subregion, and this subregion indicates a small range of swirl strength variation. It is only when the threshold value is selected within that range, that two subregions are identified. In other words, when the number of threshold levels is large enough to cover that value range, two subregions can be identified.

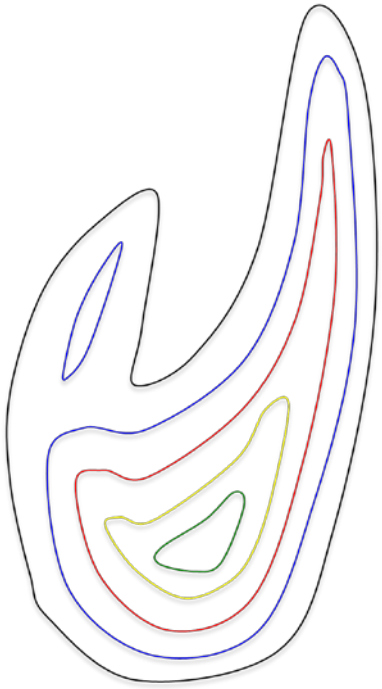

Figure 5.15: This image shows the reason leading to the decreasing number of segments found using certain numbers of threshold levels.

Overally, major individual vortices are identified and rendered even though only a few iterations are applied. Our results show that our method might have a chance of missing a certain portion. However, the portion which is not identified is small and might be

less important. If a method is sensitive enough to capture all existing structures, this capability may introduce a serious issue of noise identification. The problem of noises can be seen in chapter 6 for segmenting vortices in our experimental vortex ring dataset.

5.6 Statistics Analysis

Statistics information of the entire volume can be investigated through automatic analsysis procedure. This procedure analyzes and retrieves turbulence attributes automatically and provides overall information that can assist scientists in obtaining a global view of flow data quickly. Interesting attributes include vortex entities' number, volume, location, segments, and possibly relationships across attributes. The automatic procedure is performed to retrieve attributes from our turbulent channel flows and provides the table and figures below.

In table 5.1 and figure 5.16, one pass of our segmentation algorithm is performed on all connected entities in the flow volume, and distribution of entity segmentation is provided. There are 3047 entities in the volume. Most of the entities, 97.47 %, consist only of a single individual vortex. This type of vortex entity has only simple forms like small blobs or elongated tubes.

The left image in figure 5.17 shows the distribution of all vortex entities in the entire field. Even though some very large entities may exist, most of them are relatively small.

The right image in figure 5.17 plots the distribution of the 100 largest entities in the field and shows that few entities are relatively large.

Segment	Count	Percentage	Segment	Count	Percentage
1	2970	97.47	7	2	0.07
2	49	1.61	8	0	0.00
3	11	0.36	9	1	0.03
4	8	0.26	10	2	0.07
5	0	0.00	11	1	0.03
6	3	0.10	Total:	3047	

Table 5.1: This table shows, for each connected region in our dataset, the number of constituent vortices detected using one pass of our segmentation algorithm.

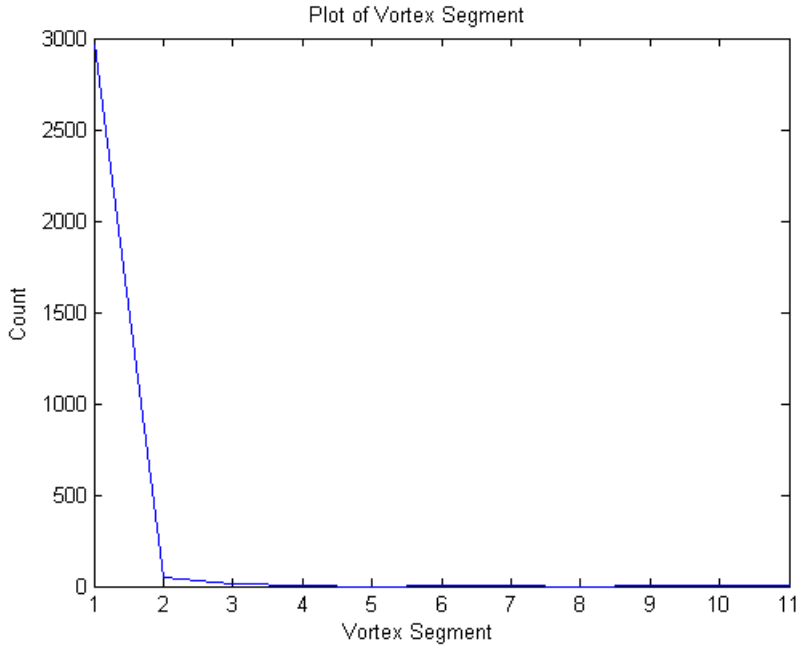

Figure 5.16: This image shows, for each connected region in our dataset, the number of constituent vortices detected using one pass of our segmentation algorithm.

Figure 5.18 shows the images for the locations of all vortex entities. The entity's location is computed according to its centroid and is represented by a dot. Therefore, very simple 3D plots are created from different view points. These plots clearly convey locations and distribution of all entities whose density is higher near the bottom.

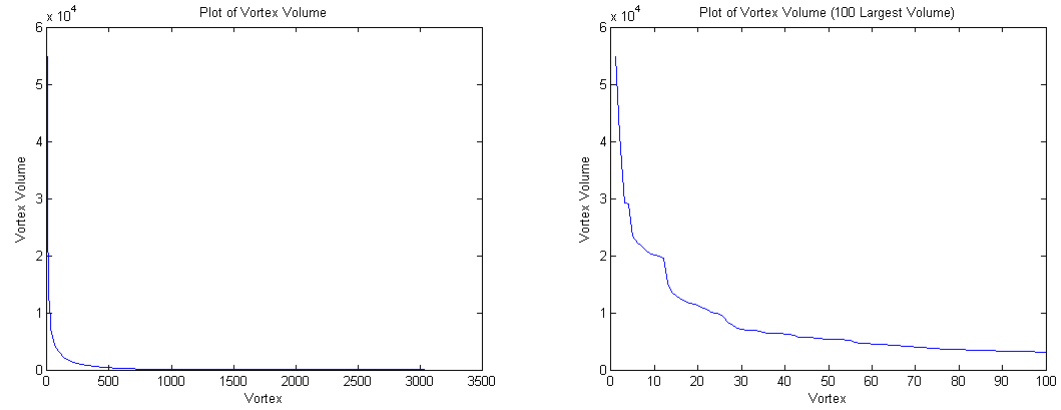

Figure 5.17: The left image shows the volume distribution of all connected regions. The right image shows the volume distribution of 100 largest connected regions.

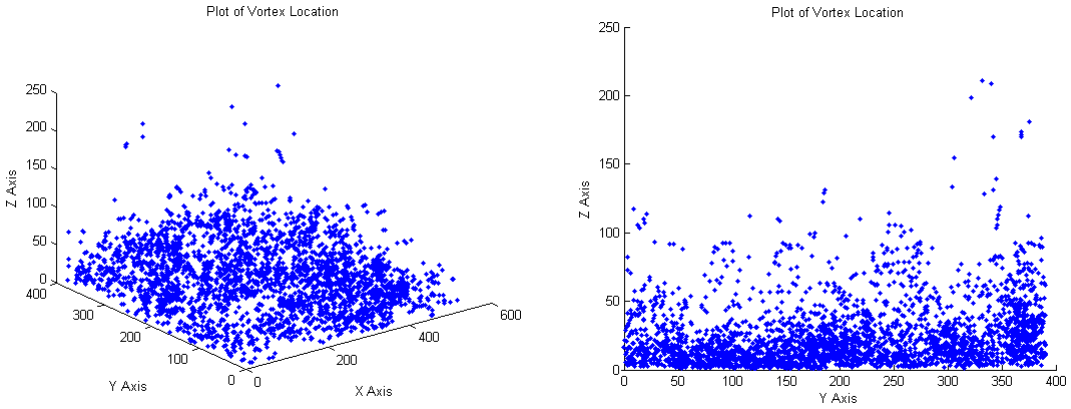

Figure 5.18: The left image shows the distrubiton of detected structures. Locations of the entities' centroids are represented by dots. The right image shows the same distribution on the Y-Z plane.

5.7 Discussion

In this chapter we propose and explain a novel algorithm which can perform segmentation on a connected complex region for individual vortices. We investigate a vortex core detection method, the predictor-corrector method, and develop its adaptation for our segmentation application. Our segmentation algorithm combines both vortex region identification and vortex core detection methods for segmenting a complex connected region into individual vortices. The vortex region identification method usually cannot distinguish among vortices which are too close, and the vortex core detection method may introduce multiple cores indicating the same vortex. The combination of our algorithm overcomes the disadvantages of these two types of methods. It enables the capability to identify individual vortices in an extremely complex connected region by searching all the potential candidates of sub-vortices through the technique of hierarchical vortex region identification.

This algorithm is not sensitive to the threshold selection even though a small variation of results may exist. The decision of this algorithm for identifying distinct individual vortices is made by a series of criterion that is not sensitive to the predefined internal thresholds. In order to achieve a parameter-free approach, the hierarchical vortex region identification with vortex core line extraction is developed, and our method completes segmentation tasks of various compound regions successfully. In our experiments, a simpler structure of vortex is stable to the result of identified vortex segments. Even though the iteration number may still affect segmentation results on

complex regions, main structures are identified effectively. Generally, this method identifies major structures very well by the task of vortex segmentation and is expected to be applied to a wide range of vortex topology. With the significant results of segmentation tasks, vortex structures can be rendered effectively with distinct colors on different segments. Our experiments have demonstrated the effective way of conveying the segmented vortices.

In addition, the novel techniques developed in this chapter can further assist in producing attribute statistics of a large flow volume. This information is very helpful for scientists to understand how the entire flow would be. Our automatic procedure is capable of analyzing and generating the flow's overall information including connected regions' number, volume, location, and segments.

Chapter 6

Segmenting and Tracking Time-Varying Vortex Ring Data

Effective feature extraction and tracking are very interesting but difficult in 3D time-varying datasets. We investigate time-evolving vortex ring dataset in this chapter for advanced extraction and tracking of individual vortices. This dataset provides an interesting evolution of flow turbulence over 70 time steps. The vortex ring is a primary structure in this flow dataset. The approach of segmenting vortices in this chapter is based on the development of segmentation algorithm for the one time step proposed in chapter 5. Since characteristics of vortex ring flow are different from those of turbulent channel flows in chapter 5, the segmentation algorithm that is initially developed for turbulent channel flows needs to be improved. We have successfully adapted the original algorithm to this dataset with only minor modification. The advanced segmentation algorithm is shown in figure 6.3 and figure 6.4 and is explained in the following sections.

6.1 Vortex Identification and Tracking

To achieve effective vortex identification and tracking, several studies specifically for our vortex ring dataset are needed for the development process. Issues of vortex ring identification, noise handling, and correspondence problems are discussed in this section.

6.1.1 Vortex Ring Identification

The vortex ring is a primary vertical structure in our experimental dataset. Special detection for this feature is necessary for effective identification of vortices existing in the data. Even though our original termination criteria developed in our variation of predictor-corrector method in chapter 5 can detect this vortex ring structure as a vortex, it requires extra time to satisfy the length criteria of the vortex core line for the termination process. In fact, the original vortex core extraction cannot complete the detection of a vortex ring and didn't identify this special structure of vortex ring. Therefore, developing approaches for vortex ring identification is required for effective and efficient feature extraction in the vortex ring data.

6.1.2 Noise Fading

Our vortex ring dataset contains many noises throughout all time steps. Noises may appear in one time step, but disappear in another time step. Most of the noises appear as small blobs. If they are rendered with salient colors and are not excluded, scientists could be easily distracted. Our algorithm fades those noises with gray color by a threshold value of features' size, which can be determined interactively. Gray blobs are less salient than other colorful features so that the scientists' attention can remain focused on the important features over time.

6.1.3 Region Correspondence

Region correspondence involves finding overlapping features in the volume. Spatial overlap of features between successive time steps implicitly determines the correspondence of those features. However, overlapping features do not necessarily represent the same features. More than one feature may overlap as shown in figure 6.1, and the decision for feature correspondence can be made with the assistance of other information such as features' attributes. When one feature overlaps with more than one other feature, it may also involve events like split and merge. In addition, when noise is considered, the event detection can become even more complex.

Spatial correspondence compares regions of features on the cell basis between the successive time steps. However, our data of each time step are acquired with different

cell sizes and positions, so additional processes for data alignment are required to correctly compare corresponding cells between different time steps.

6.1.4 Attribute Correspondence

Attribute correspondence performs feature matching according to features' attributes such as position, size, shape, and orientation. This correspondence is particularly effective when combined with region correspondence. In figure 6.1, feature A in time step t1 overlaps with feature B and feature C in time step t2, and an uncertainty of correspondence occurs for corresponding feature A to feature B or feature C. Attribute correspondence considers size of features and correlates the feature A in time step t1 to the feature B in time step t2 instead of feature C since the size of feature A is more similar to feature B.

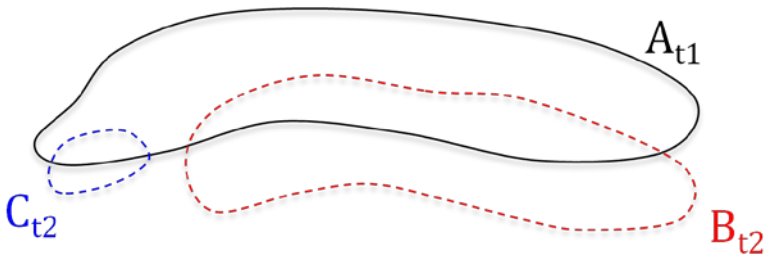

Figure 6.1: Feature A has spatial correspondence with feature B and feature C. Regarding attribute correspondence, the size of feature A is more similar to the size of feature B than to that of feature C. Therefore, the feature A in time step t1 evolves as feature B in time step t2.

6.1.5 Global Correspondence

Global correspondence determines feature correlation globally throughout all time steps rather than in only successive time steps. The researchers must have a clear understanding of the dataset with respect to the examined features in order to perform effective global determination for the features in all time steps. Our algorithm considers the initial tracking results of extracted features and verifies and determines the final segmentation for the individual vortices. Any two vortices are considered as individual vortices only when they have at some time appeared and split in a time step. In the left image of figure 6.2, features A and B are detected in time step t1. They are considered to be the same feature since they have never split in their entire lifetime. In our vortex ring dataset, this criterion provides good handling of noises since detected connected features, which may be noises, usually do not appear continously in the successive time steps and do not evolve to be separate features. Therefore, those features which never split are not considered to be distinct features. In the right image of figure 6.2, features A and B are contiguous in time step t1 but are split in time steps t2 and t3. According to the criterion of our global correspondence, these two features are distinct ones. In our vortex ring dataset, distinct individual vortices evolve to split with any others. Any two vortices that have ever split will be considered to be individual vortices and will be correctly identified.

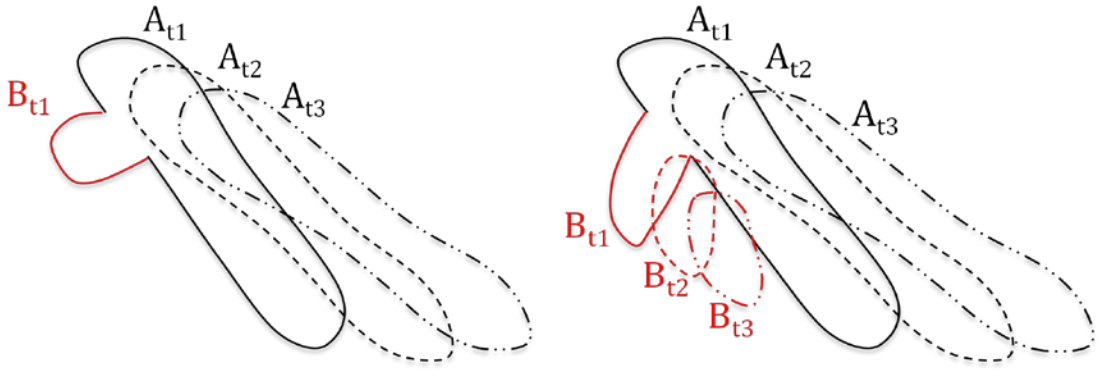

Figure 6.2: The left image shows that the contiguous features A and B are detected in time step t1. They are considered to be the same feature since a split event has never occurred. The right image shows that the features A and B are contiguous in time step t1 and separate in time steps t2 and t3. They are considered to be distinct features.

6.2 Algorithm

This section describes details of segmenting time varying vortex ring data. Explanations of the parts that are identical to stages of the algorithm in chapter 5 are omitted. Section 6.2.1 includes a flow chart for the tracking approach of two successive time steps, and section 6.2.2 includes a complete flow chart for vortex identification, tracking, and a visualization algorithm developed for vortex ring data.

6.2.1 Segment Tracking and Determination

This section explains details of the segment tracking algorithm, which is the core part (stage 13 in figure 6.4) of the entire vortex identification and tracking algorithm. The segment tracking algorithm in figure 6.3 is developed for examining coherent features

between two successive time steps and determining the evolution of these features over time. Once relationships of segments between any two successive time steps are built, we are capable of tracking each segment through times.

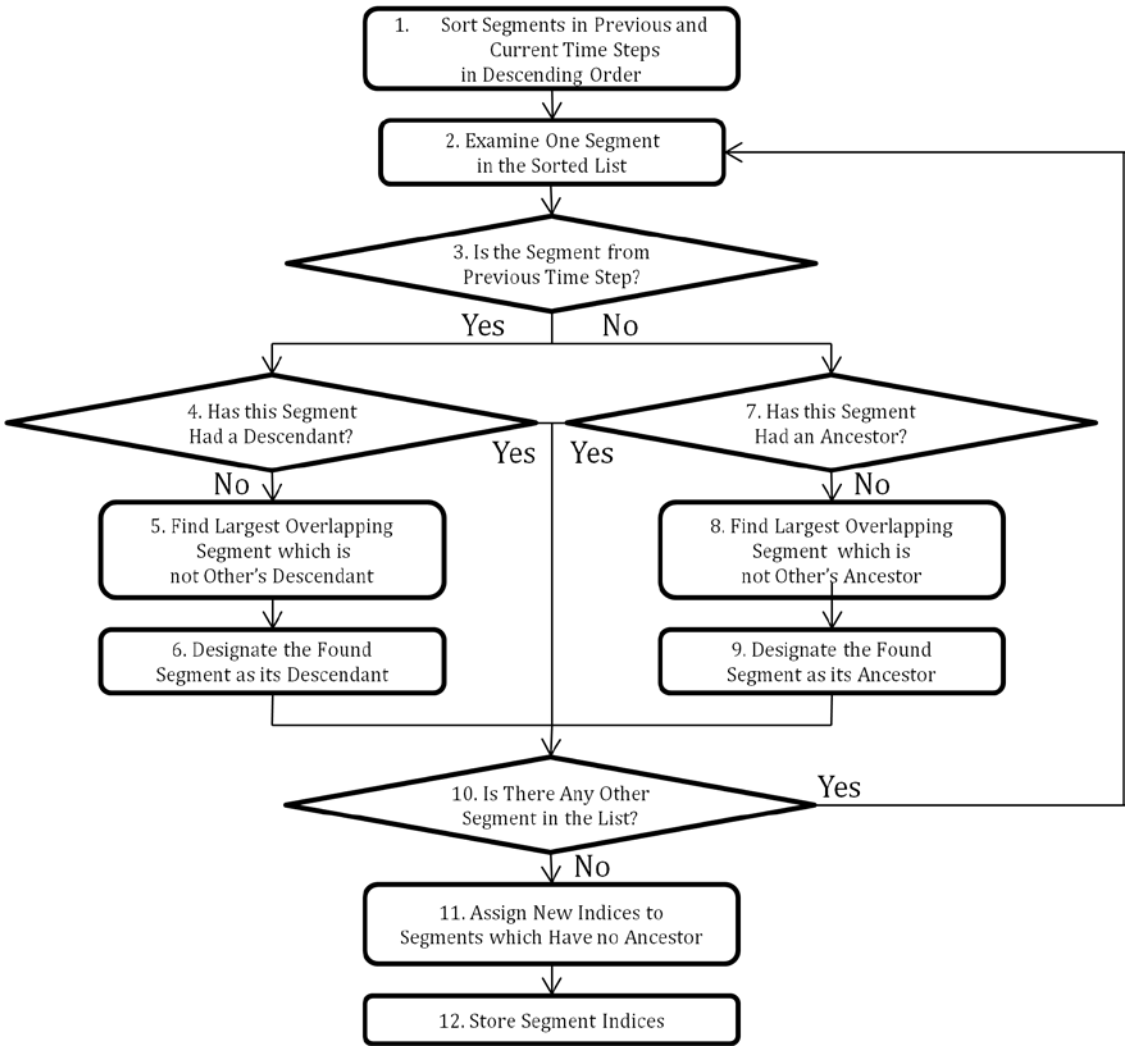

Figure 6.3: This algorithm describes a series of stages for segment tracking between successive time steps. Tracking information is maintained by each segment's index.

The correspondence scheme of our algorithm replies upon region correspondence, attribute correspondence, and global correspondence. The direct correspondence built in this algorithm for two time-steps handles region correspondence and attribute

coorespondence. This process is very important and helpful for the process of global correspondence. Figure 6.3 shows the flow chart of this algorithm, and details are also described.

1. Sort Segments in Previous and Current Time Steps in Descending Order

We sort all segments identified in previous and current time steps in descending order from large volume to small volume. A large segment typically represents a more important vortex in the flows. Small segments are likely to be less important and may be produced by noises. Therefore, the important segments are selected and processed first so as to increase the accuracy of the results and to decrease the false positive of the correspondence decision due to noises.

2. Examine One Segment in the Sorted List

This stage simply finds one unprocessed segment in the list according to the sorted order for processing in following stages.

3. Is the Segment from Previous Time Step?

If the currently processed segment is a segment in the previous time step, jump to stage 4. Otherwise, it is a segment in the current time step and jump to stage 7 accordingly.

4. Has this Segment Had a Descendant?

In this stage, we check if there is any overlapping segment in current time step which is a descendant of the processed segment. If the processed segment has had its descendant, jump to stage 10. Otherwise, proceed to stage 5.

5. Find Largest Overlapping Segment which is not other's Descendant

This stage examines the currently processed segment's overlapping segments in current time step which have not yet been corresponded to other segments as their descendants, and finds the largest one from those uncorresponded segments in current time step.

6. Designate the Found Segment as its Descendant

If the largest overlapping segment was found in previous stage, it is assigned as the currently processed segment's descendant and is considered as a same segment in two different time steps.

7. Has this Segment Had an Ancestor?

This stage is similar to stage 4. We check if there is any overlapping segment in previous time step, which is its ancestor. If the processed segment has had its ancestor, jump to stage 10. Otherwise, proceed to stage 8.

8. Find Largest Overlapping Segment which is not Other's Ancestor

This stage is similar to stage 5. We examine the currently processed segment's overlapping segments in previous time step which have not yet been corresponded

to other segments as their ancestors, and find the largest one from those uncorresponded segments in previous time step.

9. Designate the Found Segment as its Ancestor

This stage is similar to stage 6. If the largest overlapping segment is found in previous stage, it is assigned as the currently processed segment's ancestor and is considered as the same segment in two different time steps.

10. Is There Any Other Segment in the List?

If there is another unprocessed segment in the sorted list, jump to stage 2. Otherwise, proceed to stage 11.

11. Assign New Indices to Segments which Have no Ancestor

During the previous stages, some segments in current time step have found their ancestors and have been assigned with their ancestors' indices. The rest of segments that no ancestor has been found for are assigned with new indices in this stage, showing that new segments have been identified.

12. Store Segment Indices

All segments have been assigned with indices, and this information is stored in this stage.

6.2.2 Application to Time-Evolving Vortex Ring Data

This section shows an entire segmentation algorithm of time-varying vortex ring data in figure 6.4. This algorithm is an extension of the algorithm in figure 5.6 in support of multiple time step data containing different vortex topologies. Two colors, red and black, are used in the flow chart in figure 6.4. Red stages imply new stages that do not exist or are different from the stages in figure 5.6. Black stages imply the stages identical to those in figure 5.6, and details of their explanations are omitted because of duplication.

1. Identify Interesting Vortices

The interesting vortices are the areas with higher swirling strength based on a proper pre-defined threshold level, which is constant in all time steps. Instead of identifying and segmenting only one target-connected clump in step 1 of figure 5.6, all vortices in the entire volume are identified. The reason for this design is due to the requirement of capturing all the vortical evolution in the volume. Vortices are evolved over time, and they may break apart or join together. Therefore, a single individual vortex is not capable of representing characteristics of a flows' evolution, and identification of all vortices in the entire volume is required for full representation of vortex evolution.

2. Determine Candidate Sub-Vortices

(Same as step 2 in figure 5.6) One threshold level of higher swirl strength is selected to determine candidate sub-vortices.

3. Determine Seeds for Each Candidate Sub-Vortex

(Same as step 3 in figure 5.6) The grid with strongest swirling strength from each candidate sub-vortex is selected to be a seed for each candidate sub-vortex.

4. Extract Vortex Core from Each Seed

This step has to be adapted to the special topology of vortices, vortex ring, in the volume. The ring-shaped vortex is less likely to appear in our turbulent channel flows and is a primary structure, which needs to be considered here. Our stop critera should work correctly on the vortex ring when the core lines exceed the threshold length. However, this situation is not efficient and cannot recognize the feature of the vortex ring. One additional stop criterion is added here in order to detect if the grown vortex core lines have formed a circle and to improve the detection efficiency. When the grown line segment is closely aligned with previous segments in the opposite direction, the vortex line is considered to have formed a circle. The extraction of the vortex line is complete for the vortex ring and has to stop immediately.

5. Merge Sub-Vortices on Same Vortex Core

(Same as step 5 in figure 5.6)

6. Determine Segments by Sub-Vortices

(Same as step 6 in figure 5.6)

7. Store and Update Temporary Segmentation Results

(Same as step 7 in figure 5.6)

8. Examine Another Candidate Level

(Same as step 8 in figure 5.6)

9. Determine Individual Vortices by Segments of All Candidate Levels

(Same as step 9 in figure 5.6)

10. Verify Segmentation Results

This stage is designed for post verification of segmentation results. Vortex ring dataset is an experimental dataset, and there exist some noises. Noises may introduce unexpected problems and produce unwanted false positives of vortex segments. This additional stage examines and verifies the most commonly incorrect segments in which a single vortex segment is broken apart. More clearly, a segment's cells determined to be in the same group in the previous stages may not be connected well and are verified in this stage. This common failure of identified individual vortices in the current threshold level is because sub-vortices, which are considered to be in the same individual vortices, may be interfered with another segment of a noise and may not be connected to each other correctly. This stage determines if some other segment separates any individual vortex apart. If

this failure is detected, those separated individual sub-vortices and the interfering segment are regrouped. Therefore, the common failure in this case can be fixed automatically in this intuitive way.

11. Store Current Segmentation Results

Verified segments determined in the previous stage for the current time step are stored in this stage and will be processed later.

12. Examine Another Time Step

If there exists an unprocessed time step, jump to stage 1 to continue segmentation algorithm for the next time step. The mechanism of this loop is the same as the loop in figure 3.8 in chapter 3. If vortices of all time steps have been segmented, proceed to the following stages for examining and processing correspondence of identified individual vortices.

13. Track Current Segments of All Time Steps

This stage builds coherent information of segments between successive time steps. Currently stored segments are extracted from first time step to last time step, and each segment is examined by the tracking algorithm, which is similar to Silver and Wang's work [118], based on the region correspondence and attribute correspondence. The details of the tracking algorithm have been discussed in figure 6.3 by considering spatial and attribute information of each segment between two successive time steps. Distinct segments are given different indices

throughout all time steps. Segments that belong to the same vortices in different time steps keep the same indices of their ancestor or descendants.

14. Determine Final Segments of Each Time Step

This stage builds the coherence information of all segments and determines the final segments. All the current segments are identified based only on each time step data. The advanced determination for the final results of individual vortices has to consider global correspondence of segments in different time steps. Segments are examined and determined again in this stage by considering spatial relationships of any paired segments. If a pair of segments has ever split throughout all the time steps, they are considered to be distinct segments. Otherwise, they are merged to be a single segment. The determination is performed for all pairs of segments in all time steps. The final decision for the segments in each time step is updated with their corresponding indices. The false-positive segments are reduced in this stage, and tracking information for each segment in all time steps has been maintained.

15. Store Final Segmentation Results

The segments that are determined throughout the above stages in the pipelines are now considered as the final individual vortices, and the relevant segment information is stored for rendering later.

16. Determine Important Segments for Rendering

This stage determines important individual vortices according to the vortex volume. The threshold value can be predefined or determined dynamically. We set the threshold value of segment volume to be about 5 to 10 cell size. If the volume of an individual vortex is smaller than the threshold value, that vortex is rendered with a gray color. In this way, only vortices that are large enough are considered important and rendered with random colors, remaining highlighted. All other vortices are faded out with the gray color and become less salient.

17. Render Individual Vortices with Different Colors and Time Coherence

Distinct colors are randomly generated for vortices according to each segment's index so that people can track the individual vortices easily according to the colors. The individual vortices, which are categorized as important in the previous stage, are given a color according to the index number, and all other vortices are rendered with the same gray color. Any same vortex will be rendered with the same color because they have the same index. Since a vortex will maintain the same color in different time steps, evolution of vortices in time-varying flows can be observed by the eyes very easily with the coherence information of individual vortices, and the vivid random colors given to the important votices keep users' attention effectively. All the information of individual vortices can be decided and stored for reference, so the rendering process in this stage can be performed in real time and provides interactive experience for viewing the segmentation results.

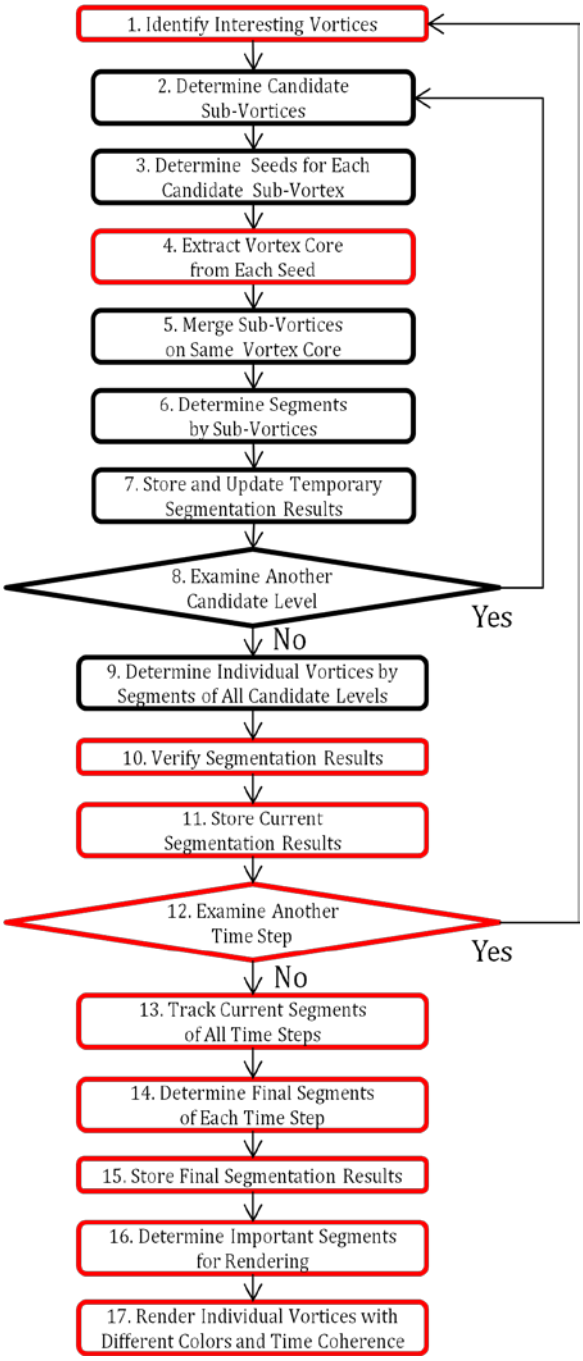

Figure 6.4: This algorithm describes a series of stages for the segmentation of individual vortices in a time-varying vortex ring.

6.3 Experimental Results

We apply our segmentation algorithm on time varying vortex ring data, which contain 70 time steps. Results of six time steps (10, 15, 20, 29, 34, and 42) are shown in figure 6.5 and figure 6.6, and these figures include the results from the front view in figure 6.5 and the side view in figure 6.6 respectively.

In figure 6.5, we are capable of both viewing the evolution of vortices in the volume clearly and of tracking individual vortices by their distinct colors. The fluids in the volume are pushed by a piston inside a vertical cylinder with the inclined exit. Therefore, the flows move from the top toward the bottom. The cylinder is rendered with its frame so that we can view flows inside. This series of images show that the circulated flows form a green vortex ring, which represents a primary vortex in the dataset, and the ring also moves toward the bottom. Two vertical vortices, the pink and brown tubes, appear from inside of the cylinder to the center of the ring and become longer when the ring moves down. This vortex ring maintains its topology until it merges with the pink tube of two vertical vortices in the time step 34 (Middle right) in figure 6.5. In the meantime, the other vertical vortex, the brown one, breaks into several pieces, and these smaller pieces are rendered with different colors. More and more small vortices appear when larger ones continue to break apart. In the results, many small vortices, which are not important or are noises, are rendered with gray colors, which may potentially draw observers' attention to other colorful vortices.

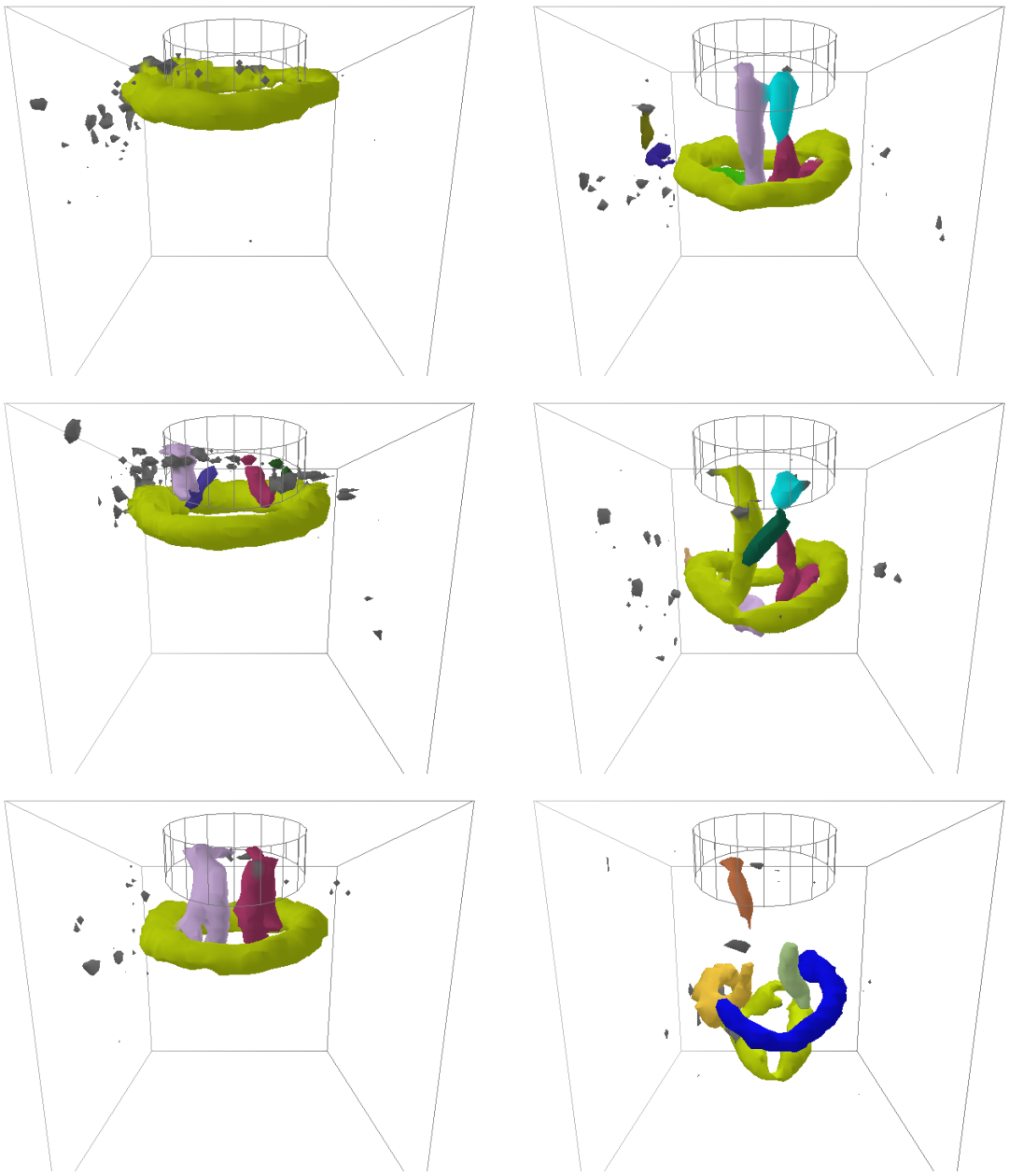

Figure 6.5: This figure shows a series of individual vortices identified inside the volume at the following time steps: 10 (Top left), 15 (Middle left), 20 (Bottom left), 29 (Top right), 34 (Middle right), and 42 (Bottom right) viewed from the front.

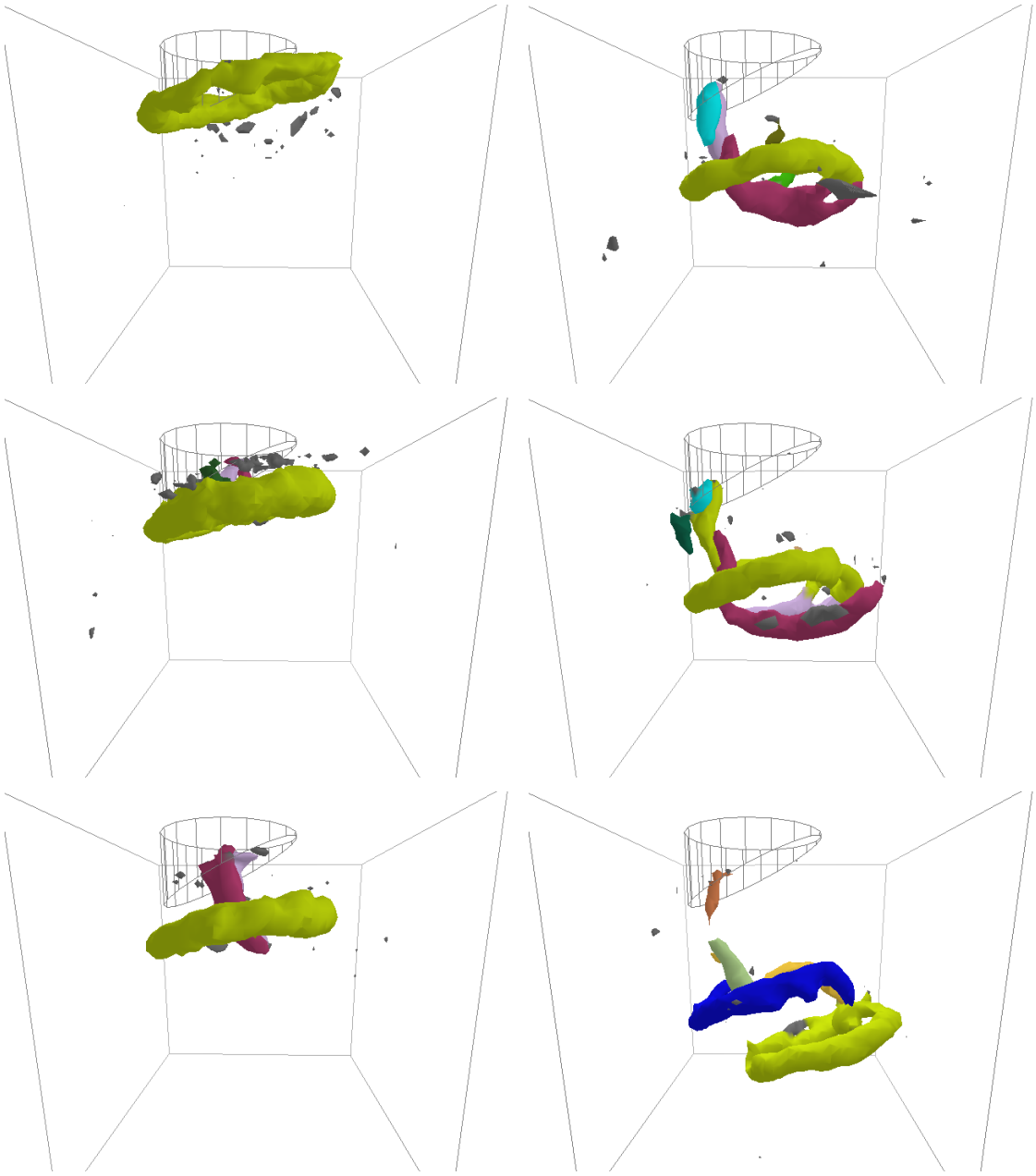

Figure 6.6: This figure shows a series of individual vortices identified inside the volume at the following time steps 10 (Top left), 15 (Middle left), 20 (Bottom left), 29 (Top right), 34 (Middle right), and 42 (Bottom right) viewed from the side.

Figure 6.6 shows exactly the same results as figure 6.5 but from the side view. These results demonstrate effective visualization of the structure tracking of vortices in the flows even though those structures are complicated and clumped together.

6.4 Discussion

Developing an effective tool for understanding the complicated time-evolving flows has been a challenging research problem. It is necessary for the tool to be able to identify characteristics in the flows correctly and to provide effective visualization of time-varying flow data. In addition, interactive or real-time visualization is also very useful and important for researchers to be capable of viewing how the flows evolve over time on the unsteady flows. The tools that are capable of extracting and examining features and their correspondence throughout all time frames can provide more powerful capability of visualizing 3D flow data.

Combining advanced feature extraction techniques with a tracking algorithm tightly provides an effective way of visualizing time-varying vortex ring data. The preliminary coherence of segments between any two successive time steps can be verified and processed in order to build global correspondence of the features for advanced determination of segmentation. Our experimental results have shown that the applications are successfully applied with the algorithm for the tasks of identifying, segmenting, processing, and tracking individual vortices.

All the time consuming tasks of the stages from stage 1 to 16 in figure 6.4 can be completed in advance in order to produce off-line data for interactive rendering. The interactive capability or the pre-rendered animation can be achieved to demonstrate the success of our useful and powerful applications in time-varying vortex ring data.

Chapter 7

Conclusion and Future Work

This dissertation proposed a variety of techniques which aim at an ultimate goal of developing an improved understanding of characteristics in 3D time-evolving flows. In order to achieve this goal, a series of problems have been raised and investigated, and appropriate solutions have been developed successively and explained in clear flow charts of algorithms. The challenge of 3D turbulent flow visualization is the lack of robust mathematical definition of physical characteristics in a flow and is also due to the intrinsic issues of 3D flow visualization such as occlusion.

We have developed many techniques in this dissertation for the problems involving muti-variate visualization as well as feature extraction, analysis, and tracking. Our multi-variate visualization techniques include multiple schemes to help researchers investigate different measures and their potential features in order to understand 3D flows. With the enhanced understanding of flow fields, the advanced techniques are further developed.

Two techniques have been developed in this dissertation for the task of vortex segmentation. Our first segmentation algorithm is based on the characteristics of multiple rotation vectors. The development of this approach relies upon underlying study about the relationships of various variables relating to turbulence. The approach requires a pre-defined threshold for angle quantity. However, the drawback of this algorithm is its sensitivity to the selection of the threshold, which might be improved by furhter analysis of these quantities.

Our second technique of segmenting individual vortices is proposed to be applied more robustly to the 3D turbulent channel flows. This approach is extended to the time-evolving vortex ring flow as well. Our approaches have shown the flexibility, effectiveness, and robustness of applications on different flow data, and our results have demonstrated the successful applications of identifying, segmenting, and tracking time varying vortex ring flows. The algorithm for rendering a time-evolving vortex ring dataset can provide the renderer interactive capability by computing time-consuming 3D flow features offline and leaving light computation of rendering real-time. In addition, all these techniques can be applied to the entire flow by an automatic procedure, and statistics of features in the flow can be obtained for scientists to analyze the entire flow data efficiently.

Our series of solutions are capable of assisting researchers in better understanding the complicated features in 3D flows through different approaches and visualizing the dynamically-evolving features in the flows successfully. However, some tasks of our algorithms in muti-variate visualization, hierarchical vortex region identification, and

time-varying vortex ring visualization are time-consuming, so intermediate data can be computed in advance or in parallel for providing real-time rendering or animation, which can be improved in the future.

Our tools in this dissertation provide global visualization of local quantities and global analysis of the vertical structure like individual vortices on turbulent flows. However, many other potential structures in the flows have not been understood, and a specific type of vortical structure such as hairpin [2, 3] has yet to be discussed. Combining our segmentation techniques with structure detection algorithms has potential for finding coherently organized hairpin vortices [3]. Thus, the capability of our visualization can be enhanced with such advanced investigation inside the flows [85, 87]. Other problems that have not been investigated in this dissertation include the evaluation of segments' accuracy, the robustness of our methods on different types of flow data, and the correspondence reconstruction for aggregation on vortices that have broken apart. These research areas are left for future work.

Bibliography

[1] J. C. d. Álamo, *et al.*, "Scaling of the Energy Spectra of Turbulent Channels," *J. Fluid Mech.*, vol. 500, pp. 135-144, 2004.

[2] J. Zhou, "Self-Sustaining Formation of Packets of Hairpin Vortices in a Turbulent Wall Layer," Ph.D. dissertation, University of Illinois, 1997.

[3] J. Zhou, *et al.*, "Mechanisms for Generating Coherent Packets of Hairpin Vortices in Channel Flow," *J. Fluid Mech.*, vol. 387, pp. 353-396, 1999.

[4] R. Himeno and K. Fujitani, "Numerical Analysis and Visualization of Flow in Automobile Aerodynamics Development," *J. Wind Eng. and Ind. Aerodynamics*, vol. 46-47, pp. 785-790, 1993.

[5] A. Jameson, "Computational Aerodynamics for Aircraft Design," *Science*, vol. 245, pp. 361-371, 1989.

[6] E. R. Hawkes, *et al.*, "Direct Numerical Simulation of Turbulent Combustion: Fundamental Insights Towards Predictive Models," *J. Phy.: Conf. Ser.*, vol. 16, pp. 65-79, 2005.

[7] G. Sridhar and J. Katz, "Drag and Lift Forces on Microscopic Bubbles Entrained by a Vortex," *Phys. Fluids*, vol. 7, pp. 389-399, 1995.

[8] R. S. Laramee, *et al.*, "The State of the Art in Flow Visualization: Dense and Texture-Based Techniques," *Comput. Graph. Forum*, vol. 23, pp. 203-221, 2004.

[9] R. V. Klassen and S. J. Harrington, "Shadowed Hedgehogs: A Technique for Visualizing 2D Slices of 3D Vector Fields," *Proc. IEEE Visualization '91*, pp. 148-153, 1991.

[10] D. S. Ebert, *et al.*, "Volume Rendering Methods for Computational Fluid Dynamics Visualization," *Proc. IEEE Visualization '94*, pp. 232-239, 1994.

[11] E. Boring and A. Pang, "Directional Flow Visualization of Vector Fields," *Proc. IEEE Visualization '96*, pp. 389-392, 1996.

[12] W. C. d. Leeuw and J. J. v. Wijk, "A Probe for Local Flow Field Visualization," *Proc. IEEE Visualization '93*, pp. 39-45, 1993.

[13] J. J. v. Wijk, "Spot Noise - Texture Synthesis for Data Visualization," *Proc. SIGGRAPH '91*, vol. 25, pp. 309-318, 1991.

[14] W. C. d. Leeuw and J. J. v. Wijk, "Enhanced Spot Noise for Vector Field Visualization," *Proc. IEEE Visualization '95*, p. IEEE Visualization '95, 1995.

[15] A. Telea and J. J. v. Wijk, "Simplified Representation of Vector Fields," *Proc. IEEE Visualization '99*, pp. 35-42, 1999.

[16] B. Cabral and L. C. Leedom, "Imaging Vector Fields Using Line Integral Convolution," *Comput. Graph. Proc., Annu. Conference Series*, pp. 263-269, 1993.

[17] W. C. d. Leeuw and R. v. Liere, "Comparing LIC and Spot Noise," *Proc. IEEE Visualization '98*, pp. 359-365, 1998.

[18] L. K. Forssell and S. D. Cohen, "Using Line Integral Convolution for Flow Visualization: Curvilinear Grids, Variable-Speed Animation, and Unsteady Flows," *IEEE Trans. Vis. and Comput. Graphics*, vol. 1, pp. 133-141, 1995.

[19] V. Verma, *et al.*, "PLIC: Bridging the Gap between Streamlines and LIC," *Proc. IEEE Visualization '99*, pp. 341-348, 1999.

[20] A. Okada and D. Kao, "Enhanced Line Integral Convolution with Flow Feature Detection," *Proc. IS&T/SPIE Electron. Imaging '97*, pp. 206-217, 1997.

[21] R. Wegenkittl, *et al.*, "Animating Flow Fields: Rendering of Oriented Line Integral Convolution," in *Comput. Animation '97*, 1997, pp. 15-21.

[22] R. Wegenkittl and E. Groller, "Fast Oriented Line Integral Convolution for Vector Field Visualization via the Internet," *Proc. IEEE Visualization '97*, pp. 309-316, 1997.

[23] M.-H. Kiu and D. C. Banks, "Multi-Frequency Noise for LIC," *Proc. IEEE Visualization '96*, pp. 121-126, 1996.

[24] U. Bordoloi and H.-W. Shen, "Hardware Accelerated Interactive Vector Field Visualization: A Level of Detail Approach," in *Eurographics '02*, 2002, pp. 605-614.

[25] W. Heidrich, *et al.*, "Applications of Pixel Textures in Visualization and Realistic Image Synthesis," in *ACM Symp. on Interactive 3D Graph.*, 1999, pp. 127-134.

[26] D. Stalling and H.-C. Hege, "Fast and Resolution Independent Line Integral Convolution," *Proc. SIGGRAPH '95*, pp. 249-256, 1995.

[27] M. Zockler, *et al.*, "Parallel Line Integral Convolution," in *Proc. Eurographics Workshop on Parallel Graph. and Visualization*, 1996, pp. 111-127.

[28] G. Turk and D. Banks, "Image-Guided Streamline Placement," *Proc. SIGGRAPH '96*, pp. 453-460, 1996.

[29] B. Jobard and W. Lefer, "Creating Evenly-Spaced Streamlines of Arbitrary Density," in *Proc. Eurographics Workshop on Visualization in Scientific Computing*, 1997, pp. 45-55.

[30] B. Jobard and W. Lefer, "Multiresolution Flow Visualization," in *WSCG '01 Conference Proc.*, 2001, pp. 34-37.

[31] I. A. Sadarjoen, *et al.*, "Selective Visualization of Vortices in Hydrodynamic Flows," *Proc. IEEE Visualization '98*, pp. 419-422, 1998.

[32] A. Helgeland and O. Andreassen, "Visualization of Vector Fields Using Seed LIC and Volume Rendering," *IEEE Trans. Vis. and Comput. Graphics*, vol. 10, pp. 673-682, 2004.

[33] C. Rezk-Salama, *et al.*, "Interactive Exploration of Volume Line Integral Convolution Based on 3D-Texture Mapping," *Proc. IEEE Visualization '99*, pp. 233-240, 1999.

[34] V. Interrante, "Illustrating Surface Shape in Volume Data via Principal Direction-Driven 3D Line Integral Convolution," *Proc. SIGGRAPH '97*, pp. 109-116, 1997.

[35] V. Interrante and C. Grosch, "Strategies for Effectively Visualizing 3D Flow with Volume LIC," *IEEE VIsualization '97*, pp. 421-424, 1997.

[36] V. Interrante and C. Grosch, "Visualizing 3D Flow," *IEEE Comput. Graph. and Applicat.*, vol. 18, pp. 49-53, 1998.
[37] H. Loffelmann and E. Groller, "Enhancing the Visualization of Characteristic Structures in Dynamical Systems," in *Proc. Eurographics Workshop on Visualization in Scientific Computing*, 1998, pp. 59-68.
[38] A. Fuhrmann and E. Groller, "Real-Time Techniques for 3D Flow Visualization," *Proc. IEEE Visualization '98*, pp. 305-312, 1998.
[39] M. Zockler, *et al.*, "Interactive Visualization of 3D-Vector Fields Using Illuminated Stream Lines," *Proc. IEEE Visualization '96*, pp. 107-113, 1996.
[40] C. Teitzel and T. Ertl, "New Approaches for Particle Tracing on Sparse Grids," in *EG/IEEE TCVG Symp. on Visualization '99*, 1999, pp. 73-84.
[41] S.-K. Ueng, *et al.*, "Efficient Streamline, Streamribbon, and Streamtube Constructions on Unstructured Grids," *IEEE Trans. Vis. and Comput. Graphics*, vol. 2, pp. 100-110, 1996.
[42] W. J. Schroeder, *et al.*, "The Stream Polygon: A Technique for 3D Vector Field Visualization," *Proc. IEEE Visualization '91*, pp. 126-132, 1991.
[43] M. Brill, *et al.*, "Streamball Techniques for Flow Visualization," *Proc. IEEE Visualization '94*, pp. 225-231, 1994.
[44] J. J. v. Wijk, "Implicit Stream Surfaces," *Proc. IEEE Visualization '93*, pp. 245-252, 1993.
[45] W. Cai and P.-A. Heng, "Principal Stream Surfaces," *Proc. IEEE Visualization '97*, pp. 75-80, 1997.
[46] J. J. v. Wijk, "Flow Visualization with Surface Particles," *IEEE Comput. Graph. and Applicat.*, vol. 13, pp. 18-24, 1993.
[47] A. Appel, *et al.*, "The Haloed Line Effect for Hidden Line Elimination," *Proc. SIGGRAPH '79*, pp. 151-157, 1979.
[48] M. Zockler and H.-C. Hege, "Fast Display of Illuminated Field Lines," *IEEE Trans. Vis. and Comput. Graphics*, vol. 3, pp. 118-128, 1997.
[49] X. Ye, *et al.*, "Strategy for Seeding 3D Streamlines," *Proc. IEEE Visualization '05*, pp. 471-478, 2005.
[50] X. Mao, *et al.*, "Image-Guided Streamline Placement on Curvilinear Grid Surfaces," *Proc. IEEE Visualization '98*, pp. 135-142, 1998.
[51] C. Teitzel, *et al.*, "Efficient and Reliable Integration Methods for Particle Tracing in Unsteady Flows on Discrete Meshes," in *Proc. Eurographics Workshop on Visualization in Scientific Computing*, 1997, pp. 31-41.
[52] R. S. Laramee, *et al.*, "Investigating Swirl and Tumble Flow with a Comparison of Visualization Techniques," *Proc. IEEE Visualization '05*, pp. 51-58, 2005.
[53] F. H. Post, *et al.*, "The State of the Art in Flow Visualization: Feature Extraction and Tracking," *Comput. Graph. Forum*, pp. 775-792, 2003.
[54] J. Sahner, *et al.*, "Galilean Invariant Extraction and Iconic Representation of Vortex Core Lines," *Proc. Eurographics / IEEE VGTC Symp. on Visualization*, pp. 151-160, 2005.
[55] P. A. Durbin and G. Medic, *Fluid Dynamics with a Computational Perspective*: Cambridge: Cambridge Univ. Press, 2007.

[56] W. R. Debler, *Fluid Mechanics Fundamentals*, 1990.
[57] J. A. Fay, *Introduction to Fluid Mechanics*: MA: MIT Press, 1994.
[58] C. Pozrikidis, *Introduction to Theoretical and Computational Fluid Dynamics*: Oxford Univ. Press, 1997.
[59] J. F. Douglas, *et al.*, *Fluid Mechanics*, 3rd ed., 1995.
[60] C. H. Berdahl and D. S. Thompson, "Education of Swirling Structure Using the Velocity Gradient Tensor," *AIAA J.*, vol. 28, pp. 1347-1352, 1990.
[61] R. J. Adrian, *et al.*, "Analysis and Interpretation of Instantaneous Turbulent Velocity Fields," *Experiments in Fluids*, vol. 29, pp. 275-290, 2000.
[62] R. J. Adrian, "Particle-Imaging Techniques for Experimental Fluid Mechanics," *Annu. Review of Fluid Mechanics*, vol. 23, pp. 261-304, 1991.
[63] R. J. Adrian, "Twenty Years of Particle Image Velocimetry," *Experiments in Fluids*, vol. 39, pp. 159-169, 2005.
[64] A. K. Prasad, "Stereoscopic Particle Image Velocimetry," *Experiments in Fluids*, vol. 29, pp. 103-116, 2000.
[65] S. M. Soloff, *et al.*, "Distortion Compensation for Generalized Stereoscopic Particle Image Velocimetry," *Meas. Sci. Technol.*, vol. 8, pp. 1441-1454, 1997.
[66] M. P. Arroyo and C. A. Greated, "Stereoscopic Particle Image Velocimetry," *Meas. Sci. Technol.*, vol. 2, pp. 1181-1186, 1991.
[67] B. Ganapathisubramani, *et al.*, "Dual-Plane PIV Technique to Determine the Complete Velocity Gradient Tensor in a Turbulent Boundary Layer," *Experiments in Fluids*, vol. 39, pp. 222-231, 2005.
[68] F. R. Hama, *et al.*, "On Transition from Laminar to Turbulent Flow," *J. Appl. Phys.*, vol. 28, 1956.
[69] S. J. Kline and P. W. Runstadler, "Some Preliminary Results of Visual Studies of the Flow Model of the Wall Layers of the Turbulent Boundary Layers," *Trans. ASME*, vol. 2, 1959.
[70] E. R. Corino and R. S. Brodkey, "A Visual Investigation of the Wall Region in Turbulent Flow," *J. Fluid Mech.*, vol. 37, pp. 1-30, 1969.
[71] S. J. Kline, *et al.*, "The Structure of Turbulent Boundary Layers," *J. Fluid Mech.*, vol. 30, pp. 741-773, 1967.
[72] B. J. Cantwell, "Organized Motion in Turbulent Flow," *Annu. Rev. Fluid Mech.*, vol. 13, pp. 457-515, 1981.
[73] S. K. Robinson, "Coherent Motions in Turbulent Boundary Layers," *Ann. Rev. Fluid Mech.*, vol. 23, pp. 601-639, 1991.
[74] R. L. Panton, "Overview of the Self-Sustaining Mechanisms of Wall Turbulence," *Prog. Aerospace Sci.*, vol. 37, pp. 341-383, 2001.
[75] J. Jeong, *et al.*, "Coherent Structures Near the Wall in a Turbulent Channel Flow," *J. Fluid Mech.*, vol. 332, pp. 185-214, 1997.
[76] D. K. Heist, *et al.*, "Observations of the Formation of Streamwise Vortices by Rotation of Arch Vortices," *Phys. Fluids*, vol. 12, pp. 2965-2975, 2000.
[77] T. Theodorsen, "Mechanism of Turbulence," in *Proc. 2nd Midwestern Conf. Fluid Mech.*, Ohio State University, Columbus, Ohio, 1952.

[78] M. R. Head and P. Bandyopadhyay, "New Aspects of Turbulent Boundary Layer Structure," *J. Fluid Mech.*, vol. 107, pp. 297-338, 1981.
[79] A. E. Perry and M. S. Chong, "On the Mechanism of Wall Turbulence," *J. Fluid Mech.*, vol. 119, pp. 173-217, 1982.
[80] A. A. Townsend, *The Structure of Turbulent Shear Flow*, 2nd ed.: Cambridge University Press, 1976.
[81] A. E. Perry and I. Marusic, "A Wall-Wake Model for the Turbulence Structure of Boundary Layers," *J. Fluid Mech.*, vol. 298, pp. 361-388, 1995.
[82] R. J. Adrian, *et al.*, "Vortex Organization in the Outer Region of the Turbulent Boundary Layer," *J. Fluid Mech.*, vol. 422, pp. 1-53, 2000.
[83] C. D. Tomkins and R. J. Adrian, "Spanwise Structure and Scale Growth in Turbulent Boundary Layers," *J. Fluid Mech.*, vol. 490, pp. 37-74, 2003.
[84] R. J. Adrian and Z. C. Liu, "Observation of Vortex Packets in Direct Numerical Simulation of Fully Turbulent Channel Flow," *J. Visualization*, vol. 5, pp. 9-19, 1991.
[85] K. T. Christensen and R. J. Adrian, "Statistical Evidence of Hairpin Vortex Packets in Wall Turbulence," *J. Fluid Mech.*, vol. 431, pp. 433-443, 2001.
[86] I. Marusic, "On the Role of Large Scale Structures in Wall Turbulence," *Phys. Fluids*, vol. 13, pp. 735-743, 2001.
[87] B. Ganapathisubramani, *et al.*, "Characteristics of Vortex Packets in Turbulent Boundary Layers," *J. Fluid Mech.*, vol. 478, pp. 35-46, 2003.
[88] J. Jimenez, "Turbulent Flows over Rough Walls," *Ann. Rev. Fluid Mech.*, vol. 36, pp. 173-196, 2004.
[89] M. P. Schultz and K. A. Flack, "The Rough-Wall Turbulent Boundary Layer from the Hydraulically Smooth to the Fully Rough Regime," *J. Fluid Mech.*, vol. 580, pp. 381-405, 2007.
[90] Y. Wu and K. T. Christensen, "Outer-Layer Similarity in the Presence of a Practical Rough Wall Topography," *Phys. of Fluids*, vol. 19, 2007.
[91] O. Flores, *et al.*, "Vorticity Organization in the Outer Layer of Turbulent Channels with Disturbed Walls," *J. Fluid Mech.*, vol. 591, pp. 145-154, 2007.
[92] O. Coceal, *et al.*, "Structure of Turbulent Flow over Regular Arrays of Cubical Roughness," *J. Fluid Mech.*, vol. 589, pp. 375-409, 2007.
[93] B. McCormick, *et al.*, "Visualization in Scientific Computing," *Comput. Graph.*, vol. 21, 1987.
[94] M. Jiang, *et al.*, "Detection and Visualization of Vortices," in *Visualization Handbook*, C. Johnson and C. Hansen, Eds., 1 ed: Academic Press, 2004.
[95] M. Roth, "Automatic Extraction of Vortex Core Lines and Other Line-Type Features for Scientific Visualization," Ph.D. dissertation, Swiss Federal Institute of Technology Zurich, 2000.
[96] M. Jiang, *et al.*, "Geometric Verification of Swirling Features in Flow Fields," *Proc. IEEE Visualization '02*, 2002.
[97] J. Jeong and F. Hussain, "On the Identification of a Vortex," *J. Fluid Mech.*, vol. 285, pp. 69-94, 1995.

[98] J. C. R. Hunt, *et al.*, "Eddies, Streams and Convergence Zones in Turbulent Flows," *Proc. 1988 Summer Program of the Center for Turbulence Research*, pp. 198-208, 1988.
[99] M. S. Chong, *et al.*, "A General Classification of Three-Dimensional Flow Fields," *Phys. Fluids*, vol. 2, pp. 765-777, 1990.
[100] P. Chakraborty, *et al.*, "On the Relationships between Local Vortex Identification Schemes," *J. Fluid Mech.*, vol. 535, pp. 189-214, 2005.
[101] D. Bauer and R. Peikert, "Vortex Tracking in Scale-Space," *Proc. Symp. on Data Visualization 2002*, pp. 233-240, 2002.
[102] D. Kenwright and R. Haimes, "Automatic Vortex Core Detection," *IEEE Comput. Graph. and Applicat.*, vol. 18, pp. 70-74, 1998.
[103] J. Sahner, *et al.*, "Vortex and Strain Skeletons in Eulerian and Lagrangian Frames," *IEEE Trans. Vis. and Comput. Graphics*, vol. 13, pp. 980-990, 2007.
[104] S. Stegmaier, *et al.*, "Opening the Can of Worms: an Exploration Tool for Vortical Flows," *Proc. IEEE Visualization '05*, pp. 463-470, 2005.
[105] M. Jankun-Kelly, *et al.*, "Vortex Visualization for Practical Engineering Applications," *IEEE Trans. Vis. and Comput. Graphics*, vol. 12, pp. 957-964, 2006.
[106] D. C. Banks and B. A. Singer, "A Predictor-Corrector Technique for Visualizing Unsteady Flow," *IEEE Trans. Vis. and Comput. Graphics*, vol. 1, pp. 151-163, 1995.
[107] D. Sujudi and R. Haimes, "Identification of Swirling Flow in 3D Vector Fields," *AIAA Paper 95-1715*, 1995.
[108] M. Jiang, *et al.*, "A Novel Approach to Vortex Core Region Detection," *Proc. Symp. on Data Visualization 2002*, pp. 217-225, 2002.
[109] M. Roth and R. Peikert, "A Higher-Order Method for Finding Vortex Core Lines," *Proc. IEEE Visualization '98*, pp. 143-150, 1998.
[110] M. Jankun-Kelly, *et al.*, "A Multistage Vortex Visualization Method," *44th AIAA Aerospace Sciences Meeting and Exhibit*, 2006.
[111] G. Haller, "An Objective Definition of a Vortex," *J. Fluid Mech.*, vol. 525, pp. 1-26, 2005.
[112] F. Sadlo and R. Peikert, "Efficient Visualization of Lagrangian Coherent Structures by Filtered AMR Ridge Extraction," *IEEE Trans. Vis. and Comput. Graphics*, vol. 13, pp. 1456-1463, 2007.
[113] R. Fuchs, *et al.*, "Parallel Vectors Criteria for Unsteady Flow Vortices," *IEEE Trans. Vis. and Comput. Graphics*, vol. 14, pp. 615-626, 2008.
[114] D. R. Troolin and E. K. Longmire, "Volumetric Velocity Measurements of Vortex Rings from Inclined Exits," *Experiments in Fluids*, 2009.
[115] C. Montani, *et al.*, "Discretized Marching Cubes," *IEEE Visualization '94*, pp. 281 - 287, 1994.
[116] A. Sanna, *et al.*, "Visualizing Vector Fields: the Thick Oriented Stream-Line Algorithm (TOSL)," *Computers and Graphics*, vol. 25, pp. 847-855, 2001.
[117] P. Hall, "Volume Rendering of Vector Fields," *The Visual Compu.*, vol. 10, pp. 69-78, 1993.

[118] D. Silver and X. Wang, "Tracking and Visualizing Turbulent 3D Features," *IEEE Trans. Vis. and Comput. Graphics*, vol. 3, pp. 129-141, 1997.

Appendix

We begin by stating some well-known facts from linear algebra. Thinking of a vector $\bar{v}$ as a 3×1 matrix and its transpose $\bar{v}^T$ as a 1×3 matrix, the following can easily be proved:

Lemma 1.

A. $\bar{v}^{\mathrm{T}}\bar{v} = |\bar{v}|^2$.

B. $\bar{v}^{\mathrm{T}}\bar{w} = \bar{w}^{\mathrm{T}}\bar{v} = \bar{v} \circ \bar{w}$.

C. $\bar{u} \circ (\bar{v} \times \bar{w}) = \bar{v} \circ (\bar{w} \times \bar{u}) = \bar{w} \circ (\bar{u} \times \bar{v})$.

D. $\bar{v} \circ (\bar{w} \times \bar{v}) = 0$.

More interesting is the following result.

Lemma 2. *Let* $\bar{s} = \begin{pmatrix} s_1 \\ s_2 \\ s_3 \end{pmatrix}, \bar{t} = \begin{pmatrix} t_1 \\ t_2 \\ t_3 \end{pmatrix}$ *and* $\bar{y} = \begin{pmatrix} u \\ v \\ w \end{pmatrix}$. *Then*

$$\bar{t}^T \begin{pmatrix} 0 & w & -v \\ -w & 0 & u \\ v & -u & 0 \end{pmatrix} \bar{s} = \bar{y} \circ (\bar{t} \times \bar{s}).$$

Proof.

$$\bar{t}^T \begin{pmatrix} 0 & w & -v \\ -w & 0 & u \\ v & -u & 0 \end{pmatrix} \bar{s} = t_3(-s_2u + s_1v) + t_2(s_3u - s_1w) + t_1(-s_3v + s_2w)$$

$$= u(s_3t_2 - s_2t_3) - v(s_3t_1 + s_1t_3) + w(s_2t_1 - s_1t_2) = \bar{y} \circ (\bar{t} \times \bar{s}).$$

We apply these results using equations (15) and (16) in Chapter 4. Multiplying both side of (15) by $\bar{t}^T$ and both side of (16) by $\bar{s}^T$ we obtain

$$\bar{t}^T A \bar{s} = a\bar{t}^T \bar{s} - b\bar{t}^T \bar{t}$$

$$\bar{s}^T A\bar{t} = b\bar{s}^T\bar{s} + a\bar{s}^T\bar{t}$$

Subtracting the first equation from the second we obtain

$$\bar{s}^T A\bar{t} - \bar{t}^T A\bar{s} = b(|\bar{s}|^2 + |\bar{t}|^2). \qquad (17)$$

Using Lemma 1B, we rewrite $\bar{s}^T A\bar{t}$ as $\bar{t}^T A^T\bar{s}$. Hence the left side of (17) becomes

$$\bar{t}^T(A^T - A)\bar{s} = \bar{t}\begin{pmatrix} 0 & Q_x - P_y & R_x - P_z \\ P_y - Q_x & 0 & R_y - Q_z \\ P_z - R_x & Q_z - R_y & 0 \end{pmatrix}\bar{s}.$$

But this is precisely the left hand side of the equation in Lemma 2 with $\bar{y} = \bar{c}$. We summarize this as

Theorem 1. *Suppose* $\lambda_1 = a + bi$ *and* $\lambda_2 = a - bi$ *with* $b > 0$ *are the complex eigenvalues and* $\bar{v}_1 = \bar{s} + \bar{t}i$ *and* $\bar{v}_2 = \bar{s} - \bar{t}i$ *with* $|\bar{s}|^2 + |\bar{t}|^2 = 1$ *are the associated eigenvectors of the Jacobian* ∇V *of a velocity vector field V. Then* $\bar{c} \circ \bar{n} = \bar{c} \circ (\bar{t} \times \bar{s}) = b(|\bar{s}|^2 + |\bar{t}|^2) = b$. *so that the angle* θ *between* $\bar{c}$ *and* $\bar{n}$ *is given by*

$$\cos\theta = \frac{b}{|\bar{c}||\bar{t} \times \bar{s}|}$$

Finding the angle between $\bar{c}$ and $\bar{r}$ is a bit more complicated. First we note that $A\bar{r} = \lambda\bar{r}$ implies:

$$\bar{s}^T A\bar{r} = \lambda(\bar{s}^T\bar{r})$$

$$\bar{t}^T A\bar{r} = \lambda(\bar{t}^T\bar{r}) \qquad (18)$$

Also from equations (15) and (16) we can write:

$$\bar{s}^T A^T \bar{r} = \bar{r}^T A \bar{s} = a\bar{r}^T \bar{s} - b\bar{r}^T \bar{t}$$

$$\bar{t}^T A^T \bar{r} = \bar{r}^T A \bar{t} = b\bar{r}^T \bar{s} + a\bar{r}^T \bar{t} \qquad (19)$$

Subtracting the equations in (18) from those in (19) we get

$$\bar{s}^T (A^T - A)\bar{r} = (a - \lambda)\bar{s}^T \bar{r} - b\bar{t}^T \bar{r}$$

$$\bar{t}^T (A^T - A)\bar{r} = b\bar{s}^T \bar{r} + (a - \lambda)\bar{t}^T \bar{r}$$

Using Theorem 1 together with Lemma 1C and Lemma 1D we obtain

$$\bar{s} \circ (\bar{r} \times \bar{c}) = (a - \lambda)\bar{s}^T \bar{r} - b\bar{t}^T \bar{r}$$

$$\bar{t} \circ (\bar{r} \times \bar{c}) = b\bar{s}^T \bar{r} + (a - \lambda)\bar{t}^T \bar{r}$$

$$\bar{r} \circ (\bar{r} \times \bar{c}) = 0 \qquad (20)$$

If we let

$$B = \begin{pmatrix} s_1 & s_2 & s_3 \\ t_1 & t_2 & t_3 \\ r_1 & r_2 & r_3 \end{pmatrix}$$

$$\bar{x} = \bar{r} \times \bar{c}$$

$$\bar{w} = \begin{pmatrix} (a - \lambda)\bar{s}^T \bar{r} - b\bar{t}^T \bar{r} \\ b\bar{s}^T \bar{r} + (a - \lambda)\bar{t}^T \bar{r} \\ 0 \end{pmatrix} \qquad (21)$$

We can rewrite equations (20) as

$$B\bar{x} = \bar{w}.$$

Hence $\bar{r} \times \bar{c} = B^{-1}\bar{w}$. Then the angle θ between $\bar{r}$ and $\bar{c}$ can be found using $|\bar{r} \times \bar{c}| = |\bar{r}||\bar{c}| \sin\theta$. We summarize this as

Theorem 2. *If B and $\bar{w}$ are as defined in equation (21) then*

$$\bar{r} \times \bar{c} = B^{-1}\bar{w}.$$

We can now prove Theorem 3 which we separate into three parts.

Theorem 3.1. *If $\bar{r}$ and $\bar{n}$ have the same direction, then $\bar{c}$ is also in this direction.*

Proof. Suppose $\bar{r}$ and $\bar{n}$ have the same direction. Then $\bar{r}$ is in the same direction as $\bar{n} = \bar{t} \times \bar{s}$ and hence $\bar{r}$ is perpendicular to both $\bar{s}$ and $\bar{t}$. Then $\bar{w}$ in Theorem 3 is the 0 vector and so $\bar{r} \times \bar{c} = \bar{0}$. But $\bar{r} \times \bar{c} = \bar{0}$ only if $\bar{r}$ and $\bar{c}$ are in the same direction.

Theorem 3.2. *If $\bar{r}$ and $\bar{c}$ have the same direction, then $\bar{n}$ is also in this direction.*

Proof. If $\bar{r}$ and $\bar{c}$ have the same direction, then $\bar{r} \times \bar{c} = \bar{0}$, so by Theorem 3, $B^{-1}\bar{w} = \bar{0}$. Hence $\bar{w} = B\bar{0} = \bar{0}$. But using the definition of $\bar{w}$ in (21) we can then write

$$\begin{pmatrix} a-\lambda & -b \\ b & a-\lambda \end{pmatrix} \begin{pmatrix} \bar{s}^T\bar{r} \\ \bar{t}^T\bar{r} \end{pmatrix} = \begin{pmatrix} 0 \\ 0 \end{pmatrix}$$

The determinant of this matrix is $(a-\lambda)^2 + b^2 \neq 0$, so it is invertible and hence both $\bar{s}^T\bar{r} = 0$ and $\bar{t}^T\bar{r} = 0$. But this means that $\bar{r}$ is perpendicular to both $\bar{s}$ and $\bar{t}$ and hence $\bar{r}$ is in the same direction as $\bar{n} = \bar{t} \times \bar{s}$.

Theorem 3.3. *If $\bar{c}$ and $\bar{n}$ have the same direction, then $\bar{r}$ is also in this direction.*

Proof. Suppose $\bar{c}$ and $\bar{n}$ have the same direction. Then $\bar{c} = k\bar{n}$ for some scalar k, so by Theorem 1

$$b = \bar{c} \circ \bar{n} = k\bar{n} \circ \bar{n} \qquad (22)$$

Replacing $\bar{c}$ in equations (20) by $k\bar{n}$ and using Lemma 1.C we obtain

$$\bar{r} \circ (k\bar{n} \times \bar{s}) = (a - \lambda)\bar{s}^T\bar{r} - b\bar{t}^T\bar{r}$$

$$\bar{r} \circ (k\bar{n} \times \bar{t}) = b\bar{s}^T\bar{r} + (a - \lambda)\bar{t}^T\bar{r} \qquad (23)$$

which can be rewritten as

$$0 = \bar{r} \circ (k\bar{n} \times \bar{s} - (a - \lambda)\bar{s} + b\bar{t}) = \bar{r} \circ \bar{w}_1$$

$$0 = \bar{r} \circ (k\bar{n} \times \bar{t} - b\bar{s} - (a - \lambda)\bar{t}) = \bar{r} \circ \bar{w}_2 \qquad (24)$$

Now $k\bar{n} \times \bar{s}$ lies in the plane of $\bar{s}$ and $\bar{t}$ since it is perpendicular to $\bar{n}$ so $\bar{w}_1$ also lies in this plane. Similarly, $\bar{w}_2$ lies in the plane of $\bar{s}$ and $\bar{t}$. If we can show that $\bar{w}_1$ and $\bar{w}_2$ are linearly independent, and note from equation (24) that $\bar{r}$ is perpendicular to both of them then $\bar{r}$ must be in the same direction as $\bar{n}$, the normal to this plane.

In order to show linear independence of $\bar{w}_1$ and $\bar{w}_2$, we first note that

$$\bar{w}_1 \circ \bar{s} = -(a - \lambda)(\bar{s} \circ \bar{s}) + b(\bar{t} \circ \bar{s})$$

$$\bar{w}_2 \circ \bar{t} = -b(\bar{s} \circ \bar{t}) - (a - \lambda)(\bar{t} \circ \bar{t}) \qquad (25)$$

Also, since

$$(k\bar{n} \times \bar{s}) \circ \bar{t} = -k\bar{n} \circ (\bar{t} \times \bar{s}) = -k\bar{n} \circ \bar{n} = -b$$

$$(k\bar{n} \times \bar{t}) \circ \bar{s} = k\bar{n} \circ (\bar{t} \times \bar{s}) = k\bar{n} \circ \bar{n} = b$$

we obtain

$$\bar{w}_1 \circ \bar{t} = -b - (a-\lambda)(\bar{s} \circ \bar{t}) + b(\bar{t} \circ \bar{t})$$

$$\bar{w}_2 \circ \bar{s} = b - b(\bar{s} \circ \bar{s}) - (a-\lambda)(\bar{t} \circ \bar{s}) \qquad (26)$$

To show linear independence we must show that $c_1\bar{w}_1 + c_2\bar{w}_2 = \bar{0}$ implies that $c_1 = c_2 = 0$. But $c_1\bar{w}_1 + c_2\bar{w}_2 = \bar{0}$ together with equations (25) and (26) imply that

$$0 = c_1(\bar{w}_1 \circ \bar{s}) + c_2(\bar{w}_2 \circ \bar{s})$$

$$= c_1\big(-(a-\lambda)(\bar{s} \circ \bar{s}) + b(\bar{t} \circ \bar{s})\big) + c_2\big(b - b(\bar{s} \circ \bar{s}) - (a-\lambda)(\bar{t} \circ \bar{s})\big)$$

$$0 = c_1(\bar{w}_1 \circ \bar{t}) + c_2(\bar{w}_2 \circ \bar{t})$$

$$= c_1\big(-b - (a-\lambda)(\bar{s} \circ \bar{t}) + b(\bar{t} \circ \bar{t})\big) + c_2\big(-b(\bar{s} \circ \bar{t}) - (a-\lambda)(\bar{t} \circ \bar{t})\big) \qquad (27)$$

We can write (27) as

$$M\begin{pmatrix} c_1 \\ c_2 \end{pmatrix} = \begin{pmatrix} 0 \\ 0 \end{pmatrix}$$

where

$$M = \begin{pmatrix} -(a-\lambda)(\bar{s} \circ \bar{s}) + b(\bar{t} \circ \bar{s}) & b - b(\bar{s} \circ \bar{s}) - (a-\lambda)(\bar{t} \circ \bar{s}) \\ -b - (a-\lambda)(\bar{s} \circ \bar{t}) + b(\bar{t} \circ \bar{t}) & -b(\bar{s} \circ \bar{t}) - (a-\lambda)(\bar{t} \circ \bar{t}) \end{pmatrix}$$

The determinant of M can be written as

$$\big((\bar{s} \circ \bar{s})(\bar{t} \circ \bar{t}) - (\bar{s} \circ \bar{t})^2\big)((a-\lambda)^2 + b^2)$$

which is greater than $(a-\lambda)^2 + b^2$ by the Cauchy-Schwarz inequality. Hence M is invertible so $c_1 = c_2 = 0$. This completes the proof.